UNIVERSITY OF CALIFORNIA

Santa Barbara

Operando NMR Study of the Selective Hydrogenolysis and Hydrogenation of Lignin Model Compounds Catalyzed by Ni/γ-Al_2O_3

A dissertation submitted in partial satisfaction of the

requirements for the degree Doctor of Philosophy

in Chemistry

by

Ali Chamas

Committee in charge:

Professor Susannah Scott, Chair

Professor Mahdi Abu-Omar

Professor Alison Butler

Professor R. Daniel Little

December 2021

The dissertation of Ali Chamas is approved.

_____
Alison Butler

_____
R. Daniel Little

_____
Mahdi M. Abu-Omar

_____
Susannah L. Scott, Committee Chair

October 2021

Operando NMR Study of the Selective Hydrogenolysis and Hydrogenation of Lignin Model Compounds Catalyzed by Ni/γ-Al_2O_3

ACKNOWLEDGEMENTS

First and foremost, I would like to express my deepest gratitude to Professor Susannah L. Scott. In my time in her group, she has pushed me to become a much more focused researcher. She pushes her students to do their best, and strives to make sure her student not only reach, but exceed their potential. I would like to extend my appreciation to my committee members, Professor Abu-Omar, Professor Butler, and Professor Little for giving me critical feedback over the years. Professor Butler's group was the first I rotated in at the start of my PhD. Professor Little helped me countless number of times with organic synthesis. Professor Abu-Omar has been a fantastic collaborator and co-author over the years. This PhD would not be possible if not for help from the group members past and present in the Scott group. I would especially like to thank Zach Jones, Long Qi, Tarnuma Tabassum, Jason Chalmers, and my former undergraduate mentee Quentin Kim. I would also like to acknowledge the scientists at MRL and CNSI, and in particular Jerry Hu and Jaya Nolt for their assistance with the NMR experiments. Additionally, much of this work would not be possible without the help of scientists at Pacific Northwest National Lab, in particular David Hoyt, Eric Walter, Nancy Washton, Sara Burton, Jesse Sears, Hardeep Mehta, and Andrew Lipton.

None of this would have been possible without the support I received from my friends and family. I would like to thank friends dating back from highschool, Jesse, Anthony, John, Brandon, Sabrina, Rebecca, and Anabel. Friends from my time at UCSB, David, Ricky, Michael, and Mackel. Friends from my cycling team years, Eric, Nicole, Mike, Alyssa, Will, Garrison, Vince, Richard, Gerald, and Brandon. Friends from New York, Sarah, Trey, and Daniel. Lastly, I thank my loving family, my father, mother, sister, and brother for their unwavering support.

Section 1.2 was partially adapted from the following publication:

Chamas, A.; Qi, L.; Mehta, H. S.; Sears, J. A.; Scott, S. L.; Walter, E. D.; Hoyt, D. W. High Temperature/Pressure MAS-NMR for the Study of Dynamic Processes in Mixed Phase Systems. *Magn. Reson. Imaging* **2019**, *56*, 37–44.

Chapter 2 was adapted from the following publication:

Walter, E. D.; Qi, L.; Chamas, A.; Mehta, H. S.; Sears, J. A.; Scott, S. L.; Hoyt, D. W. Operando MAS NMR Reaction Studies at High Temperatures and Pressures. *J. Phys. Chem. C* **2018**, *122*, 8209.

Chapter 3 was adapted from the following publication:

Qi, L.; Chamas, A.; Jones, Z. R.; Walter, E. D.; Hoyt, D. W.; Washton, N. M.; Scott, S. L. Unraveling the Dynamic Network in the Reactions of an Alkyl Aryl Ether Catalyzed by Ni/γ-Al2O3 in 2-Propanol. *J. Am. Chem. Soc.* **2019**, *141* (43), 17370–17381.

VITA OF ALI CHAMAS
October 2021

Education

Bachelor of Science in Biochemistry, University of California, Santa Barbara, Jun 2014

Doctor of Philosophy in Chemistry, University of California, Santa Barbara, October 2021 (expected)

Research Experience

2015-present: Graduate Research Assistant, Dept. of Chemistry & Biochemistry, UC Santa Barbara

Sep 2018: DOE Office of Science Graduate Student Research (SCGSR) Fellow, Pacific Northwest National Laboratory

Publications

7. Degradation Rates of Plastics in the Environment
Ali Chamas, Hyunjin Moon, Jiajia Zheng, Yang Qiu, Tarnuma Tabassum, Jun Hee Jang, Susannah L. Scott, Mahdi Abu-Omar, Sangwon Suh, (**2020**). *ACS Sustainable Chem. Eng,* 8, 3494-3511.

6. Unraveling the Dynamic Network in the Reactions of an Alkyl Aryl Ether Catalyzed by Ni/γ-Al_2O_3 in 2-Propanol
Long Qi, Ali Chamas, Zachary R. Jones, Eric D. Walter, David W. Hoyt, Nancy M. Washton, and Susannah L. Scott, (**2019**). *J. Am. Chem. Soc.*, 141, 17370-17381.

5. High Temperature/Pressure MAS-NMR for the Study of Dynamic Processes in Mixed Phase Systems
Ali Chamas, Long Qi, Hardeep S. Metha, Jesse A. Sears, Susannah L. Scott, Eric D. Walter, and David W. Hoyt, (**2019**), *Magn. Reson. Imaging*, 56, 37-44.

4. Operando MAS NMR Reaction Studies at High Temperatures and Pressures
Eric D. Walter, Long Qi, Ali Chamas, Hardeep S. Metha, Jesse A. Sears, Susannah L. Scott, and David W. Hoyt, (**2018**), *J. Phys. Chem. C*, 122, 8209–8215 (Cover)

3. Amino acid metaclusters: implications of growth trends on peptide self-assembly and structure
Thanh D Do, Natália EC De Almeida, Nichole E LaPointe, Ali Chamas, Stuart C Feinstein, Michael T Bowers, (**2016**) *Anal. Chem.*, 88, 868-876

2. Elucidation of the Aggregation Pathways of Helix–Turn–Helix Peptides: Stabilization at the Turn Region Is Critical for Fibril Formation
Thanh D Do, Ali Chamas, Xueyun Zheng, Aaron Barnes, Dayna Chang, Tjitske Veldstra, Harmeet Takhar, Nicolette Dressler, Benjamin Trapp, Kylie Miller, Audrene McMahon,

Stephen C Meredith, Joan-Emma Shea, Kristi Lazar Cantrell, Michael T Bowers, (**2015**), *Biochemistry*, 54, 4050-4062.

1. Interactions between Amyloid-β and Tau Fragments Promote Aberrant Aggregates: Implications for Amyloid Toxicity
Thanh D. Do, Nicholas J. Economou, Ali Chamas, Steven K. Buratto, Joan-Emma Shea, and Michael T. Bowers, (**2014**), *J. Phys. Chem. B, 118*, 11220-11230.

Presentations and Posters

3. Operando MAS-NMR Investigation of Ni/γ-Al_2O_3-Catalyzed Hydrogenolysis of Alkyl Aryl Ethers
Ali Chamas, Long Qi, Zachary R. Jones, Eric D. Walter, David W. Hoyt, and Susannah L. Scott, Gordan Research Conference: Biomass to Biobased Chemicals and Materials. July 2019, Newry, ME

2. Operando MAS-NMR Investigation of Ni/γ-Al_2O_3-Catalyzed Hydrogenolysis of Alkyl Aryl Ethers
Ali Chamas, Long Qi, Zachary R. Jones, Eric D. Walter, David W. Hoyt, and Susannah L. Scott, North American Catalysis Society Meeting. June 2019, Chicago, IL (Oral)

1. Catalytic Conversion of Lignin Model Compounds using *Operando* Spectroscopy
Ali Chamas, Long Qi, Zachary R. Jones, and Susannah L. Scott, Mellichamp workshop on Sustainable Chemical Manufacturing. March 22, 2017, Santa Barbara, CA

Awards

Department of Energy:

Office of Science Graduate Student Research (SCGSR) Fellowship: national award for collaborative, in-residence, research at a national lab. (2018)

University of California, Santa Barbara:

Outstanding Service to the Department: awarded by the UCSB Chemistry department. (2019)

UCSB Crossroads Fellow in Green Chemistry: interdisciplinary pedagogy fellowship focused on recycling and circular use of materials. (2017-2018)

Mellichamp Academic Initiative in Sustainability Fellowship: summer fellowships for sustainable material and product design. Promoted increased internal collaboration between fellows in the area of chemical sustainability. (2016, 2017)

ABSTRACT

Operando NMR Study of the Selective Hydrogenolysis and Hydrogenation of Lignin Model Compounds Catalyzed by Ni/γ-Al_2O_3

by

Ali Chamas

A plentiful material found in nature, nonfood lignocellulosic biomass has emerged as a promising renewable source of liquid fuels and valuable chemicals due to its high energy content and abundance of aromatics in the lignin fraction. However, the recalcitrant nature of lignocellulosic biomass hinders its efficient transformation to platform chemicals and fuels. To gain kinetic and mechanistic insight about organic transformations relevant to the valorization of lignin, the reductive cleavage of the aryl ether linkage and the hydrogenation of phenol, catalyzed by the heterogenous catalyst Ni/γ-Al_2O_3, were investigated.

Operando Magic Angle Spinning Nuclear Magnetic Resonance Spectroscopy (MAS-NMR) is a powerful and non-invasive tool for acquiring detailed kinetic information. Recent advances in the design of MAS NMR rotors allows for internal rotor pressures up to 400 bar and temperatures up to 250 °C. The new high temperature and pressure rotors were used to collect *operando* ^{1}H and ^{13}C spectra during the hydrogenolysis of benzyl phenyl ether (BPE), a lignin model compound, at temperatures up to 250 ºC, both with and without H_2 gas. In the absence of H_2, the 2-propanol solvent can serve as a source of H_2.

The reaction generates toluene and phenol with an apparent activation barrier of (80 ± 8) kJ mol^{-1} at temperatures of 150-170 ºC. Toluene does not undergo further hydrogenation at

these temperatures, but phenol undergoes subsequent, slow hydrogenation to cyclohexanol. Benzylic C-O bond cleavage is faster than H/D exchange in the methyl group of toluene, which in turn is faster than phenol hydrogenation. The source of the reducing equivalents for both hydrogenolysis and hydrogenation is exclusively H_2/D_2 gas rather than the solvent at these temperatures.

Although the rate of BPE hydrogenolysis is not strongly solvent-dependent, the selectivity to phenol changes with the choice of solvent: the rate of hydrogenation is significantly faster in solvents with lower polarity. The rates are strongly dependent on the extent of phenol adsorption on the catalyst surface, implicating the balance between phenol solvation and competitive adsorption. For polar protic solvents (typically, alcohols), the rate decreases with the strength of the hydrogen bonding between phenol and the solvent, presumably due to better solvation of phenol. In aprotic solvents (typically, alkanes and aromatics), the rate of phenol hydrogenation correlates inversely with the strength of solvent adsorption on Ni active sites. Consequently, selectivity in aryl ether hydrogenolysis to phenolics can be tuned by solvent selection with little impact on activity.

TABLE OF CONTENTS

LIST OF FIGURES, SCHEMES, AND TABLES

Chapter 1

Chapter 2

Chapter 3

Chapter 4

Chapter 1: Introduction

1.1 Characterization and Conversion of Lignin into Value Added Compounds

An increase in greenhouse gas emissions coupled with environmental issues caused by the burning of fossil fuels have motivated the development of renewable energy sources and sustainable alternatives to fossil fuel-based chemicals. Lignocellulosic biomass, a renewable, abundant, and nonedible raw material, has garnered attention as an ideal feedstock candidate over the last few decades. It is an essential component in woody plants, herbaceous plants, aquatic plants, forestry and agricultural residues, etc. Efforts are underway to effectively convert lignocellulose to biofuels and value-added chemicals and materials.[1–4] The conversion of lignocellulosic biomass, and in particular the lignin fraction, into value-added products remains a challenge due to the heterogeneity and complex structure of lignin-containing biomass.[5]

1.1.1 Structure and Role of Lignin in Plants

Lignocellulosic biomass consists of three major components, lignin, cellulose, and hemicellulose.[6] Lignin is a three−dimensional amorphous polymer comprised of methoxylated phenylpropane structures. The role of lignin in nature is to fill the spaces between cellulose and hemicellulose in plant cell walls, crosslinking the polysaccharides to improve mechanical strength of the cell wall and decrease water permeability. Scheme 1.1 demonstrates a schematic representation of lignin found in biomass. There are three types of monolignols (p−coumaryl alcohol, coniferyl alcohol and sinapyl alcohol) making up the lignin backbone, which form p−hydroxyphenyl (H), guaiacyl (G) and syringyl (S) units in lignin upon radical polymerization of the monolignols. These monolignols are connected by

linkages like β−O−4, β−5, 4−O−5, 5−5, β−1, and β−β, of which the β−O−4 linkage is dominant, comprising more than 50% of the lignin linkage structures in some lignins.[7]

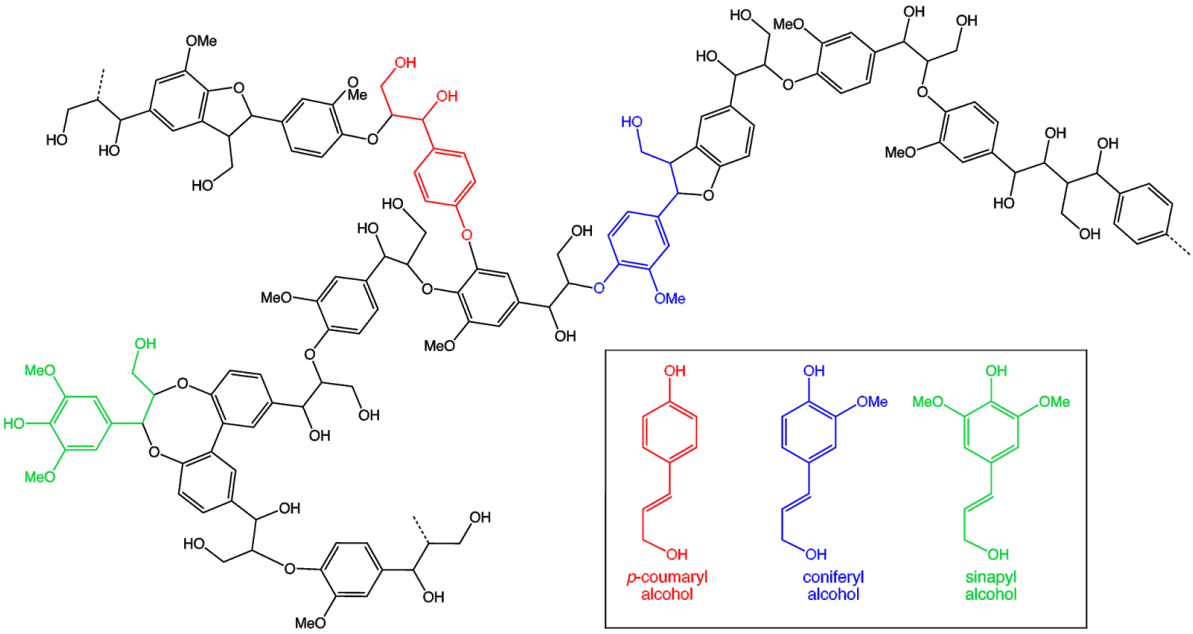

Scheme 1.1 Representative lignin fragment with different phenolic moieties and the monolignol building blocks *p*-coumaryl, coniferyl, and sinapyl alcohols.

1.1.2 Use of Solution State and 2D NMR for the Characterization of Lignin

Nuclear Magnetic Resonance Spectroscopy (NMR) is a common and powerful tool used for elucidating the structure and chemical composition of lignin. Chemical shift assignments of various lignin moieties using ^{1}H NMR can be elucidated to quantify carboxylic acids, formyl, aromatic hydrogens, and methoxy groups in lignin.[8] ^{13}C NMR has also been used to analyze lignin structural features due to the broader spectral window compared to ^{1}H NMR. For the complex lignin structure, traditional one-dimensional ^{1}H and ^{13}C NMR techniques usually suffer from severe signal overlap. To combat this issue, two-dimensional (2D) NMR correlation experiments are more commonly conducted on lignin and lignocellulosic biomass. 2D NMR experiments have been useful in analyzing the lignin structure, such as determining the presence of lignin subunits during various lignin extraction methods.[9,10]

However, many 2D NMR techniques have limitations since the spectra are not quantitative and spectral overlap still occurs. A complementary approach to 1D and 2D NMR techniques is the selective labeling of lignin or lignin model. For example, a ^{13}C label on the carbon atoms of an ether linkage in lignin or lignin model compounds can be used to quantitatively measure the concentration of ether linkages before and after a depolymerization reaction.

NMR is commonly used in measuring the concentration of β-O-4 linkages before and after extraction of the lignin fraction from the whole lignocellulosic biomass. For example, the kraft pulping process commonly used in the paper industry has been shown to damage native lignin linkages leading to an increase in condensation reactions to form phenolic groups and further increase lignin's recalcitrance.[11] HSQC NMR spectroscopy (2D ^{1}H-^{13}C heteronuclear single quantum coherence nuclear magnetic resonance spectroscopy) is commonly applied to measure the concentration of β-O-4 linkages on lignin. A simple 1D ^{13}C spectra would be insufficient to provide meaningful information for lignin due to the significant signal overlap in both the aliphatic regions and aromatic regions. As shown in Figure 1.1 and Figure 1.2, HSQC NMR provides two dimensional resolution of various linkages in lignin that can all be identified based on literature chemical shift assignments.[12] Additionally, HSQC NMR studies on the ethanol organosolv lignin and milled wood isolated from Miscanthus x giganteus have shown that the organosolv extraction process takes place through the scission of the β-O-4 linkages.[13] In a separate HSQC NMR study, characterization of six separate extracted lignins (Indulin Kraft, soda P1000, Alcell, poplar organosolv, and wheat straw organosolv lignins) showed that all lignins were highly condensed and had a low content of β-ether linkages after the isolation.[14]

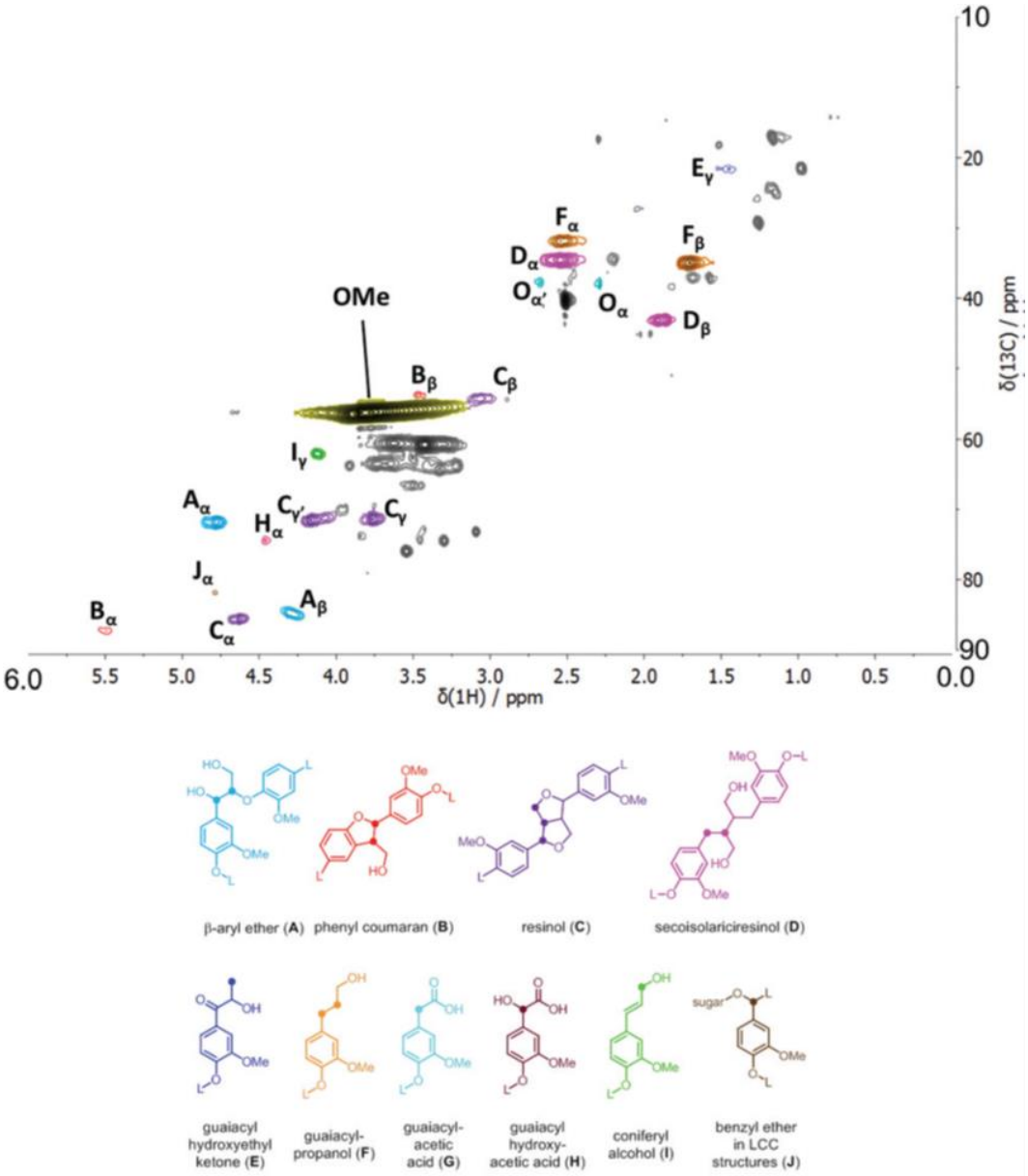

Figure 1.1 HSQC spectrum of softwood kraft lignin and assignments of selected structural features in the aliphatic region.[12]

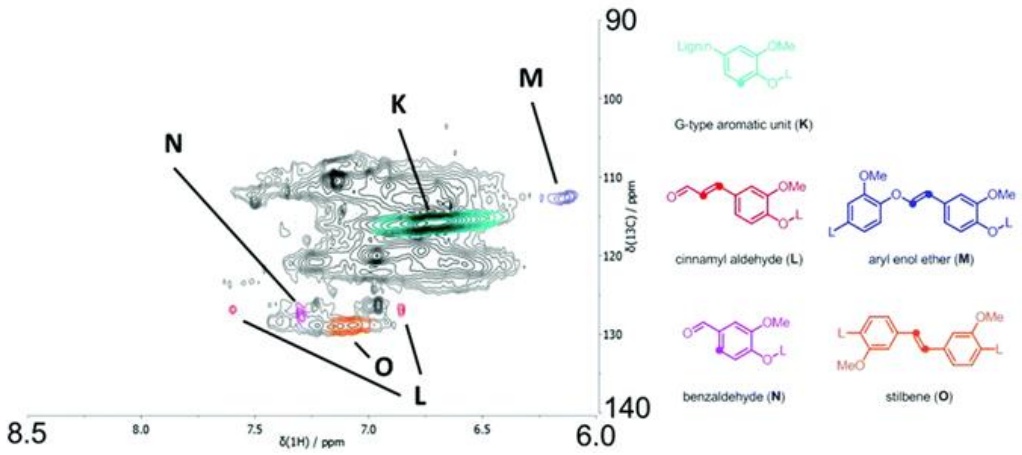

Figure 1.2. HSQC spectrum of softwood kraft lignin and assignments of selected structural features in the aromatic region.[12]

1.1.3 Background on Lignin Valorization

Extensive research has been conducted on developing new technologies for lignin valorization, or the efficient conversion of renewable and under-utilized lignin into high value products. Thermal conversion of lignin is a common method used and can be defined using a broad class of technologies which include pyrolysis, hydrothermal liquefaction, gasification, oxidative cracking, solvolysis, and hydrogenolysis.[7] These methods typically involve numerous complex reactions, and due to differing conditions (temperature, environment, catalyst, etc.) the yield and composition of the gaseous, liquid, and solid products can vary greatly.[1,15–18] New technologies are constantly emerging to study the depolymerization of lignin, to break the interunit linkages within the lignin macromolecule and convert the complex lignin polymers into oligomers or monomeric aromatic products for use in specialty fuels and chemicals. The use of heterogeneous catalysts for the depolymerization of lignin has the advantages of high efficiency, product selectivity, moderate reaction conditions, and ease of reaction control.[19] In particular, transition metal-

based catalysts have proven to be successful in catalyzing lignin depolymerization to phenolic products. Examples of these catalysts include nickel supported on HZSM-5, activated carbon, or SiO_2; copper supported on alumina or magnesia-alumina; Pt, Pd, Ru, Rh supported on active carbon or alumina; and many others.[20] The common target for depolymerization products under heterogeneous catalytic treatment is C6–C9 aromatics, with product selectivity dependent on the catalyst and reaction conditions. The high cost of platinum group metals (Pt, Pd, Ru, Rh) has promoted further research into more abundant and less costly metals including molybdenum, zinc, copper, and nickel.[21]

Lignin model compounds have been used to study the valorization of lignocellulosic biomass due to the difficulty in isolating pure lignin. One of the most common extraction methods is the organosolv process, which typically uses an organic solvent, most commonly with an acid co-catalyst and water to liberate large amounts of lignin from biomass.[22] Based on the conditions used in the organosolv process, cleavage of ether linkages as well as condensation reactions can occur.[23–25] The condensation is thought to occur via dehydration reactions and the formation of additional C-C linkages between neighboring aromatic groups. The dehydration reactions lead to the formation of benzylic carbocations from the protonation of the α-OH in various lignin structures. The reactive carbocations can then undergo electrophilic aromatic substation reactions to form C-C bonds between adjacent aromatic rings. As such, the extraction processes have been shown to lower monomer production, with yields of <10% during catalytic processing.[23,26] New approaches, called the "lignin-first" method, where the entire native lignocellulosic biomass is reacted in the presence of the catalyst has garnered interest. The reaction of whole lignocellulosic biomass leads to direct hydrogenolysis of the native lignin fraction, resulting in 40-50% monomer yields.[27–31]

1.2 *Operando* MAS NMR

1.2.1 Background of high-pressure and -temperature *operando* NMR rotors

In recent years, great efforts have been devoted to the development of high temperature/pressure nuclear magnetic resonance (NMR) for *in situ* and *operando* studies.[32,33] Early efforts studying liquid and/or gas samples[34] have used Roe-style ceramic tubes (sapphire or zirconia),[35] capillary tubes,[36] or polymer cells.[37] For solid or solid-containing samples direct pressurization of the probehead or the sample cavity was made possible,[38] with pressures of the probe head reaching 25,000 bar.[39] Adoption of sealed Magic Angle Spinning (MAS) NMR began with use of a glass insert filled with the solid sample and pre-adsorbed gas or liquid before being sealed and transferred into a MAS NMR rotor.[40] More recently, cavern style rotors have been used to introduce gases to rotors for *in situ* studies.[41,42] However, these MAS setups are incapable of introducing high pressure fluids or are intolerant of pressure build-up at higher temperature. Therefore, a sealed rotor design capable of handling elevated temperature/pressures and containing all phases of the analytes, a combination of solid, liquid and gas phase material, is desired. Simple o-ring seals on the rotor endcaps can provide a method of containing liquids and gases at near ambient pressure, and these products are offered by NMR instrumentation companies. Various lab-made designs have increased the pressure limits by trapping the o-ring beneath a screw; the internal threads that these screws engage are either in a bushing insert retained by adhesive in a commercial rotor, or integral to the ceramic of a custom machined monolith rotor.[43] Versions of this design have enabled *operando* spectra to be collected for growth of zeolite crystals or acid-catalyzed dehydration of cyclohexanol.[44,45]

These recent advances in NMR have allowed for detailed structural and mechanistic information of multiphasic systems at elevated temperatures and pressures to be

obtained.[46,47] Previously, the use of solid-state NMR in these multiphase systems had been limited due to the inability to reach both high temperatures and pressures.[48,49] The new cavern style rotors have been used in geochemistry and geoengineering looking at supercritical CO_2 intercalation and hydraulic fracturing fluid,[50,51] biological systems probing the effects of sequestered CO_2 on microbial environments,[52] and catalytic systems examining biomass valorization.[46,53]

1.2.2 Use of *Operando* NMR Rotors for Heterogeneous Catalysis

The cavern rotors allow the mixing of solids, such as catalytically active materials, with gases and liquids under MAS conditions. Thus, high-resolution NMR spectra can be acquired during the course of the reaction, which allows for the simultaneous detection of the reactants, products, intermediates, side-products, and solvents, with the potential to discriminate the phase or mobility of each species. Catalytic biomass conversion has been particularly challenging, typically requiring solid catalysts, solvents, and recalcitrant substrates. The cavern style rotors have been used to carry out investigations on carbohydrates and lignin,[46,53] the major components of biomass. In many cases, an isotopically labeled species was used in the reactant or solvent to enhance the desired signals and suppress the unwanted ones, minimizing acquisition time.

An example use of the cavern rotors in biomass conversion is the glucose isomerization reaction catalyzed by the solid base, NaX zeolite. Traditional methods can only provide information on the filtered reaction solution, but the reaction mostly occurs in the micropores of zeolite. NaX zeolite was mixed in a 5 mm or 7.5 mm cavern rotor with glucose-1-^{13}C dissolved in aqueous solution of γ-valerolactone (GVL) (46 mol%), Fig. 1.3. The adsorption of glucose in the zeolite can be significantly improved by a GVL-water

binary solvent without limitation of mass transfer in the catalytic reaction. At 25 °C, four resonances of glucose-C1 can be detected. The two sharp signals can be assigned to the glucopyranose tautomers in the bulk solution and the two broad signals corresponds to the adsorbed species inside the zeolite pores. The deconvolution of the quantitative ^{13}C NMR spectrum agrees with traditional adsorption studies, showing 65% of glucose being adsorbed.

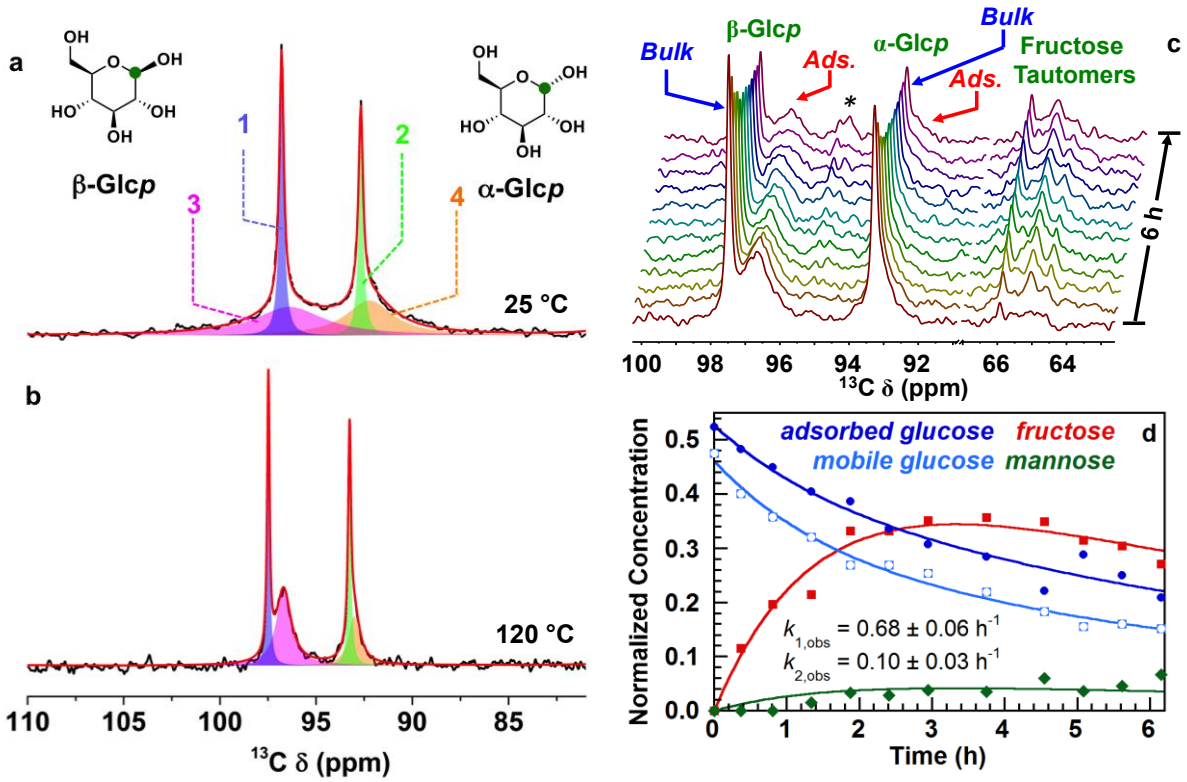

Figure 1.3. Direct polarization MAS solid-state ^{13}C NMR study (125.77 MHz, 5 kHz MAS) of a mixture of NaX zeolite (200 mg) with a solution of glucose-1-^{13}C (0.100 mol L^{-1}, 1.00 mL) in 46 mol % of GVL at 25 and 120 °C: (a) spectrum recorded at 25 °C (green dots indicate the locations of the ^{13}C labels, corresponding to the observed signals); (b) first spectrum recorded shortly after heating the rotor to 120 °C. (c) Relative amounts of α-Glc*p* and β-Glc*p* glucose tautomers in the adsorbed or solution phases, as determined by solid-state NMR at 25 and 120 °C. (c) Time-resolved *operando* spectra, showing glucose conversion to fructose (* denotes mannose side-product). (b) Kinetic profiles (points) for glucose adsorbed in the zeolite, glucose present in the solution phase, total fructose, and total mannose. The lines are curve fits to a bi-exponential rate, where $k_{1,obs}$ and $k_{2,obs}$ are the pseudo-first-order rate constants for fructose production and degradation, respectively.[53,54]

Upon temperature elevation to 120 °C, the signals of the adsorbed glucose sharpen as the mobility of the molecules is enhanced at higher temperature. In addition, all four glucose resonances start to decrease in intensity, due to the isomerization to fructose. The ratios among the adsorbed and mobile species stay unchanged during the course of the reaction, indicating the diffusion of glucose in-and-out of the zeolite is unlimited. Curve-fitting of the concentration profiles of glucose and fructose reveals that both the isomerization and the further deactivation of glucose and fructose follow pseudo-first-order kinetics. The rate constant of the isomerization coincides well with the value obtained from a plug-flow reactor.

1.3 Solvent Effects on Hydrogenolysis and Hydrogenation of Alkyl Aryl Ethers

Liquid-phase reactions catalyzed by supported metals are important in the chemical conversion of non-volatile feedstocks, such as the highly functionalized oxygenates derived from biomass. The presence of water, organic solvents, and reactive solutes presents challenges in understanding adsorption and reactions at solid-liquid interfaces, particularly under reaction conditions involving elevated temperatures and pressures.[55] Its reactions often take place in a triphasic solid-liquid-gas mixture involving temperatures >150 ºC and pressures >10 bar, and experimental studies are often accompanied by poor mass balances.[56] The mechanisms of cleavage of the major aryl ether C-O linkages in lignin by heterogeneous catalysts remain poorly documented,[57] and can be subject to strong solvent effects.

1.3.1 Solvent Effects on the Hydrogenolysis and Hydrogenation of Lignin

Much work has been done exploring solvent effects in enzymatic and homogeneous catalysis,[58] however such behavior is poorly explained in heterogeneous systems. There are some reports addressing solvent effects on the hydrogenation of aromatic alcohols and ketones with Pd on several supports,[59] Pt/Al_2O_3,[60] Ru/Al_2O_3, and Ni/SiO_2 catalysts,[61] and for the hydrogenolysis of lignin.[62] Solvents play a vital role in the catalytic conversion of lignin and lignin model compounds, acting as the medium to dissolve the reactants and solvate the eventual products.

A recent study on the solvent effects on the hydrogenation of model oxygenates derived from bio-oils, such as 2-butanone, 2-pentanone, and phenol, showed a strong influence of the solvent polarity on the rate of hydrogenation.[63] The Ru/C catalyzed hydrogenation of 2-butanone was measured in 10 different solvents: polar protic, polar aprotic, and polar aprotic, Figure 1.4. The rate of hydrogenation was greatest in water, followed by the remained of the polar protic solvents, then the apolar aprotic solvents, and finally the protic polar solvents. A correlation between the initial hydrogenation rate of 2-butanone and hydrogen-bond donor capability of the solvents was observed, and it was suggested that the hydrogen bonding lowers the activation energy barrier and leads to high hydrogenation rates. For the polar aprotic solvents, it was suggested that the solvent could strongly adsorb onto the catalyst surface and block the Ru active sites leading to an inhibition of the hydrogenation, however no evidence was provided.

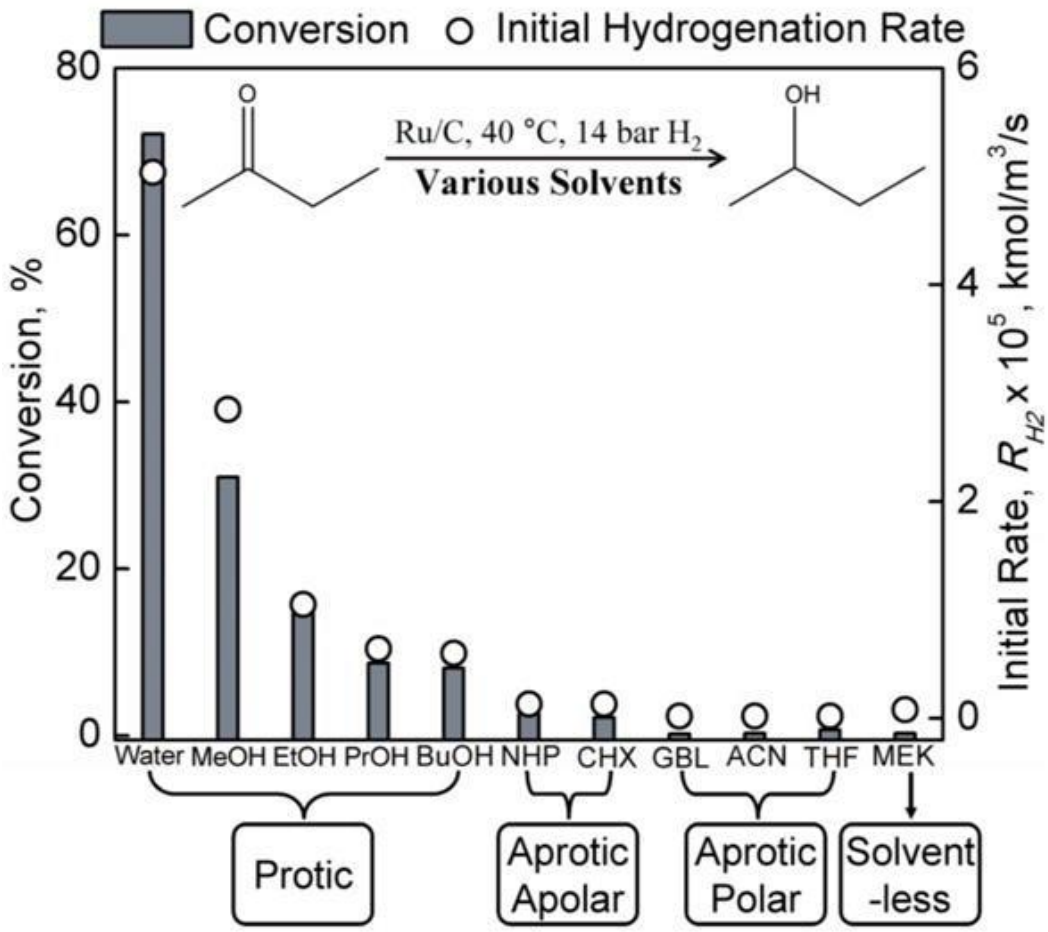

Figure 1.4 Solvent effects in 2-butanone hydrogenation with 1% Ru/C catalyst and 14 bar H_2 gas at 40 °C for 1 hr. Legend: (■) 2-butanone conversion, and (○) initial hydrogenation rate.[63]

Polar protic solvents such as methanol or ethanol have been extensively used as the solvent for lignin valorization since lignin is largely insoluble in nonpolar solvents or water. A previous study found that the monomer containing oil fraction after reaction was ca. 2x greater if ethanol was used as a solvent for lignin depolymerization compared with yields using methanol or isopropanol as the solvent. The increase in monomer yield was due to increased etherification of the highly reactive phenolic intermediates that are formed during the reaction.[64] The authors suggest the use of methanol as the solvent resulted in less O-

alkylation due to the decomposition under the reaction conditions to formic acid. In the case of 2-propanol, higher steric hindrance towards O-alkylation resulted in a decrease in monomer yield.[64]

Researchers have proposed that the interaction of solvent with the reactant and/or solvent interactions with the catalyst could be the main factor affecting aromatic hydrogenation reactions in different solvents.[61,65] Solvent effects in heterogeneous catalysis have often been rationalized by a correlation to activity or product distribution to the polarity of the solvent.[66] For polar adsorbates in contact with a polar solvent, solvation of the substrate is expected to occur through electrostatic interactions and hydrogen bonding. In contrast, in nonpolar systems the dominating factor in solvating the substrate is London dispersion and van der Waals forces.[67] Therefore, nonpolar solvents are known to enhance the adsorption of polar react polar reactants.[68] For example, phenol has been shown to have an increased affinity for the surface of Pd/Al_2O_3 and Pd/SiO_2, and a higher rate of hydrogenation in less polar cyclohexane compared to more polar ethanol.[69] Nevertheless, the existing research on solvent effects in heterogeneous catalysis is sparse, and further research examining these effects on lignin valorization must be conducted in order to advance the rational choice of the reaction medium in the design of catalytic systems for the valorization of lignin.

1.4 References

(1) Tuck, C. O.; Pérez, E.; Horváth, I. T.; Sheldon, R. A.; Poliakoff, M. Valorization of Biomass: Deriving More Value from Waste. *Science* **2012**, *337* (6095), 695–699.

(2) Cao, L.; Yu, I. K. M.; Liu, Y.; Ruan, X.; Tsang, D. C. W.; Hunt, A. J.; Ok, Y. S.; Song, H.; Zhang, S. Lignin Valorization for the Production of Renewable Chemicals:

State-of-the-Art Review and Future Prospects. *Bioresour. Technol.* **2018**, *269*, 465–475.

(3) Guan, W.; Tsang, C.-W.; Lin, C. S. K.; Len, C.; Hu, H.; Liang, C. A Review on High Catalytic Efficiency of Solid Acid Catalysts for Lignin Valorization. *Bioresour. Technol.* **2020**, *298*, 122432.

(4) Xu, L.; Zhang, S.-J.; Zhong, C.; Li, B.-Z.; Yuan, Y.-J. Alkali-Based Pretreatment-Facilitated Lignin Valorization: A Review. *Ind. Eng. Chem. Res.* **2020**, *59* (39), 16923–16938.

(5) Boerjan, W.; Ralph, J.; Baucher, M. Lignin Biosynthesis. *Annu. Rev. Plant Biol.* **2003**, *54*, 519–546.

(6) Kleinert, M.; Barth, T. Phenols from Lignin. *Chem. Eng. Technol.* **2008**, *31* (5), 736–745.

(7) Pandey, M. P.; Kim, C. S. Lignin Depolymerization and Conversion: A Review of Thermochemical Methods. *Chem. Eng. Technol.* **2011**, *34* (1), 29–41.

(8) Li, S.; Lundquist, K. A New Method for the Analysis of Phenolic Groups in Lignins by ^{1}H NMR Spectrometry. *Nord. Pulp Pap. Res. J.* **1994**, *9* (3), 191–195.

(9) Zhang, L.; Gellerstedt, G.; Ralph, J.; Lu, F. NMR Studies on the Occurrence of Spirodienone Structures in Lignins. *J. Wood Chem. Technol.* **2006**, *26* (1), 65–79.

(10) Zhang, L.; Henriksson, G.; Gellerstedt, G. The Formation of β–β Structures in Lignin Biosynthesis—Are There Two Different Pathways? *Org. Biomol. Chem.* **2003**, *1* (20), 3621–3624.

(11) Lancefield, C. S.; Wienk, H. L. J.; Boelens, R.; Weckhuysen, B. M.; Bruijnincx, P. C. A. Identification of a Diagnostic Structural Motif Reveals a New Reaction

Intermediate and Condensation Pathway in Kraft Lignin Formation. *Chem. Sci.* **2018**, *9* (30), 6348–6360.

(12) Crestini, C.; Lange, H.; Sette, M.; Argyropoulos, D. S. On the Structure of Softwood Kraft Lignin. *Green Chem.* **2017**, *19* (17), 4104–4121.

(13) El Hage, R.; Brosse, N.; Sannigrahi, P.; Ragauskas, A. Effects of Process Severity on the Chemical Structure of Miscanthus Ethanol Organosolv Lignin. *Polym. Degrad. Stab.* **2010**, *95* (6), 997–1003.

(14) Constant, S.; Wienk, H. L. J.; Frissen, A. E.; Peinder, P. de; Boelens, R.; Es, D. S. van; Grisel, R. J. H.; Weckhuysen, B. M.; Huijgen, W. J. J.; Gosselink, R. J. A.; Bruijnincx, P. C. A. New Insights into the Structure and Composition of Technical Lignins: A Comparative Characterisation Study. *Green Chem.* **2016**, *18* (9), 2651–2665.

(15) Zakzeski, J.; Bruijnincx, P. C. A.; Jongerius, A. L.; Weckhuysen, B. M. The Catalytic Valorization of Lignin for the Production of Renewable Chemicals. *Chem Rev* **2010**, *110* (6), 3552–3599.

(16) Calvo-Flores, F. G.; Dobado, J. A. Lignin as Renewable Raw Material. *ChemSusChem* **2010**, *3* (11), 1227–1235.

(17) Azadi, P.; Inderwildi, O. R.; Farnood, R.; King, D. A. Liquid Fuels, Hydrogen and Chemicals from Lignin: A Critical Review. *Renew Sust Energ Rev* **2013**, *21* (0), 506–523.

(18) Ragauskas, A. J.; Beckham, G. T.; Biddy, M. J.; Chandra, R.; Chen, F.; Davis, M. F.; Davison, B. H.; Dixon, R. A.; Gilna, P.; Keller, M.; Langan, P.; Naskar, A. K.; Saddler, J. N.; Tschaplinski, T. J.; Tuskan, G. A.; Wyman, C. E. Lignin Valorization: Improving Lignin Processing in the Biorefinery. *Science* **2014**, *344* (6185).

(19) Wang, H.; Tucker, M.; Ji, Y. Recent Development in Chemical Depolymerization of Lignin: A Review. *J. Appl. Chem.* **2013**, *2013*, 838645.

(20) Phan, D.-P.; Lee, E. Y. Controlled Hydrogenolysis over Heterogeneous Catalysts for Lignin Valorization. *Catal. Rev.* **2020**, *62* (4), 607–630.

(21) Xiao, L.-P.; Wang, S.; Li, H.; Li, Z.; Shi, Z.-J.; Xiao, L.; Sun, R.-C.; Fang, Y.; Song, G. Catalytic Hydrogenolysis of Lignins into Phenolic Compounds over Carbon Nanotube Supported Molybdenum Oxide. *ACS Catal.* **2017**, *7* (11), 7535–7542.

(22) Johansson, A.; Aaltonen, O.; Ylinen, P. Organosolv Pulping — Methods and Pulp Properties. *Biomass* **1987**, *13* (1), 45–65.

(23) Sun, Z.; Fridrich, B.; de Santi, A.; Elangovan, S.; Barta, K. Bright Side of Lignin Depolymerization: Toward New Platform Chemicals. *Chem. Rev.* **2018**, *118* (2), 614–678.

(24) Rinaldi, R.; Jastrzebski, R.; Clough, M. T.; Ralph, J.; Kennema, M.; Bruijnincx, P. C. A.; Weckhuysen, B. M. Paving the Way for Lignin Valorisation: Recent Advances in Bioengineering, Biorefining and Catalysis. *Angew. Chem. Int. Ed.* **2016**, *55* (29), 8164–8215.

(25) Schutyser, W.; Renders, T.; Van den Bosch, S.; Koelewijn, S. F.; Beckham, G. T.; Sels, B. F. Chemicals from Lignin: An Interplay of Lignocellulose Fractionation, Depolymerisation, and Upgrading. *Chem. Soc. Rev.* **2018**, *47* (3), 852–908.

(26) Shuai, L.; Talebi Amiri, M.; Luterbacher, J. S. The Influence of Interunit Carbon–Carbon Linkages during Lignin Upgrading. *Curr. Opin. Green Sustain. Chem.* **2016**, *2*, 59–63.

(27) Parsell, T.; Yohe, S.; Degenstein, J.; Jarrell, T.; Klein, I.; Gencer, E.; Hewetson, B.; Hurt, M.; Kim, J. I.; Choudhari, H.; Saha, B.; Meilan, R.; Mosier, N.; Ribeiro, F.;

Delgass, W. N.; Chapple, C.; Kenttämaa, H. I.; Agrawal, R.; Abu-Omar, M. M. A Synergistic Biorefinery Based on Catalytic Conversion of Lignin Prior to Cellulose Starting from Lignocellulosic Biomass. *Green Chem.* **2015**, *17* (3), 1492–1499.

(28) Bosch, S. V. den; Schutyser, W.; Koelewijn, S.-F.; Renders, T.; Courtin, C. M.; Sels, B. F. Tuning the Lignin Oil OH-Content with Ru and Pd Catalysts during Lignin Hydrogenolysis on Birch Wood. *Chem. Commun.* **2015**, *51* (67), 13158–13161.

(29) Ferrini, P.; Rinaldi, R. Catalytic Biorefining of Plant Biomass to Non-Pyrolytic Lignin Bio-Oil and Carbohydrates through Hydrogen Transfer Reactions. *Angew. Chem. Int. Ed.* **2014**, *53* (33), 8634–8639.

(30) Galkin, M. V.; Samec, J. S. M. Selective Route to 2-Propenyl Aryls Directly from Wood by a Tandem Organosolv and Palladium-Catalysed Transfer Hydrogenolysis. *ChemSusChem* **2014**, *7* (8), 2154–2158.

(31) Abu-Omar, M. M.; Barta, K.; Beckham, G. T.; Luterbacher, J. S.; Ralph, J.; Rinaldi, R.; Román-Leshkov, Y.; Samec, J. S. M.; Sels, B. F.; Wang, F. Guidelines for Performing Lignin-First Biorefining. *Energy Environ. Sci.* **2021**, *14* (1), 262–292.

(32) Zhang, W.; Xu, S.; Han, X.; Bao, X. In Situ Solid-State NMR for Heterogeneous Catalysis: A Joint Experimental and Theoretical Approach. *Chem. Soc. Rev.* **2012**, *41* (1), 192–210.

(33) Blasco, T. Insights into Reaction Mechanisms in Heterogeneous Catalysis Revealed by in Situ NMR Spectroscopy. *Chem. Soc. Rev.* **2010**, *39* (12), 4685–4602.

(34) Yonker, C. R.; Linehan, J. C. The Use of Supercritical Fluids as Solvents for NMR Spectroscopy. *Prog. Nucl. Magn. Reson. Spectrosc.* **2005**, *47* (1), 95–109.

(35) Horváth, I. T.; Millar, J. M. NMR under High Gas Pressure. *Chem. Rev.* **1991**, *91* (7), 1339–1351.

(36) Yonker, C. R.; Zemanian, T. S.; Wallen, S. L.; Linehan, J. C.; Franz, J. A. A New Apparatus for the Convenient Measurement of NMR Spectra in High-Pressure Liquids. *J. Magn. Reson. A* **1995**, *113* (1), 102–107.

(37) Wallen, S. L.; Schoenbachler, L. K.; Dawson, E. D.; Blatchford, M. A. A Polymer NMR Cell for the Study of High-Pressure and Supercritical Fluid Solutions. *Anal. Chem.* **2000**, *72* (17), 4230–4234.

(38) Jonas, J. *High Pressure NMR*; Springer, Berlin, Heidelberg, 1991; Vol. 24.

(39) Edwards, T.; Endo, T.; Walton, J. H.; Sen, S. Observation of the Transition State for Pressure-Induced $BO_3 \rightarrow$ BO4 Conversion in Glass. *Science* **2014**, *345* (6200), 1027–1029.

(40) Freude, D.; Hunger, M.; Pfeifer, H. Study of Brønsted Acidity of Zeolites Using High-Resolution Proton Magnetic Resonance with Magic-Angle Spinning. *Chem. Phys. Lett.* **1982**, *91* (4), 307–310.

(41) Munson, E. J.; Ferguson, D. B.; Kheir, A. A.; Haw, J. F. Applications of a New CAVERN Design to the Study of Reactions on Catalysts Using in Situ Solid-State NMR. *J. Catal.* **1992**, *136* (2), 504–509.

(42) Chen, K.; Abdolrhamani, M.; Sheets, E.; Freeman, J.; Ward, G.; White, J. L. Direct Detection of Multiple Acidic Proton Sites in Zeolite HZSM-5. *J. Am. Chem. Soc.* **2017**, *139* (51), 18698–18704.

(43) Hu, J. Z.; Hu, M. Y.; Zhao, Z.; Xu, S.; Vjunov, A.; Shi, H.; Camaioni, D. M.; Peden, C. H. F.; Lercher, J. A. Sealed Rotors for in Situ High Temperature High Pressure MAS NMR. *Chem. Commun.* **2015**, *51* (70), 13458–13461.

(44) Prodinger, S.; Vjunov, A.; Hu, J. Z.; Fulton, J. L.; Camaioni, D. M.; Derewinski, M. A.; Lercher, J. A. Elementary Steps of Faujasite Formation Followed by in Situ Spectroscopy. *Chem. Mater.* **2018**, *30* (3), 888–897.

(45) Zhao, Z.; Shi, H.; Wan, C.; Hu, M. Y.; Liu, Y.; Mei, D.; Camaioni, D. M.; Hu, J. Z.; Lercher, J. A. Mechanism of Phenol Alkylation in Zeolite H-BEA Using In Situ Solid-State NMR Spectroscopy. *J. Am. Chem. Soc.* **2017**, *139* (27), 9178–9185.

(46) Walter, E. D.; Qi, L.; Chamas, A.; Mehta, H. S.; Sears, J. A.; Scott, S. L.; Hoyt, D. W. Operando MAS NMR Reaction Studies at High Temperatures and Pressures. *J. Phys. Chem. C* **2018**, *122* (15), 8209–8215.

(47) Hoyt, D. W.; Turcu, R. V. F.; Sears, J. A.; Rosso, K. M.; Burton, S. D.; Felmy, A. R.; Hu, J. Z. High-Pressure Magic Angle Spinning Nuclear Magnetic Resonance. *J Magn Reson* **2011**, *212* (2), 378–385.

(48) Vjunov, A.; Hu, M. Y.; Feng, J.; Camaioni, D. M.; Mei, D.; Hu, J. Z.; Zhao, C.; Lercher, J. A. Following Solid-Acid-Catalyzed Reactions by MAS NMR Spectroscopy in Liquid Phase—Zeolite-Catalyzed Conversion of Cyclohexanol in Water. *Angew. Chem. Int. Ed.* **2014**, *53* (2), 479–482.

(49) He, T.; Ren, P.; Liu, X.; Xu, S.; Han, X.; Bao, X. Direct Observation of DME Carbonylation in the Different Channels of H-MOR Zeolite by Continuous-Flow Solid-State NMR Spectroscopy. *Chem. Commun.* **2015**, *51* (94), 16868–16870.

(50) Jung, H. B.; Carroll, K. C.; Kabilan, S.; Heldebrant, D. J.; Hoyt, D.; Zhong, L.; Varga, T.; Stephens, S.; Adams, L.; Bonneville, A. Stimuli-Responsive/Rheoreversible Hydraulic Fracturing Fluids as a Greener Alternative to Support Geothermal and Fossil Energy Production. *Green Chem.* **2015**, *17* (5), 2799–2812.

(51) Bowers, G. M.; Schaef, H. T.; Loring, J. S.; Hoyt, D. W.; Burton, S. D.; Walter, E. D.; Kirkpatrick, R. J. Role of Cations in CO_2 Adsorption, Dynamics, and Hydration in Smectite Clays under in Situ Supercritical CO_2 Conditions. *J Phys Chem C* **2017**, *121* (1), 577–592.

(52) Wilkins, M. J.; Hoyt, D. W.; Marshall, M. J.; Alderson, P. A.; Plymale, A. E.; Markillie, L. M.; Tucker, A. E.; Walter, E. D.; Linggi, B. E.; Dohnalkova, A. C. CO_2 Exposure at Pressure Impacts Metabolism and Stress Responses in the Model Sulfate-Reducing Bacterium Desulfovibrio Vulgaris Strain Hildenborough. *Front. Microbiol.* **2014**, *5*.

(53) Qi, L.; Alamillo, R.; Elliott, W. A.; Andersen, A.; Hoyt, D. W.; Walter, E. D.; Han, K. S.; Washton, N. M.; Rioux, R. M.; Dumesic, J. A.; Scott, S. L. Operando Solid-State NMR Observation of Solvent-Mediated Adsorption-Reaction of Carbohydrates in Zeolites. *ACS Catal.* **2017**, 3489–3500.

(54) Chamas, A.; Qi, L.; Mehta, H. S.; Sears, J. A.; Scott, S. L.; Walter, E. D.; Hoyt, D. W. High Temperature/Pressure MAS-NMR for the Study of Dynamic Processes in Mixed Phase Systems. *Magn. Reson. Imaging* **2019**, *56*, 37–44.

(55) Sievers, C.; Noda, Y.; Qi, L.; Albuquerque, E. M.; Rioux, R. M.; Scott, S. L. Phenomena Affecting Catalytic Reactions at Solid–Liquid Interfaces. *ACS Catal.* **2016**, *6* (12), 8286–8307.

(56) Bernt, C. M.; Bottari, G.; Barrett, J. A.; Scott, S. L.; Barta, K.; Ford, P. C. Mapping Reactivities of Aromatic Models with a Lignin Disassembly Catalyst. Steps Toward Controlling Product Selectivity. *Catal. Sci. Technol.* **2016**, *6* (9), 2984–2994.

(57) Froass, P. M.; Ragauskas, A. J.; Jiang, J.-E. Chemical Structure of Residual Lignin from Kraft Pulp. *J. Wood Chem. Technol.* **1996**, *16* (4), 347–365.

(58) Singh, U. K.; Vannice, M. A. Kinetics of Liquid-Phase Hydrogenation Reactions over Supported Metal Catalysts — a Review. *Appl. Catal. Gen.* **2001**, *213* (1), 1–24.

(59) Bejblová, M.; Zámostný, P.; Červený, L.; Čejka, J. Hydrodeoxygenation of Benzophenone on Pd Catalysts. *Appl. Catal. Gen.* **2005**, *296* (2), 169–175.

(60) Takagi, H.; Isoda, T.; Kusakabe, K.; Morooka, S. Effects of Solvents on the Hydrogenation of Mono-Aromatic Compounds Using Noble-Metal Catalysts. *Energy Fuels* **1999**, *13* (6), 1191–1196.

(61) Bertero, N. M.; Trasarti, A. F.; Apesteguía, C. R.; Marchi, A. J. Solvent Effect in the Liquid-Phase Hydrogenation of Acetophenone over Ni/SiO_2: A Comprehensive Study of the Phenomenon. *Appl. Catal. Gen.* **2011**, *394* (1), 228–238.

(62) Benigni, J. D.; Goldstein, I. S. Hydrogenation of Kraft Lignin. *J. Polym. Sci. Part C Polym. Symp.* **1971**, *36* (1), 477–488.

(63) Wan, H.; Vitter, A.; Chaudhari, R. V.; Subramaniam, B. Kinetic Investigations of Unusual Solvent Effects during Ru/C Catalyzed Hydrogenation of Model Oxygenates. *J. Catal.* **2014**, *309*, 174–184.

(64) Oregui-Bengoechea, M.; Gandarias, I.; Arias, P. L.; Barth, T. Unraveling the Role of Formic Acid and the Type of Solvent in the Catalytic Conversion of Lignin: A Holistic Approach. *ChemSusChem* **2017**, *10* (4), 754–766.

(65) Ramos, R.; Tišler, Z.; Kikhtyanin, O.; Kubička, D. Solvent Effects in Hydrodeoxygenation of Furfural-Acetone Aldol Condensation Products over Pt/TiO_2 Catalyst. *Appl. Catal. Gen.* **2017**, *530*, 174–183.

(66) Gilbert, L.; Mercier, C. Solvent Effects in Heterogeneous Catalysis : Application to the Synthesis of Fine Chemicals. In *Studies in Surface Science and Catalysis*; Guisnet, M., Barbier, J., Barrault, J., Bouchoule, C., Duprez, D., Pérot, G.,

Montassier, C., Eds.; Heterogeneous Catalysis and Fine Chemicals III; Elsevier, 1993; Vol. 78, pp 51–66.

(67) Mathew, K.; Sundararaman, R.; Letchworth-Weaver, K.; Arias, T. A.; Hennig, R. G. Implicit Solvation Model for Density-Functional Study of Nanocrystal Surfaces and Reaction Pathways. *J. Chem. Phys.* **2014**, *140* (8), 084106.

(68) Zare, M.; Saleheen, M.; Kundu, S. K.; Heyden, A. Dependency of Solvation Effects on Metal Identity in Surface Reactions. *Commun. Chem.* **2020**, *3* (1), 1–10.

(69) Li, X.; Cheng, L.; Wang, X. Selective Phenol Hydrogenation under Mild Condition over Pd Catalysts Supported on $Al_2O_3$and SiO_2. *Res. Chem. Intermed.* **2019**, *45* (3), 1249–1262.

Chapter 2: Operando MAS-NMR Reaction Studies at High Temperatures and Pressures

2.1 Abstract

Operando MAS-NMR studies provide unique insights into the details of chemical reactions; comprehensive information about temperature- and time-dependent changes in chemical species is accompanied by similarly rich information about changes in phase and chemical environment. Here we describe a new MAS-NMR rotor (the *WHiMS* rotor) capable of achieving internal pressures up to 400 bar at 20 °C or 225 bar at 250 °C, a range which includes many reactions of interest. The MAS-NMR spectroscopy enabled by these rotors is ideal for studying the behavior of mixed-phase systems, such as reactions involving solid catalysts and volatile liquids, with the potential to add gases at high pressure. The versatile operation of the new rotors is demonstrated by collecting *operando* ^{1}H and ^{13}C spectra during the hydrogenolysis of benzyl phenyl ether, catalyzed by Ni/γ-Al_2O_3 at ca. 250 ºC, both with and without H_2 (g) supplied to the rotor. The 2-propanol solvent, which exists in the supercritical phase under these reaction conditions, serves as an internal source of H_2. The NMR spectra provide detailed kinetic profiles for the formation of the primary products toluene and phenol, as well as secondary hydrogenation and etherification products.

2.2 Introduction

The investigation of multiphasic systems and interfacial phenomena at elevated temperatures and pressures is a highly-sought experimental goal. For example, in the study of catalytic reactions, key intermediates may be observed only under conditions closely resembling those of the reaction itself (*e.g.*, temperature, solvent). Compared to chromatographic techniques which involve separation prior to *ex situ* analysis, NMR spectroscopy distinguishes molecules in complex mixtures without the need for separation,

and is therefore well-suited to *in situ* analysis.[1-2] NMR is also sensitive to the local chemical environment, which makes it ideal for *operando* and *in situ* study.[3-4] Magic Angle Spinning (MAS) NMR further enables NMR spectroscopy for mixed phase systems; in spite of being generally synonymous with Solid-State NMR, the analyte may be a combination of solids, liquids and gasses. Even when the species of interest is in the mobile phase, MAS provides significant line narrowing in mixed-phased systems.[5] Furthermore, solid-state NMR, as a surface-sensitive technique, also empowers the study of the interaction of molecules with solid catalysts. For example, MAS-NMR revealed that both temperature and solvent composition play a critical role in directing the adsorption of glucose by a faujasite zeolite.[6] However, its use in multiphase systems has been restricted due to limits in combined high temperature and pressure.

Conventional MAS-NMR rotors can contain liquids and gases at near ambient pressure, and various designs have been proposed to increase the pressure limits. In particular, several pressurized MAS rotor systems[7-12] were pioneered at PNNL, where they were initially employed for geochemical[5, 13-20] and biogeochemical[21] studies. Although these earlier rotor designs were capable of handling pressures up to 200 bar at 20 °C, they required the use of a loading chamber that enabled mechanical opening and closing of the rotor valve under pressure.[7-8] Such loading chambers are expensive, custom equipment, and the dead volume of the vessel increases the gas consumption (an important factor with isotopically-labelled gases). The rotors also had material limitations with steam or aggressive solvents above ~130 °C, due to degradation of the high temperature adhesive,[7-8] precluding the investigation of many reactions of interest. Other researchers avoided the use of adhesives by constructing a ceramic (zirconia) monolith.[10, 22-23] However, this design was ultimately

limited by the inability to add gas to the rotor; it relied solely on the increased vapor pressure of the solvent to build pressure.

In this contribution, we describe the *WHiMS* rotor (based on the initials of its designers – Walter, Hoyt, Mehta and Sears)[24] that can hold pressures in excess of 400 bar (depending on temperature, spinning rate and rotor size) and attain temperatures exceeding 250 °C. Early versions of this design enabled *in situ* and *operando* NMR spectra to be collected on hydraulic fracturing fluids[25] and carbohydrates in zeolites.[6] The expanded temperature and pressure ranges open up the possibility of obtaining MAS-NMR spectra for much more challenging systems. Here we present new results on the catalytic hydrogenolysis of benzyl phenyl ether (BPE), a model compound with a C-O ether linkage, whose bond energy is comparable to that found in lignin.[26] Lignin is a naturally-occurring aromatic macromolecule that typically comprises 15-30 % of the dry weight of woody biomass. It can be disassembled into its constituent aromatic monomers by selective hydrogenolysis of its aryl ether linkages using a Ni-based heterogeneous catalyst at elevated temperatures.[27-29] A common undesired side-reaction is aromatic hydrogenation,[29] whose impact can be mitigated by understanding and controlling the behavior of intermediates at the solid/liquid interface. This reaction system demonstrates the capabilities of the *WHiMS* MAS rotors to handle a wide range of reaction conditions, including pressures exceeding 200 bar at 250 °C. Further, the design makes it possible to observe all of the components in mixed phase systems (solid, liquid, gas, and/or supercritical fluids), including the partitioning of components in multiple phases, simultaneously.

2.3 Experimental Methods

2.3.1 Chemicals

The following chemicals were purchased from commercial suppliers and used as received: 2-propanol-d_0 (Sigma-Aldrich, 99.5 % anhydrous), 2-propanol-d_8 (Sigma-Aldrich, 99 %, 99.5 atom % D), phenyl isopropyl ether (P*i*PE, Enamine, 95 %), ethylene glycol (Mallinckrodt), lead nitrate (Sigma-Aldrich). Selectively ^{13}C-labelled benzyl phenyl ether was synthesized from toluene-α-^{13}C and phenol-1-^{13}C (Cambridge Isotopes, 98 %, 99 atom % ^{13}C) according to literature procedures.[30-31] The 2 wt% Ni/γ-Al_2O_3 catalyst was prepared using a modified literature procedure.[32]

2.3.2 *Operando* Solid-State NMR

MAS-NMR experiments were performed on an Agilent-Varian VNMRS NMR spectrometer equipped with an 11.7 T magnet, operating at 125.7747 MHz for the ^{13}C channel and 500.1822 MHz for ^{1}H channel, and using a 5 mm or 7.5 mm homebuilt MAS double-resonance HX probe with a custom Pd-coated coil for increased sample magnetic homogeneity. The rotor was heated to various set temperatures and both ^{13}C and ^{1}H spectra were collected before further temperature elevation. All rotors were Varian/Agilent-style cavern rotors (Revolution NMR LLC), modified for high pressure samples as described in the Results and Discussion section. Bushings were constructed of Vespel and equipped with either Viton O-rings (for temperatures up to 200 °C) or Kalrez O-rings (for experiments over 200 °C). Rotors were weighed before and after pressurization and then again after spectral acquisitions to verify that no leakage occurred. Typically, weights were within 0.2 mg of the starting weight with the conditions presented in this paper.

To study the BPE hydrogenolysis reaction, the rotor was loaded with ^{13}C-labeled BPE (2 mg), 2 wt% Ni/γ-Al_2O_3 (10 mg), and solvent 2-PrOH (40 μL) at ambient conditions. The MAS rate was set and maintained at 5 kHz. For hydrogenolysis with H_2, spectra were acquired with 16 scans, a relaxation delay of 10 s, and acquisition times of 300 ms (^{13}C) or 80 ms (^{1}H). In ^{13}C direct polarization experiments, a 35 kHz ^{1}H decoupling field was employed. When the temperature reached 225 °C, the rotor was kept at this temperature while an array of ^{13}C NMR spectra was collected for 14 h. For quantification, each transient represents 16 scans, acquired with a relaxation delay of 60 s, and an acquisition time of 300 ms. For the transfer hydrogenolysis reaction of BPE, all ^{13}C NMR spectra were acquired with 8 scans, a relaxation delay of 60 s, and acquisition time of 300 ms. Line broadening of 10 Hz was applied during processing.

2.4 Results and Discussion

2.4.1 Design of Rotors for High Temperature/Pressure Applications

The design[24] of the *WHiMS* rotor includes a cavern-style sleeve (Revolution NMR LLC), with one side permanently sealed by the closed ceramic end. The rotor dimensions are standard, and the sealing device occupies the same space as a traditional end cap. Since the sample space is the same as in a standard NMR cavern rotor (and just slightly reduced for the double O-ring versions - 140 μL for 5 mm rotors, and 400 μL for 7.5 mm rotors), the signal-to-noise ratio is not negatively affected by placing the sample further from the coil due to thicker rotor walls, extra ampoules/inserts, *etc*. The rotors have performed well in tests with a wide variety of samples, including solids (minerals, clays, porous catalysts), liquids (water, organic solvents), and gases (including supercritical fluids), Table S2.1.

Solid and liquid components are loaded prior to sealing with a “snap-in” bushing and then retained with a “hexagonal locking screw”, Scheme 2.1. The bushings have been constructed from various polymers (PEEK, Vespel, Torlon), and with a single or double O-ring; we have found that Vespel offers the highest combination of chemical and temperature resistance. All data in this paper were collected with Vespel bushings and double O-rings. Slits in the bushing allow the screw to flex inward during insertion until the locking ridge lines up with a matching groove machined into the rotor. The locking screw keeps the bushing expanded and therefore the ridge engaged. This design provides no impediment to sample loading and eventual cleaning that might be caused by the fixed structures found in earlier, screw-in designs.[7-8] Furthermore, the whole process can be easily carried out in an inert atmosphere glove box for air-sensitive samples. Once sealed, the rotor can be used as-is, or a gas can be added to the head space.

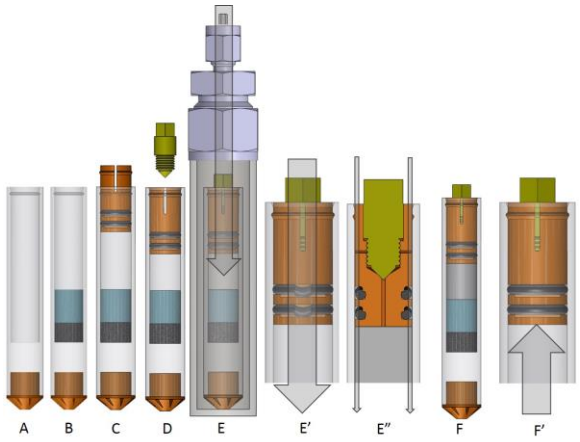

Scheme 2.1. Design of the high temperature/pressure *WHiMS* MAS rotors. A. Empty rotor; B. Rotor with solid and liquid samples added; C. Bushing installation; D. Locking screw installation, prevents gas escape through vent and retains bushing; E. Rotor in pressure vessel. E´. Close-up of check valve during pressurization. Gas (gray arrow) will flow into rotor and equalize with the pressure in the vessel by flexing the O-rings over cuts made into the O-ring grooves. E´´.Close-up/Cross-section view of check valve during pressurization. Rotor is shown rotated 90° from E´. Check valve cuts are placed 180° apart for balance resulting two paths for incoming gas (gray arrows). F. Pressurized rotor ready for NMR experiment with a three-phase reaction mixture, solid (black), liquid (blue) and gas (gray). F´. Close-up of check valve holding pressure with O-rings forced against unmodified side of the O-ring grooves by the internal pressure.

The new *WHiMS* rotor is pressurized via a one-way check valve built into the bushing, eliminating the need for mechanically opening or closing of a valve on the rotor. The assembled rotor is placed in a pressure vessel, which is then evacuated with a vacuum pump and backfilled with the desired gas, filling the rotor by equalizing the pressure, Scheme 2.1. For depressurization, the hexagonal locking screw can be loosened for quick and safe

release of the pressure through a pin-hole in the bushings. Bench testing of rotors with N_2 at room temperature shows that the 5 mm rotor is effective at holding ~400 bar (6000 psi) while the 7.5 mm rotor holds ~275 bar (4000 psi). The structural properties (tensile strength, flexural modulus, etc.) of the high temperature polymers used for the bushings typically decrease as the temperature rises: e.g., by approx. 50 % at 250 °C[33] for Vespel. Therefore, as the maximum temperature of the experiment increases, the maximum pressure limit must decrease. Using the limits and conditions presented here, ceramic sleeves and bushings have been cleaned and reused in excess of 20 times, while O-rings are typically replaced after 1-3 uses. The pressurizing chamber is commonly a section of stainless steel tubing – 0.375" for 5 mm rotors and 0.500" for 7.5 mm – capped on one end and fitted with a reducer (Swagelok) on the other, Scheme 2.1. Because it is not a piece of specialized equipment, it is easily sized to accommodate many rotors at once. Thus, highly reproducible samples can be prepared under identical gas pressure/temperature conditions.

2.4.2 Thermal Calibration

To calibrate the heating unit of the NMR probe, 40 μL ethylene glycol (EG) was loaded in a *WHiMS* rotor for use as the NMR thermometer. Liquid EG was used to mimic reaction conditions with solvent. Thermal calibration of NMR using EG is a classical method, however, the conventional calibration range is restricted to temperatures below 143 °C,[34] due to the buildup of vapor pressure as the temperature approaches the boiling point of EG (197.3 °C at ambient pressure). ^{1}H MAS-NMR spectra of EG from 25 to 250 °C are shown in Figure 2.1, and the chemical shift dependence on temperature is shown in Figures S2.1 and S2. The hydroxyl peak shifts to lower frequencies at higher temperatures, until it merges with the methylene resonance near the boiling point. Above that temperature, the shift to

lower frequencies continues. In this sealed rotor system, there are no new peaks indicating EG vaporization, even at 250 °C.

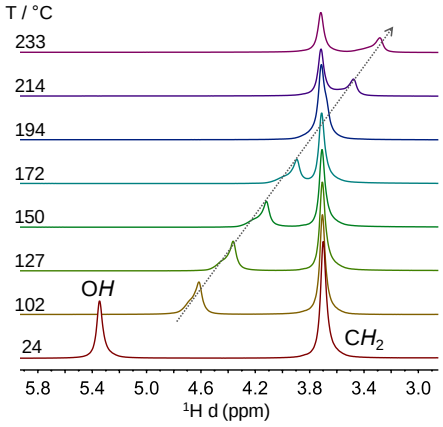

Figure 2.1. Variable temperature ^{1}H NMR spectra of ethylene glycol (EG) in a sealed *WHiMS* rotor. The indicated temperatures were calculated based on the chemical shift difference between the CH_2 and OH peaks.[35] Each spectrum was acquired at a MAS rate of 3 kHz with 4 scans, a relaxation delay of 5 s, and an acquisition time of 80 ms.

The temperature calibration was confirmed by recording the ^{207}Pb MAS NMR spectrum of solid $Pb(NO_3)_2$ in the range of 25 to 260 °C, Figure S2.3. The chemical shift changes linearly, moving to higher frequency with temperature.[36] The actual rotor temperature was calculated based on literature values for both EG[35] and $^{207}Pb(NO_3)_2$,[36] and the results agree well with each other, Figure S2.4.

2.4.3 Monitoring Phase Equilibria

Since volatile 2-PrOH was used as both the solvent and the reducing agent in the reaction studies described below, its phase behavior in the sealed rotor was examined. The 5 mm *WHiMS* rotor was loaded with 65 μL 2-PrOH, occupying 46 % of the total void space. After heating to the desired temperature, ^{13}C MAS-NMR were acquired (Figure 2.2). At

temperatures above 150 °C, two new, small peaks appear at lower frequency relative to the methyl and methine resonances, Figures 2.2 and S2.5. Their appearance is fully reversible; they disappear when the rotor is cooled. Therefore, we assign the new lines to vapor-phase 2-PrOH. All of the chemical shifts vary with temperature. When the calculated rotor temperature reaches 240 °C, the pairs of lines merge (methyl: 24.3 ppm; methine: 63.7 ppm), showing that there are no longer distinct chemical environments for the liquid and vapor phases. At 235.3 °C and 47 bar, 2-PrOH enters its supercritical phase.[37] At the highest temperature shown in Figure 2.2, the spectrum is consistent with the appearance of this supercritical phase.

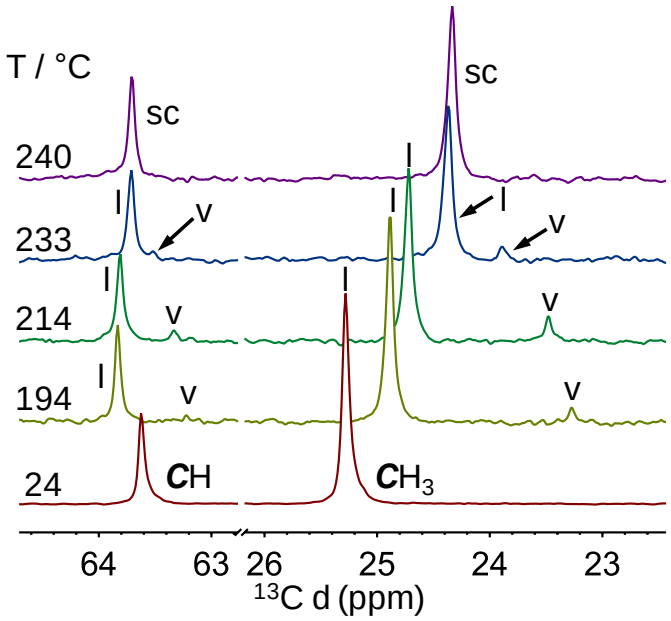

Figure 2.2. Variable temperature ^{13}C MAS-NMR spectra of 2-PrOH (65 μL) in a sealed *WHiMS* rotor (5 mm). Each spectrum was acquired at a MAS rate of 3 kHz with 16 scans, a relaxation delay of 5 s, and an acquisition time of 300 ms. Resonances corresponding to vapor, liquid, and supercritical species are denoted as v, l, and sc, respectively.

To verify the presence of supercritical 2-PrOH at 240 °C, the experiment was repeated with a smaller volume of 2-PrOH (40 μL), occupying only 28 % of the total space in the NMR rotor. In the ^{13}C NMR spectra (Figure S2.5a), vapor-phase peaks also appear in the spectra starting at 150 °C. Their intensities increase significantly as the temperature is raised, while the intensities for liquid-phase 2-PrOH decreased. At 240 °C, the liquid peaks disappear, leaving two lines for the methyl (23.8 ppm) and methine (63.5 ppm) groups. However, their chemical shifts differ significantly from those assigned to the supercritical state (see above). Since the pressure in the rotor caused by vaporization of the smaller amount of liquid is much lower, we suggest that all of the 2-PrOH exists in the vapor phase, rather than in the supercritical state.

In the variable temperature ^{1}H NMR spectra of liquid-phase 2-PrOH, Figure S2.5b, the chemical shifts of the methyl and methine do not vary greatly with temperature. However, the hydroxyl resonance, which appears at 5.2 ppm at 25 °C, shifts dramatically to lower frequency as the temperature increases, until at 240 °C it overlaps with the methyl signal at 1.0 ppm. The vapor-phase peaks for the methyl and methine protons are visible above 100 °C. In addition, a new line appears at 0.4 ppm and shifts to slightly higher frequency as the temperature increases. This is assigned to the hydroxyl proton of vapor-phase 2-PrOH, and the relative temperature-insensitivity of its chemical shift indicates that it experiences little if any intermolecular hydrogen bonding.[38] Above 225 °C, the chemical shift of the vapor phase hydroxyl proton matches that for the methyl protons. The disappearance of the liquid phase peaks also suggests that the sample is completely vaporized.

2.4.4 Direct Hydrogenolysis of Benzyl Phenyl Ether

The catalytic hydrogenolysis of the α-O-4 linkage in benzyl phenyl ether (BPE) gives toluene and phenol as primary products, Scheme 2.2. The reaction progress was monitored by MAS-NMR in a *WHiMS* rotor using selectively ^{13}C-labeled BPE. The reaction was conducted in 2-PrOH with Ni/γ-Al_2O_3 as the catalyst. *Operando* MAS-NMR spectra recorded during the reaction in the presence of an initial 121 bar H_2 are shown in Figures 2.3 and S2.6. In the ^{1}H spectrum recorded at 25 °C, the methylene appears as a doublet at 4.9 ppm, while the aromatic protons appear at 6.8-7.3 ppm. During the course of the non-isothermal experiment, the BPE spectrum gradually disappears and is replaced by new peaks for toluene and phenol as shown in Figure S2.9.

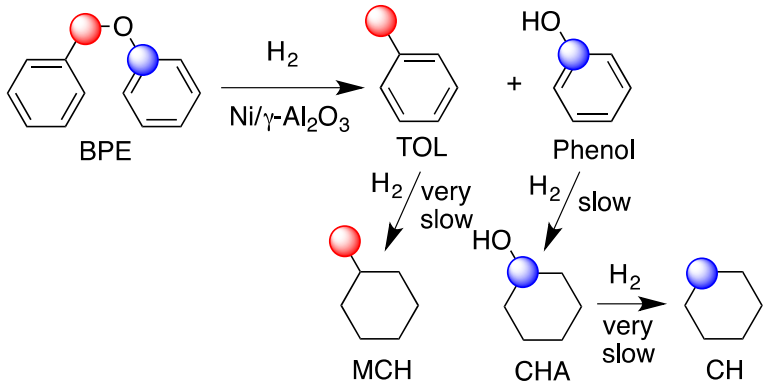

Scheme 2.2. Reaction mechanism for BPE hydrogenolysis at 225 °C, catalyzed by Ni/γ-Al_2O_3, showing the locations of the two ^{13}C labels (red and blue for the methylene and phenolate ^{13}C resonances in BPE, and labeled as BPE-B and BPE-P, respectively).

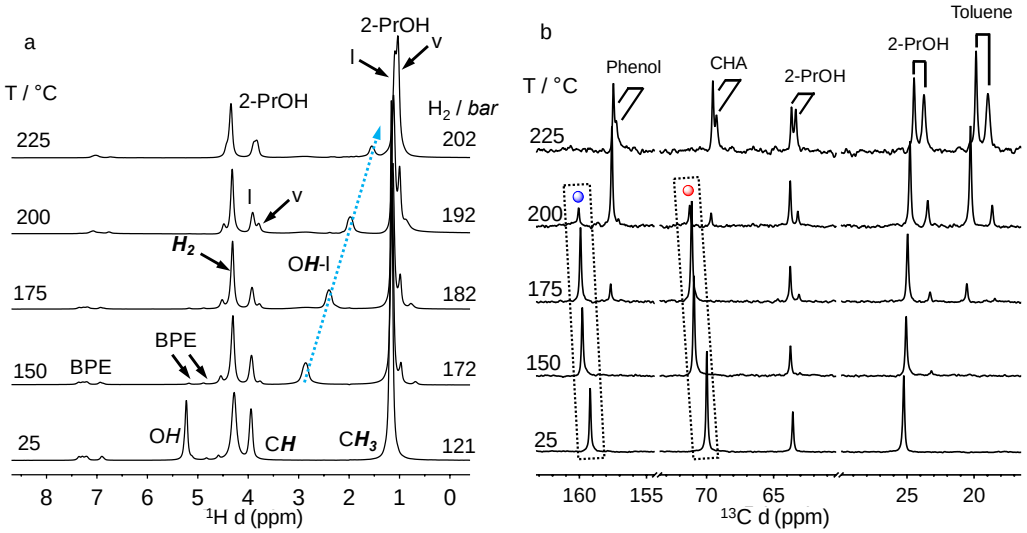

Figure 2.3. BPE hydrogenolysis in 2-PrOH observed at variable temperature, by (a) ^{1}H MAS-NMR and (b) ^{13}C MAS-NMR spectroscopy. The 5 mm *WHiMS* rotor contained ^{13}C-labeled BPE, ((phenoxy-^{13}C)-methyl-^{13}C) benzene, 2.0 mg), Ni/γ-Al_2O_3 (2 wt% Ni, 10.0 mg), and 2-PrOH (40 μL), and was pressurized with 121 bar H_2. The rotor was heated gradually to 150 °C, and was held at each temperature setpoint for 0.5 h before proceeding to the next temperature setpoint. After reaching 225 °C, the reaction was allowed to continue for 14 h. Spectra were acquired with 16 scans, a relaxation delay of 10 s, and acquisition time of 300 ms (^{13}C) or 80 ms (^{1}H), at an MAS rate of 5 kHz. In the ^{13}C spectra, all species are present as a pair of peaks, with the vapor phase at lower frequency than the liquid phase. The red and blue labels are defined in Scheme 2.2.

The conversion of BPE to toluene and phenol is observed more readily in the ^{13}C MAS-NMR spectrum, Figure 2.3b. At 25 °C, the resonances of the ^{13}C-enriched methylene and phenolate-C^{1} carbons of BPE are visible at 70.1 and 159.3 ppm, respectively. As in the ^{1}H spectral array, the conversion of BPE to toluene-α-^{13}C (20.8 ppm) and phenol-1-^{13}C (157.8 ppm) is observed to commence at ca. 150 °C. At elevated temperatures, the spectrum of

vapor-phase 2-PrOH (as described in Figure 2.2) is also visible. Nearly complete conversion of BPE was achieved at 200 °C.

Some hydrogenation of phenol-1-^{13}C to cyclohexanol-1-^{13}C (69.7 ppm) was also observed at this temperature, Scheme 2.2. When the temperature was raised to 225 °C (and 202 bar H_2), complete conversion of BPE was observed, and phenol was fully hydrogenated to cyclohexanol-1-^{13}C. In addition, hydrogenation of toluene-α-^{13}C to cyclohexane-methyl-^{13}C occurred to a small extent (ca. 12 % in 14 h at 225 °C), as judged by the appearance of a peak at 21.1 ppm in Figure S2.6. Previously, aromatic hydrogenation was reported to be promoted by the Lewis acid sites of Ni/γ-Al_2O_3, where adsorption of the aromatic ring onto an acid site was shown to be important in the formation of cyclohexanol-1-^{13}C from phenol-1-^{13}C.[39] After 14 h, further conversion (ca. 7 %) of cyclohexanol-1-^{13}C to cyclohexane-^{13}C was also observed via a peak at 27.3 ppm in Figure 2.3 (confirmed via the spectrum of the standard in Figure S2.7). Cyclohexanol undergoes slow, acid-catalyzed dehydration to cyclohexene followed by rapid hydrogenation to yield cyclohexane, thus the cyclohexene intermediate is unlikely to be detected.[40] The reverse process of cyclohexene rehydration does not occur under these conditions, since the hydroxyl group of the observed cyclohexanol remains at the labeled C1 position. The appearance of methylcyclohexane-methyl-^{13}C (from toluene hydrogenation) was also observed during the catalytic hydrogenolysis of ^{13}C-labeled BPE at 251 ºC with 213 bar H_2 (Figure S2.8). The presence of unreacted H_2 is also evident after completion of the reaction (Figure S2.9).

2.4.5 Transfer Hydrogenolysis of Benzyl Phenyl Ether

The hydrogenolysis of BPE proceeds slowly even in the absence of added H_2, Scheme 2.3, because of the reducing nature of the 2-PrOH solvent. The longer timescale makes it

convenient to acquire kinetic profiles for these reaction conditions by MAS-NMR. Ni/γ-Al_2O_3 catalyzes the oxidation of 2-PrOH efficiently at temperatures in excess of 200 °C. At 225 °C, BPE hydrogenolysis in 2-PrOH without added H_2 was observed in the NMR rotor, Figure 2.4a. At the end of the experiment, ^{13}C NMR spectrum of acetone was detected with peaks at 207.5 and 30.6 ppm, Figure S2.10. In the absence of BPE, no acetone was detected, even after heating the rotor to 260 °C, thus dehydrogenation of 2-PrOH occurs to an appreciable extent only in the presence of a hydrogen acceptor.

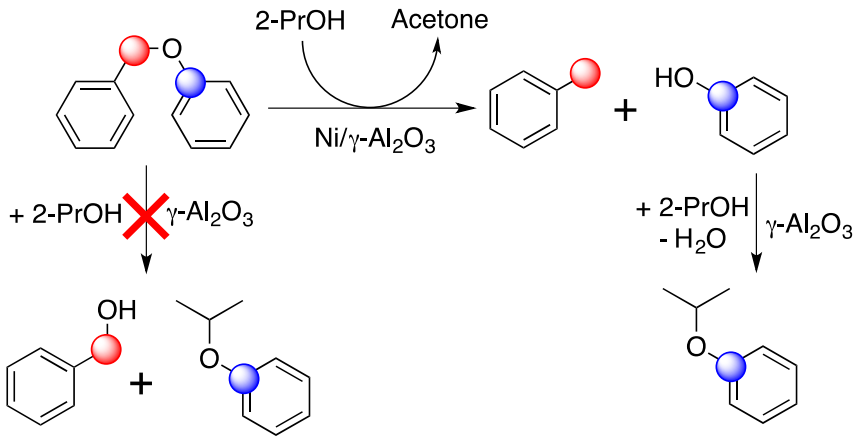

Scheme 2.3. Proposed mechanism of catalytic BPE hydrogenolysis by transfer hydrogenolysis.

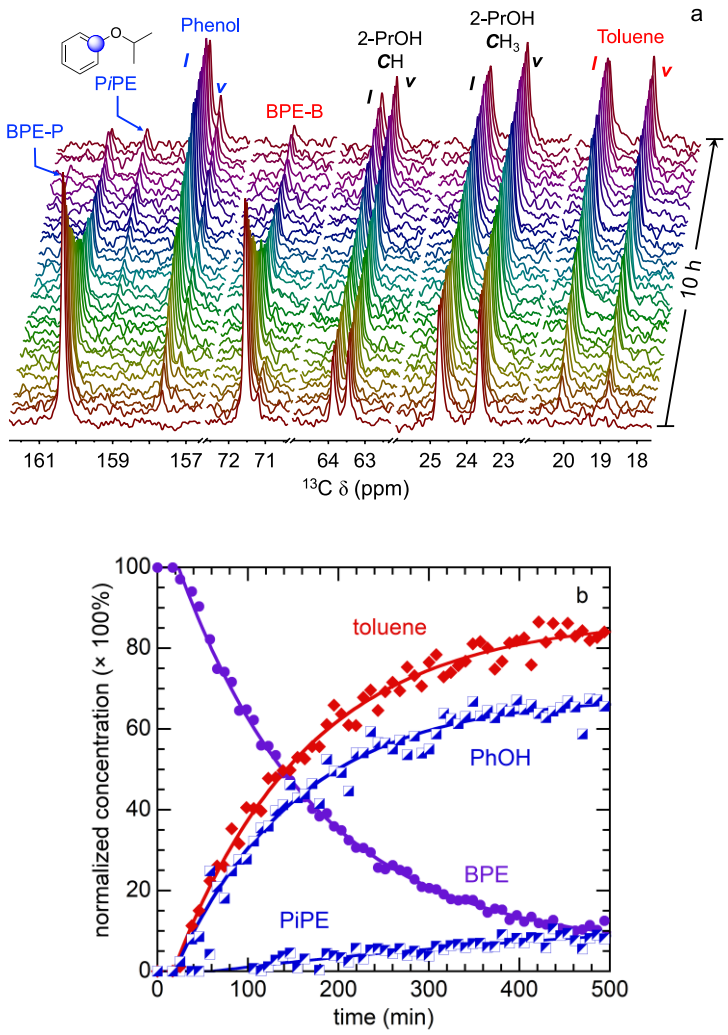

Figure 2.4. (a) ^{13}C MAS-NMR spectra recorded during hydrogenolysis of BPE in 2-PrOH in a solid-state NMR rotor at 225 ºC without added H_2, and (b) kinetic profiles extracted from the NMR spectra, for BPE (average of BPE-P and BPE-B), phenol (sum of vapor and liquid species), and toluene (sum of vapor and liquid species). Methylene and phenolate ^{13}C resonances in BPE are labeled as BPE-B (red) and BPE-P (blue), respectively. The rotor was loaded with ^{13}C-labeled BPE (2.0 mg), Ni/γ-Al_2O_3 (2 wt%, 10.0 mg), and 2-PrOH (40 μL). Direct polarization ^{13}C spectra were acquired with 8 scans, a relaxation delay of 60 s, and acquisition time of 300 ms, at an MAS rate of 5 kHz.

The ratio of the areas for each pair of liquid and vapor phase peaks remained constant throughout the course of reaction, demonstrating that the rotor remained sealed and the total pressure was constant. The fractions of phenol and toluene that exist in the vapor phase under these conditions are *ca.* 14 and 39 %, respectively. Complete conversion of BPE required about 10 h. All of the reaction profiles are pseudo-first-order, Figure 2.4b, with rate constants shown in Table 2.1. Phenol hydrogenation to cyclohexanol is not evident, suggesting that arene hydrogenation occurs only in the presence of significant H_2 pressure. Therefore, the use of 2-PrOH as an alternative hydrogen source promotes selective BPE hydrogenolysis and preserves the aromaticity of the products.

Table 2.1. Pseudo-first-order rate constants for BPE conversion in 2-PrOH at 225 °C catalyzed by 2 wt% Ni/γ-Al_2O_3, without added H_2

Kinetic profile	10^3 k_{obs} (min^{-1})[a]
BPE conversion	6.5(1)
Formation of toluene	6.8(3)
Formation of phenol	7.3(4)

[a] Obtained by fitting the pseudo-first-order rate equation to concentration profiles obtained in *operando* MAS-NMR experiments.

In transfer hydrogenolysis, phenyl isopropyl ether (P*i*PE, labeled at the phenolic carbon and observed at 158.3 ppm) is a minor product, with a yield of 10 % relative to the initial BPE concentration after 10 h. The assignment was confirmed by collecting the NMR spectrum of a P*i*PE standard, Figure S2.11. In addition, the GC-MS chromatogram of the reaction mixture recorded after cooling to room temperature contains a peak with the expected m/z = 137.0 (molecular ion) for P*i*PE, Figure S2.12. Notably, the ^{13}C NMR signal

is detected late in the spectral array, when a significant amount of phenol has already accumulated in the rotor. This suggests that P*i*PE is a secondary product, formed by etherification of the primary reaction product phenol rather than by direct solvolysis of BPE. Etherification may be catalyzed by the acid sites of γ-Al_2O_3 (Scheme 2.3).[41]

2.5 Conclusions

We developed the new *WHiMS* rotors for MAS-NMR applications requiring combined high temperatures and pressures (in excess of 200 bar at 250 °C), and demonstrated their use for *in situ* and *operando* studies of complex mixtures. Because both phase transitions and chemical reactions can be probed with excellent resolution, local chemical environments can be correlated with different functional groups. For example, *in situ* spectra of 2-PrOH collected at variable temperatures display both liquid- and vapor-phase resonances at high resolution. At higher temperatures, the liquid and vapor phase peaks may merge as the supercritical phase is formed. The remarkable robustness of *WHiMS* MAS rotor and seal is demonstrated by the ability to contain supercritical fluids known for solvating polymers.

The rotor allowed the acquisition of high-resolution and time-resolved MAS-NMR spectra during the catalytic hydrogenolysis of a lignin model compound, in the presence of an alcohol as solvent as reducing agent. Spectra were also recorded when the rotor was pressurized with 121 bar H_2. The use of selectively ^{13}C-labeled compounds makes it possible to follow specific functional groups independently as their concentrations evolved during the reaction. In the case of BPE hydrogenolysis, labeled methylene and phenolic carbons were tracked as they were converted first to toluene and phenol, then to methylcyclohexane and cyclohexanol, respectively. The aromaticity of the reaction products can be preserved by controlling the temperature and H_2 pressure.

The *WHiMS* MAS rotor should find applications in the molecular-level study of dynamics and reactions at interfaces, which are of paramount importance in electrochemistry, waste-water treatment, environmental processes that occur on natural mineral and particle surfaces, interactions of surfactants used in shale gas exploration and extraction, *etc*. In addition to the 7.5 mm and 5 mm rotors currently in use, we have developed 6 mm and 4 mm prototypes, which will increase compatibility with additional spectrometers and, in the case of 4 mm rotors, higher magnetic fields.

2.6 References

(1) Oliver, F. G.; Munson, E. J.; Haw, J. F. High-Temperature In-Situ Magic Angle Spinning NMR Studies of Chemical Reactions on Catalysts. *J. Phys. Chem.* **1992**, *96*, 8106-8111.

(2) Foley, D. A.; Bez, E.; Codina, A.; Colson, K. L.; Fey, M.; Krull, R.; Piroli, D.; Zell, M. T.; Marquez, B. L. NMR Flow Tube for Online NMR Reaction Monitoring. *Anal. Chem.* **2014**, *86*, 12008-12013.

(3) Hu, J. Z.; Sears, J. A.; Mehta, H. S.; Ford, J. J.; Kwak, J. H.; Zhu, K.; Wang, Y.; Liu, J.; Hoyt, D. W.; Peden, C. H. F. A Large Sample Volume Magic Angle Spinning Nuclear Magnetic Resonance Probe for in Situ Investigations with Constant Flow of Reactants. *PCCP* **2012**, *14*, 2137-2143.

(4) Surface, J. A.; Skemer, P.; Hayes, S. E.; Conradi, M. S. In Situ Measurement of Magnesium Carbonate Formation from CO_2 using Static High-Pressure and-Temperature ^{13}C NMR. *Environ. Sci. Technol.* **2012**, *47*, 119-125.

(5) Ok, S.; Hoyt, D. W.; Andersen, A.; Sheets, J.; Welch, S. A.; Cole, D. R.; Mueller, K. T.; Washton, N. M. Surface Interactions and Confinement of Methane: A High

Pressure Magic Angle Spinning NMR and Computational Chemistry Study. *Langmuir* **2017**, *33*, 1359-1367.

(6) Qi, L.; Alamillo, R.; Elliott, W. A.; Andersen, A.; Hoyt, D. W.; Walter, E. D.; Han, K. S.; Washton, N. M.; Rioux, R. M.; Dumesic, J. A.; Scott, S. L. Operando Solid-State NMR Observation of Solvent-Mediated Adsorption-Reaction of Carbohydrates in Zeolites. *ACS Catal.* **2017**, 3489-3500.

(7) Hoyt, D. W.; Turcu, R. V. F.; Sears, J. A.; Rosso, K. M.; Burton, S. D.; Felmy, A. R.; Hu, J. Z. High-Pressure Magic Angle Spinning Nuclear Magnetic Resonance. *J. Magn. Reson.* **2011**, *212*, 378-385.

(8) Turcu, R. V.; Hoyt, D. W.; Rosso, K. M.; Sears, J. A.; Loring, J. S.; Felmy, A. R.; Hu, J. Z. Rotor Design for High Pressure Magic Angle Spinning Nuclear Magnetic Resonance. *J. Magn. Reson.* **2013**, *226*, 64-69.

(9) Hoyt, D. W.; Sears, J. A.; Turcu, R. V.; Rosso, K. M.; Hu, J. Z. Devices and Process for High-Pressure Magic Angle Spinning Nuclear Magnetic Resonance. Patent 8,692,548, 2014.

(10) Hu, J. Z.; Hu, M. Y.; Zhao, Z.; Xu, S.; Vjunov, A.; Shi, H.; Camaioni, D. M.; Peden, C. H. F.; Lercher, J. A. Sealed Rotors for in Situ High Temperature High Pressure MAS NMR. *Chem. Commun.* **2015**, *51*, 13458-13461.

(11) Hoyt, D. W.; Hu, J. Z.; Sears, J. A.; Walter, E. D.; Mehta, H. S.; Rosso, K. M.; Turcu, R. V. F., Pressurized Magic Angle Spinning (PMAS) Technology for Nuclear Magnetic Resonance (NMR) Spectroscopy *R&D Magazine* 2015.

(12) Hoyt, D. W.; Sears, J. A.; Turcu, R. V.; Rosso, K. M.; Hu, J. Z. Devices and Process for High-Pressure Magic Angle Spinning Nuclear Magnetic Resonance. Patent 9,835,698 2017.

(13) Loring, J. S.; Schaef, H. T.; Turcu, R. V. F.; Thompson, C. J.; Miller, Q. R. S.; Martin, P. F.; Hu, J.; Hoyt, D. W.; Qafoku, O.; Ilton, E. S.; Felmy, A. R., et al. In Situ Molecular Spectroscopic Evidence for CO_2 Intercalation into Montmorillonite in Supercritical Carbon Dioxide. *Langmuir* **2012**, *28*, 7125-7128.

(14) Miller, Q. R. S.; Thompson, C. J.; Loring, J. S.; Windisch, C. F.; Bowden, M. E.; Hoyt, D. W.; Hu, J. Z.; Arey, B. W.; Rosso, K. M.; Schaef, H. T. Insights into Silicate Carbonation Processes in Water-Bearing Supercritical CO_2 Fluids. *Int. J. Greenhouse Gas Control* **2013**, *15*, 104-118.

(15) Bowers, G. M.; Hoyt, D. W.; Burton, S. D.; Ferguson, B. O.; Varga, T.; Kirkpatrick, R. J. In Situ ^{13}C and ^{23}Na Magic Angle Spinning NMR Investigation of Supercritical CO_2 Incorporation in Smectite–Natural Organic Matter Composites. *J. Phys. Chem. C* **2014**, *118*, 3564-3573.

(16) Kwak, J. H.; Hu, J. Z.; Hoyt, D. W.; Sears, J. A.; Wang, C.; Rosso, K. M.; Felmy, A. R. Metal Carbonation of Forsterite in Supercritical CO_2 and H_2O using Solid State ^{29}Si, ^{13}C NMR Spectroscopy. *J. Phys. Chem. C* **2010**, *114*, 4126-4134.

(17) Kwak, J. H.; Hu, J. Z.; Turcu, R. V.; Rosso, K. M.; Ilton, E. S.; Wang, C.; Sears, J. A.; Engelhard, M. H.; Felmy, A. R.; Hoyt, D. W. The role of H_2O IN THECarbonation of Forsterite in Supercritical CO_2. *Int. J. Greenhouse Gas Control* **2011**, *5*, 1081-1092.

(18) Bowers, G. M.; Schaef, H. T.; Loring, J. S.; Hoyt, D. W.; Burton, S. D.; Walter, E. D.; Kirkpatrick, R. J. Role of Cations in CO_2 Adsorption, Dynamics, and Hydration in Smectite Clays under in Situ Supercritical CO_2 Conditions. *J. Phys. Chem. C* **2017**, *121*, 577-592.

(19) Schaef, H. T.; Loganathan, N.; Bowers, G. M.; Kirkpatrick, R. J.; Yazaydin, A. O.; Burton, S. D.; Hoyt, D. W.; Thanthiriwatte, K. S.; Dixon, D. A.; McGrail, B. P. Tipping Point for Expansion of Layered Aluminosilicates in Weakly Polar Solvents: Supercritical CO_2. *ACS Appl. Mater. Interfaces* **2017**.

(20) White, M. D.; McGrail, B. P.; Schaef, H. T.; Hu, J. Z.; Hoyt, D. W.; Felmy, A. R.; Rosso, K. M.; Wurstner, S. K. Multiphase Sequestration Geochemistry: Model for Mineral Carbonation. *Energy Procedia* **2011**, *4*, 5009-5016.

(21) Wilkins, M. J.; Hoyt, D. W.; Marshall, M. J.; Alderson, P. A.; Plymale, A. E.; Markillie, L. M.; Tucker, A. E.; Walter, E. D.; Linggi, B. E.; Dohnalkova, A. C. CO_2 Exposure at Pressure Impacts Metabolism and Stress Responses in the Model Sulfate-Reducing Bacterium Desulfovibrio Vulgaris Strain Hildenborough. *Front. Microbiol.* **2014**, *5*.

(22) Vjunov, A.; Hu, M. Y.; Feng, J.; Camaioni, D. M.; Mei, D.; Hu, J. Z.; Zhao, C.; Lercher, J. A. Following Solid-Acid-Catalyzed Reactions by MAS NMR Spectroscopy in Liquid Phase—Zeolite-Catalyzed Conversion of Cyclohexanol in Water. *Angew. Chem. Int. Ed.* **2014**, *53*, 479-482.

(23) Zhao, Z.; Shi, H.; Wan, C.; Hu, M. Y.; Liu, Y.; Mei, D.; Camaioni, D. M.; Hu, J. Z.; Lercher, J. A. Mechanism of Phenol Alkylation in Zeolite H-BEA Using In Situ Solid-State NMR Spectroscopy. *J. Am. Chem. Soc.* **2017**, *139*, 9178-9185.

(24) Walter, E.; Sears, J.; Mehta, H.; Hoyt, D. Snap-In Bushings and Process for High-Pressure And/Or High Temperature Magic Angle Spinning Nuclear Magnetic Resonance. US Patent Pending – No. 15/225,688 Filed August 1, 2016.

(25) Jung, H. B.; Carroll, K.; Kabilan, S.; Heldebrant, D. J.; Hoyt, D.; Zhong, L.; Varga, T.; Stephens, S.; Adams, L.; Bonneville, A. Stimuli-Responsive/Rheoreversible

Hydraulic Fracturing Fluids as a Greener Alternative to Support Geothermal and Fossil Energy Production. *Green Chem.* **2015**, *17*, 2799-2812.

(26) Kim, S.; Chmely, S. C.; Nimlos, M. R.; Bomble, Y. J.; Foust, T. D.; Paton, R. S.; Beckham, G. T. Computational Study of Bond Dissociation Enthalpies for a Large Range of Native and Modified Lignins. *J. Phys. Chem. Lett.* **2011**, *2*, 2846-2852.

(27) Jyothi, T. M.; Raja, T.; Talawar, M. B.; Sreekumar, K.; Sugunan, S.; Rao, B. S. NiO-Al_2O_3 Prepared from a Ni-Al Hydrotalcite Precursor as an Efficient Catalyst for Transfer Hydrogenation Reactions. *Synth. Commun.* **2000**, *30*, 1573-1579.

(28) Sergeev, A. G.; Webb, J. D.; Hartwig, J. F. A Heterogeneous Nickel Catalyst for the Hydrogenolysis of Aryl Ethers without Arene Hydrogenation. *J. Am. Chem. Soc.* **2012**, *134*, 20226-20229.

(29) Wang, X.; Rinaldi, R. Exploiting H-Transfer Reactions with RANEY® Ni for Upgrade of Phenolic and Aromatic Biorefinery Feeds Under Unusual, Low-Severity Conditions. *Energy Environ. Sci.* **2012**, *5*, 8244-8260.

(30) Mathew, K. M.; Ravi, S.; Unny, V. K. P.; Sivaprasad, N. Microwave-Assisted Synthesis of (RS) methyl-2-([2′-14C]4,6-dimethoxypyrimidin-2′-yloxy)-2-phenyl [1-^{14}C]ethanoate. *J. Labelled Compd. Radiopharm.* **2006**, *49*, 699-705.

(31) Wu, W.-B.; Huang, J.-M. Electrochemical Cleavage of Aryl Ethers Promoted by Sodium Borohydride. *J. Org. Chem* **2014**, *79*, 10189-10195.

(32) Goula, M. A.; Charisiou, N. D.; Papageridis, K. N.; Delimitis, A.; Pachatouridou, E.; Iliopoulou, E. F. Nickel on Alumina Catalysts for the Production of Hydrogen Rich Mixtures via the Biogas Dry Reforming Reaction: Influence of the Synthesis Method. *Int. J. Hydrogen Energy* **2015**, *40*, 9183-9200.

(33) Rabilloud, G., *High-Performance Polymers: Chemistry and Applications*; Editions Technip, 1997; Vol. 2.

(34) Ammann, C.; Meier, P.; Merbach, A. A Simple Multinuclear NMR Thermometer. *J. Magn. Reson.* **1982**, *46*, 319-321.

(35) Hoffman, R. E.; Becker, E. D. Temperature Dependence of the ^{1}H Chemical Shift of Tetramethylsilane in Chloroform, Methanol, and Dimethylsulfoxide. *J. Magn. Reson.* **2005**, *176*, 87-98.

(36) Bielecki, A.; Burum, D. P. Temperature dependence of ^{207}Pb MAS spectra of solid lead nitrate. An accurate, sensitive thermometer for variable-temperature MAS. *J. Magn. Reson., Ser A* **1995**, *116*, 215-220.

(37) Tsukahara, T.; Harada, M.; Tomiyasu, H.; Ikeda, Y. NMR Studies on Effects of Temperature, Pressure, and Fluorination on Structures and Dynamics of Alcohols in Liquid and Supercritical States. *J. Phys. Chem. A* **2008**, *112*, 9657-9664.

(38) Aizawa, T.; Sato, O.; Ikushima, Y.; Hatakeda, K.; Saito, N. An In Situ High-Pressure NMR Study of Hydrogen Bonding of Alcohols in Supercritical Carbon Dioxide. *Rev. High-Pressure Sci. Technol.* **1998**, *7*, 1426-1428.

(39) Hu, S.; Xue, M.; Chen, H.; Shen, J. The Effect of Surface Acidic and Basic Properties on the Hydrogenation of Aromatic Rings over the Supported Nickel Catalysts. *Chem. Eng. J.* **2010**, *162*, 371-379.

(40) Mortensen, P. M.; Grunwaldt, J.-D.; Jensen, P. A.; Jensen, A. D. Screening of Catalysts for Hydrodeoxygenation of Phenol as a Model Compound for Bio-oil. *ACS Catal.* **2013**, *3*, 1774-1785.

(41) Larmier, K.; Chizallet, C.; Cadran, N.; Maury, S. A., J.; Lamic-Humblot, A.-F.; Marceau, E.; Lauron-Pernot, H. Mechanistic Investigation of Isopropanol

Conversion on Alumina Catalysts: Location of Active Sites for Alkene/Ether Production. *ACS Catal.* **2015**, *5*, 4423-4437.

2.7 Appendix I

Table S2.1. Applications of *WHiMS* rotors

System	Solvent	Gas	Rotor (mm)	H Field (MHz)	Pressure (bar)	Temp °C[a]	ref
Bio-oil upgrading	Pyrolysis oil	N_2 or H_2	7.5	300	138	180	*
Geothermal Fracturing	Water	CO_2	5	300	275	130	1
Lignin/model compound decomposition	2-propanol	H_2	5	500	213	250	2
	2-propanol	H_2	7.5	300	150	250	
Biomass conversion	Water/GVL[b]	N_2	5	850	72	150	3
	Water/GVL[b]	N_2	7.5	500	72	150	
Temperature reference	Ethylene glycol		5	500	-	250	2
			7.5	300	-	225	
MOF[c]	THF[d]	H_2	5	500	80	220	*
Mineral/clay	water	Supercritical CO_2 or CH_4	5	500	90	50	4

[a] Temperature of sample as measured by lead nitrate standard; temperature of VT gas was 5-15 °C higher. [b] GVL – gamma-Valerolactone. [c] MOF – Metal Organic Framework. [d] THF – tetrahydrofuran. * - unpublished results.

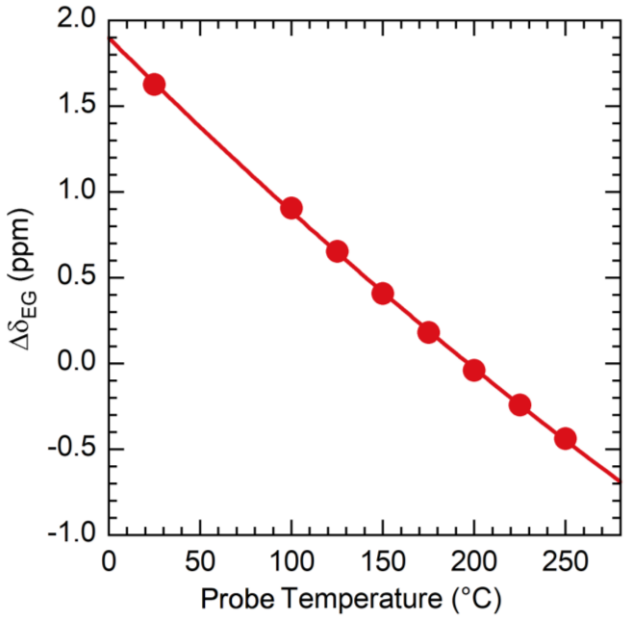

Figure S2.1. Temperature dependence of the chemical shift difference between the CH_2 and OH signals of ethylene glycol (EG). The data were collected with a 5mm *WHiMS* rotor. Each ^1H NMR spectrum (500.1822 MHz) was acquired at a MAS rate of 3 kHz with 4 scans, a relaxation delay of 5 s, and an acquisition time of 80 ms.

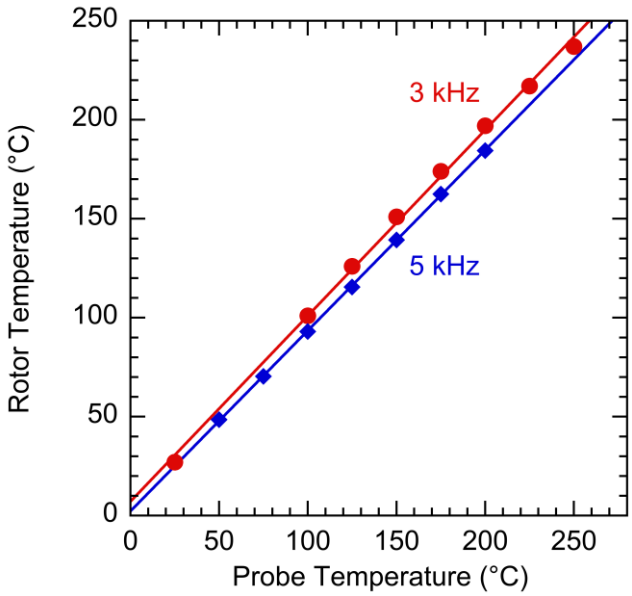

Figure S2.2. Temperature of the NMR rotor, calculated using EG as the NMR thermometer at different set temperatures, recorded using two MAS rates. Each spectrum was acquired with 4 scans, a relaxation delay of 5 s, and an acquisition time of 80 ms. The rotor temperatures indicated were calculated based on the chemical shift difference between the CH_2 and OH signals of EG.[5]

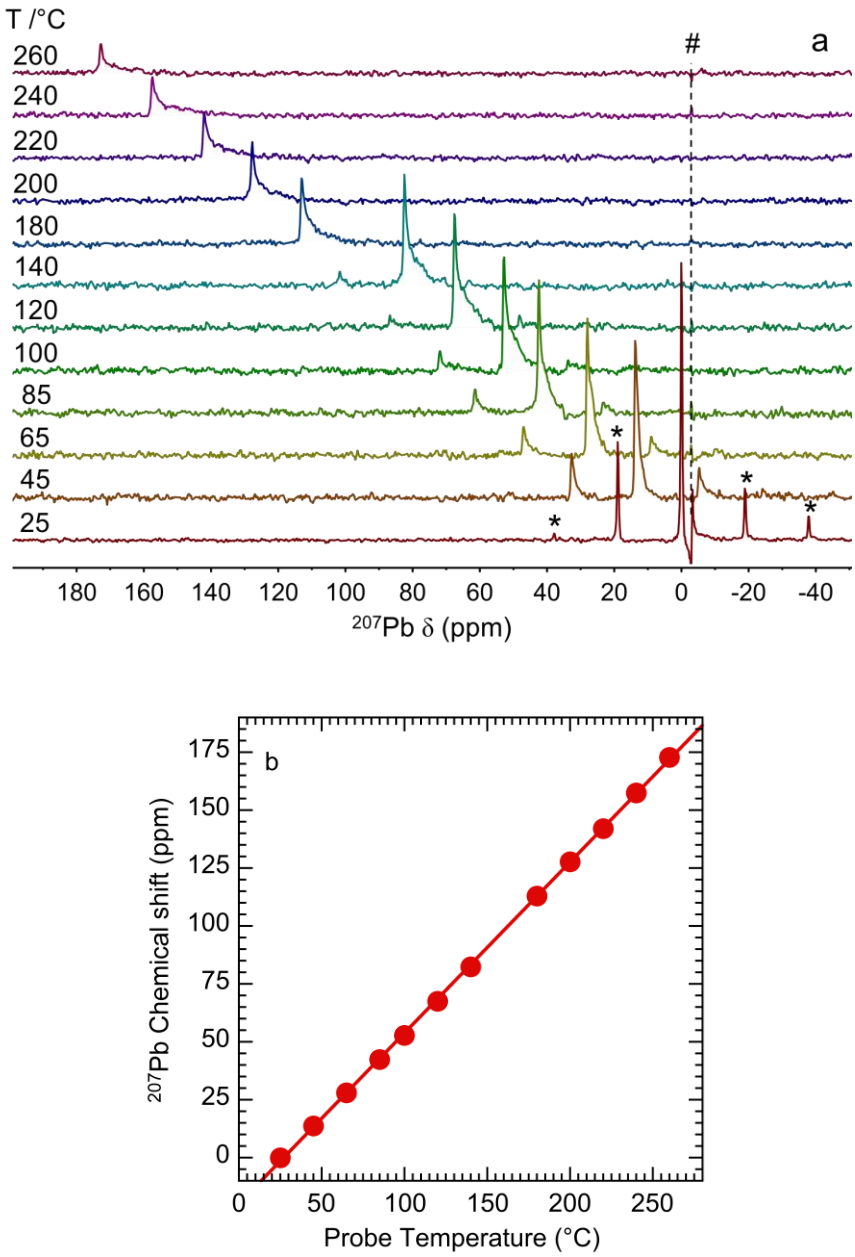

Figure S2.3. (a) ^{207}Pb NMR spectra of $Pb(NO_3)_2$, and (b) temperature dependence of ^{207}Pb shift. The ^{207}Pb chemical shift is defined as 0 ppm at 25 °C. All spectra were acquired at an MAS rate of 2 kHz with 4 scans, a relaxation delay of 1 s, and an acquisition time of 20 ms. Line broadening of 25 Hz was applied. The wiggle (#) in the ^{207}Pb NMR spectra is an artifact at the transmitter frequency. Asterisks on the 25 °C spectrum indicate spinning side bands.

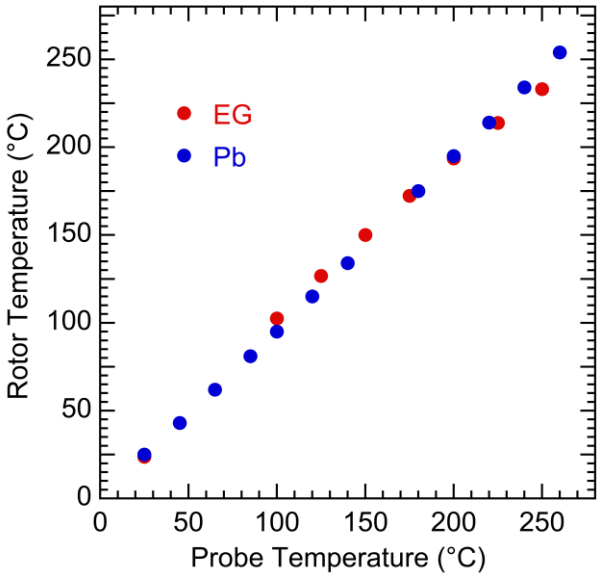

Figure S2.4. Comparison of rotor temperature calibrations using the NMR thermometers EG or $Pb(NO_3)_2$. In experiments with EG, rotor temperatures were calculated based on the chemical shift difference between the CH_2 and OH signals.[5] In experiments with $Pb(NO_3)_2$, rotor temperatures were calculated using the chemical shift of the ^{207}Pb signal.[6]

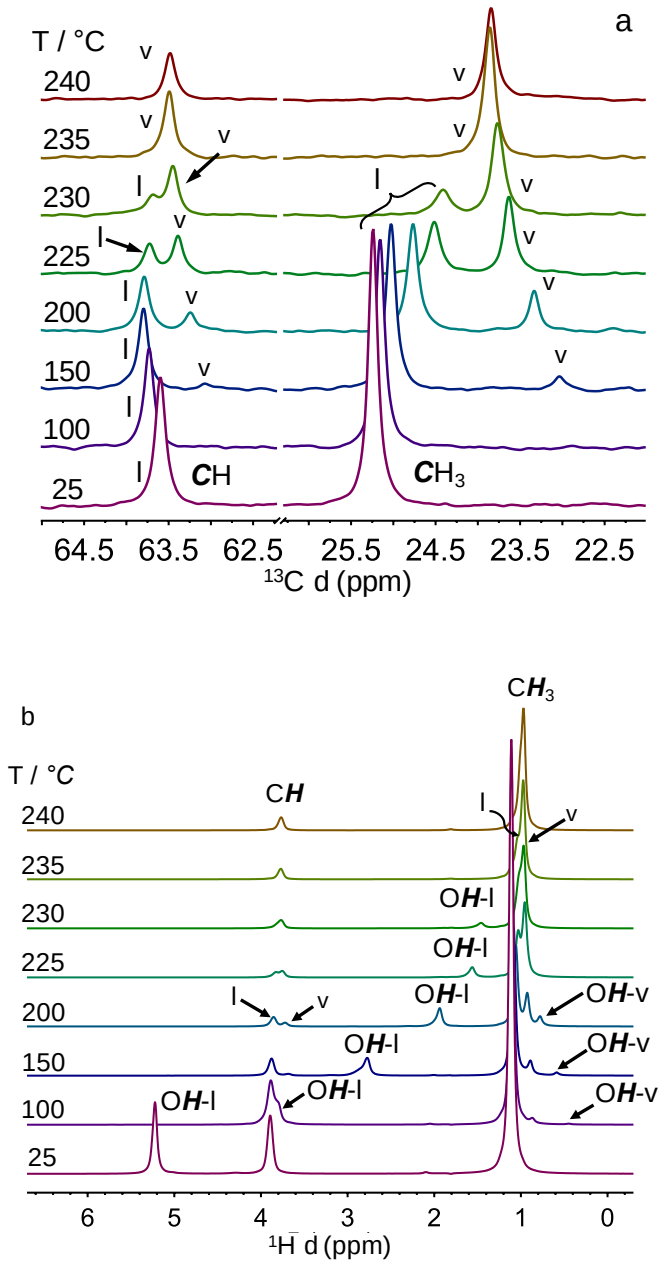

Figure S2.5. Variable temperature MAS-NMR of 2-PrOH (40 μL) in a 5 mm *WHiMS* rotor: (a) ^{13}C NMR spectra, and (b) ^{1}H MAS NMR spectra. ^{1}H NMR spectra were acquired with 16 scans, 10 s of relaxation delay, 300 ms of acquisition time, and were processed with a line broadening of 10 Hz. ^{13}C spectra were acquired with 16 scans, a relaxation delay of 60 s, an acquisition time of 300 ms, and were processed with a line broadening of 10 Hz. Signals of liquid phase and vapor phase species are denoted with (l) and (v), respectively.

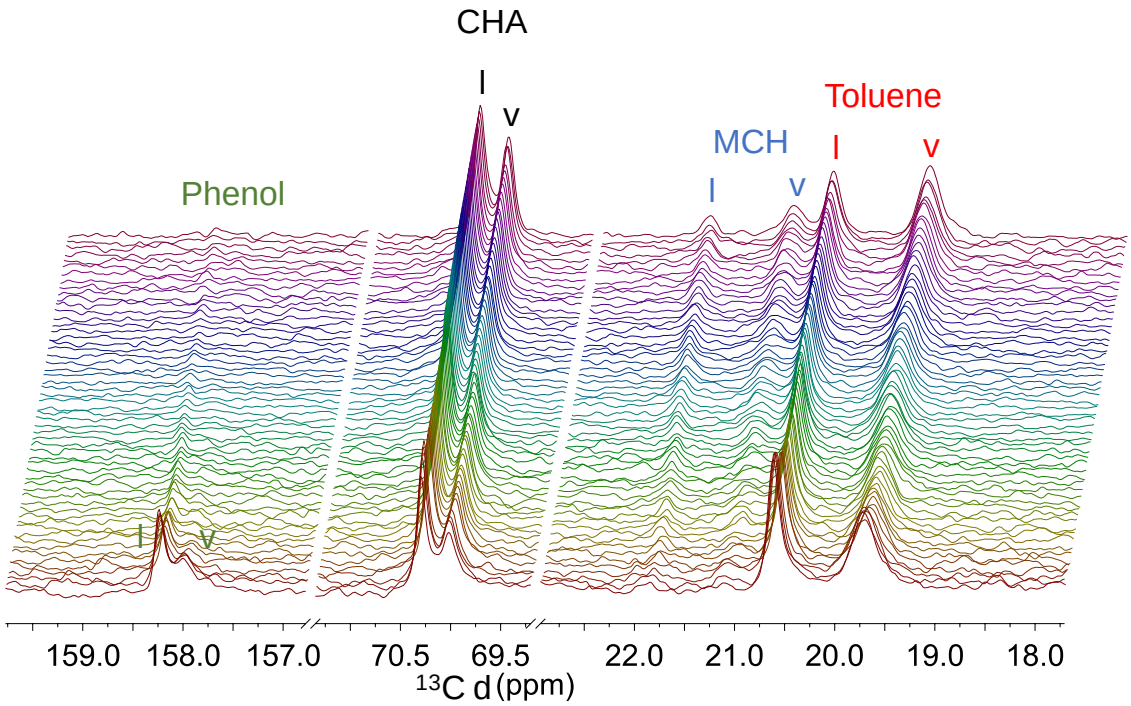

Figure S2.6. *Operando* ^{13}C MAS-NMR spectra, recorded during hydrogenolysis of BPE in 2-PrOH in an NMR rotor at 225 ºC and ~202 bar showing the hydrogenation of phenol and toluene to cyclohexanol (CHA) and methylcyclohexane (MCH), respectively. The rotor contained ^{13}C-labeled BPE (2.0 mg), Ni/γ-Al_2O_3 (2 wt% Ni, 10.0 mg), and 2-PrOH (40 μL), and was pressurized at 25 ºC with 121 bar H_2. The spectra were acquired with 16 scans, a relaxation delay of 10 s, and acquisition time of 300 ms (^{13}C) or 80 ms (^{1}H), at an MAS rate of 5 kHz for 14 h. Line broadening of 10 Hz was applied during processing. Signals of liquid phase and vapor phase species are denoted with (l) and (v), respectively.

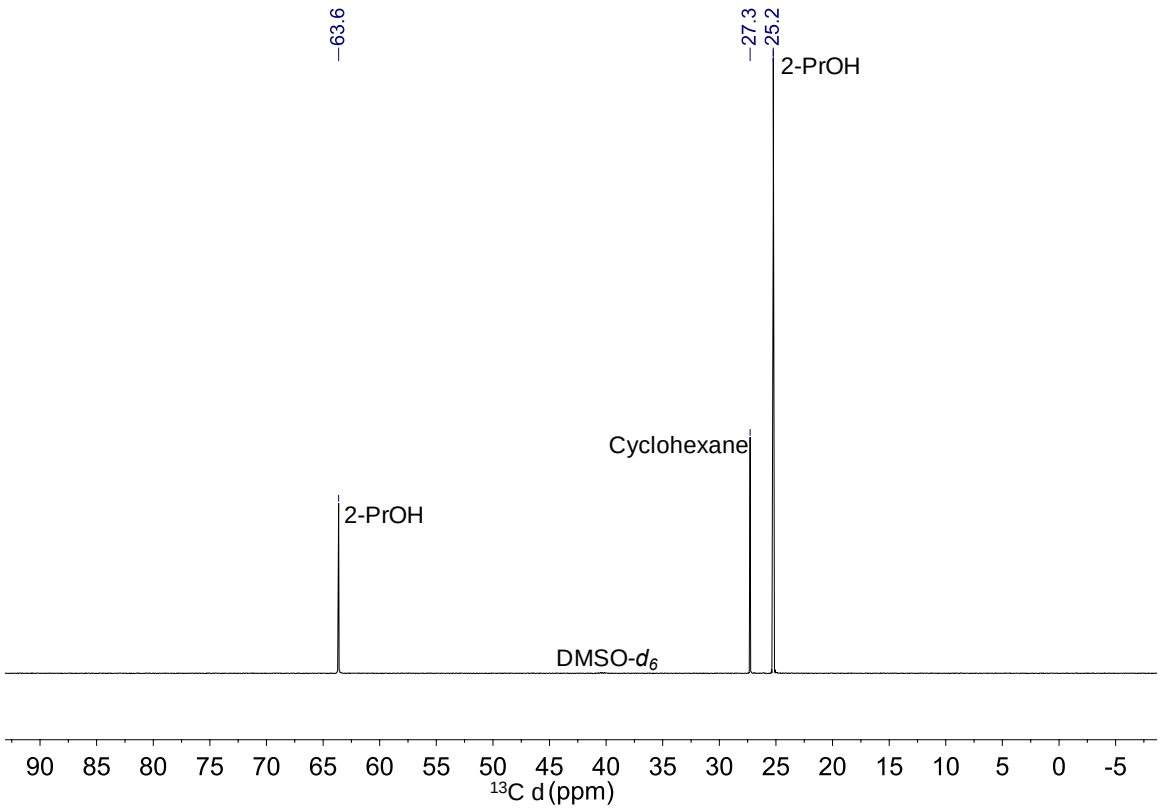

Figure S2.7. Solution-state ^{13}C NMR spectrum of unlabeled cyclohexane in 2-propanol with DMSO-d_6 capillary insert, acquired at 125 MHz (recycle delay: 10 s, 16 scans).

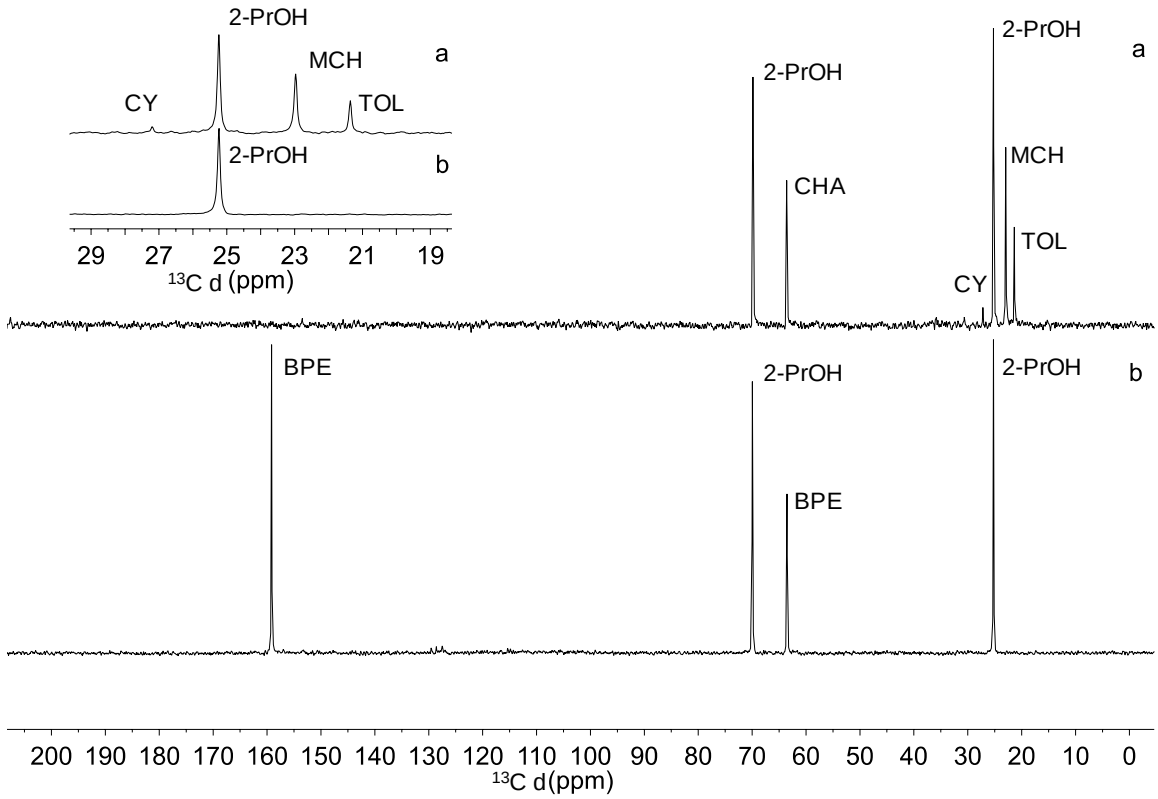

Figure S2.8. ^{13}C MAS-NMR spectra of ^{13}C-labeled BPE (2.0 mg, 0.011 mmol) in 2-PrOH (40 μL, 0.52 mmol) with 121 bar H_2 (0.48 mmol) over Ni/γ-Al_2O_3 (10.0 mg), recorded at 25 °C: (a) after reaction at 251 °C for 3 h in a 5 mm *WHiMS* rotor, and (b) before the reaction. Spectra were collected by averaging 16 scans, with an acquisition time of 0.3 s and a relaxation delay of 60 s. Line broadening of 10 Hz was applied during processing. Abbreviations: 2-Propanol (2-PrOH), benzyl phenyl ether (BPE), cyclohexane (CY), cyclohexanol (CHA), methylcyclohexane (MCH), toluene (TOL).

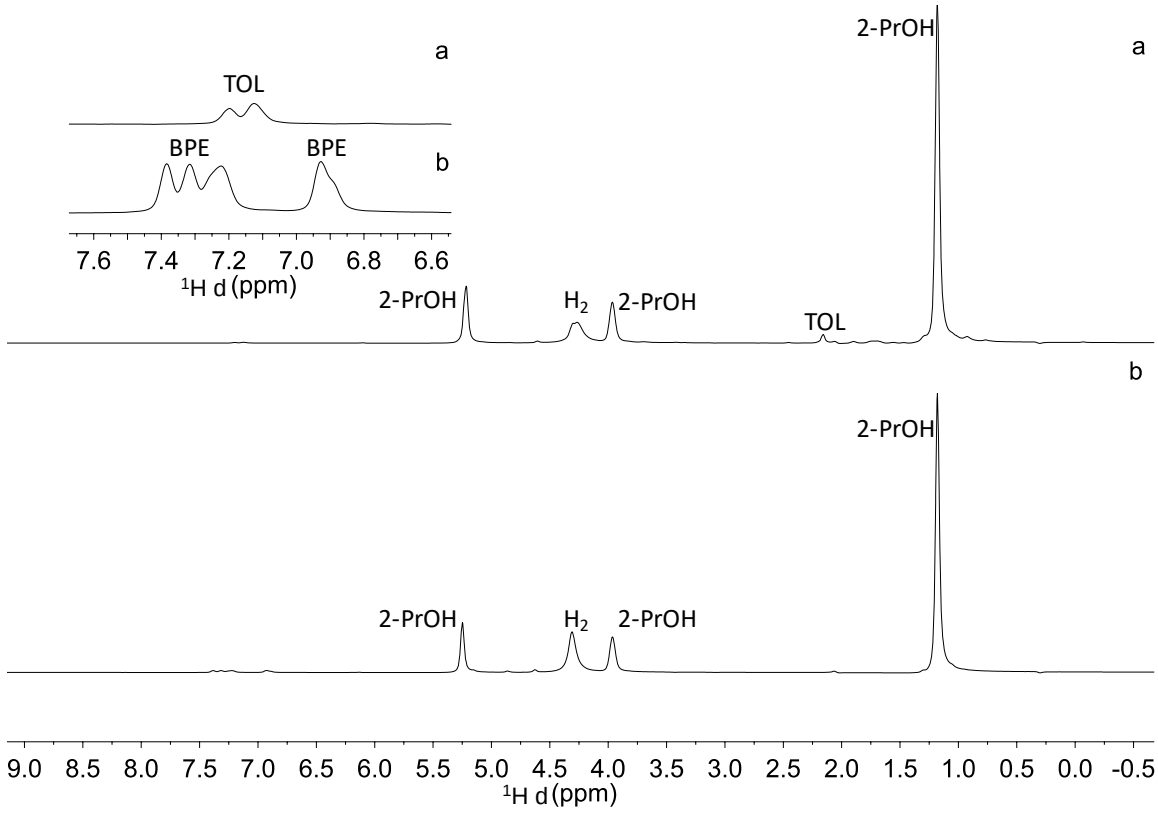

Figure S2.9. ^{1}H MAS-NMR spectra of ^{13}C-labeled BPE (2.0 mg, 0.011 mmol) in 2-PrOH (40 μL, 0.52 mmol) with 121 bar H_2 (0.48 mmol) over Ni/γ-Al_2O_3 (10.0 mg), recorded at 25 °C: (a) after reaction at 251 °C for 3 h in a 5 mm *WHiMS* rotor, and (b) before the reaction. Spectra were collected by averaging 32 scans, with an acquisition time of 1 s and a relaxation delay of 5 s. Line broadening of 10 Hz was applied during processing. Abbreviations: 2-Propanol (2-PrOH), benzyl phenyl ether (BPE), hydrogen (H_2), toluene (TOL).

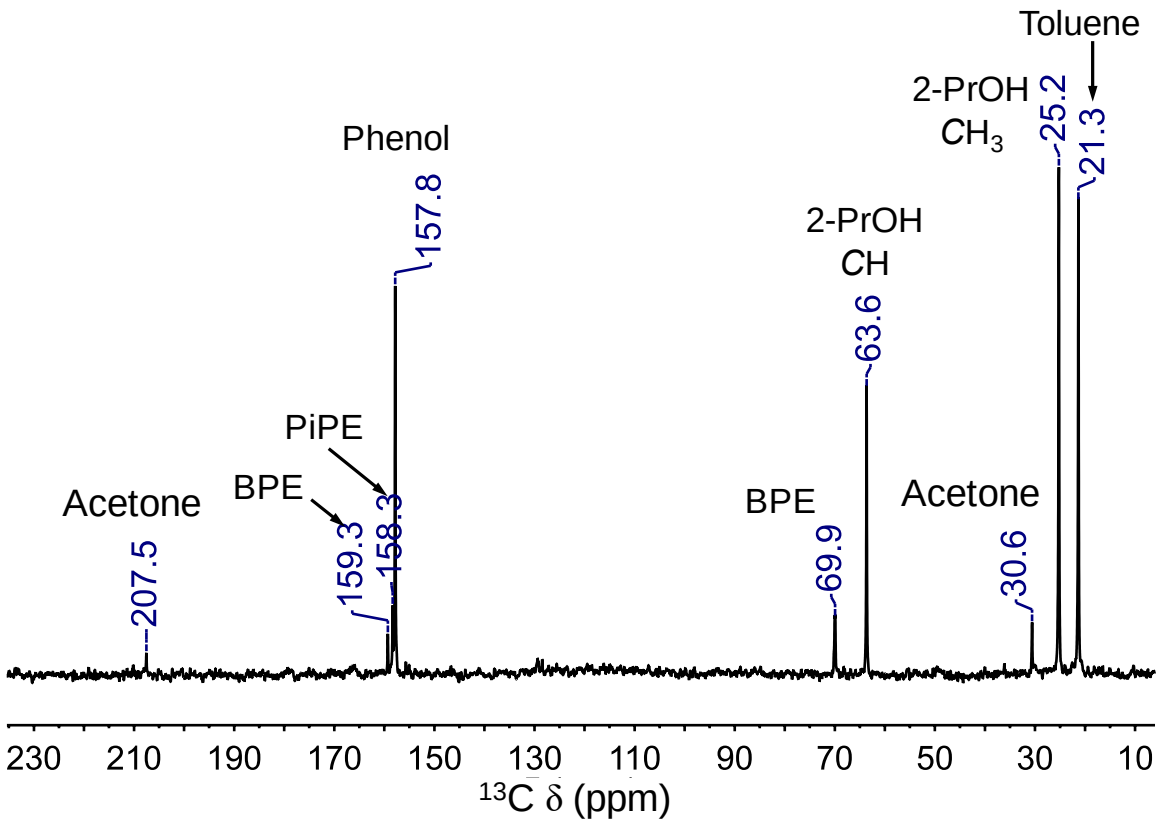

Figure S2.10. Solution-state ^{13}C NMR spectrum recorded after the reaction of the hydrogenolysis of BPE at 225 °C without added hydrogen, emphasizing the formation of acetone.

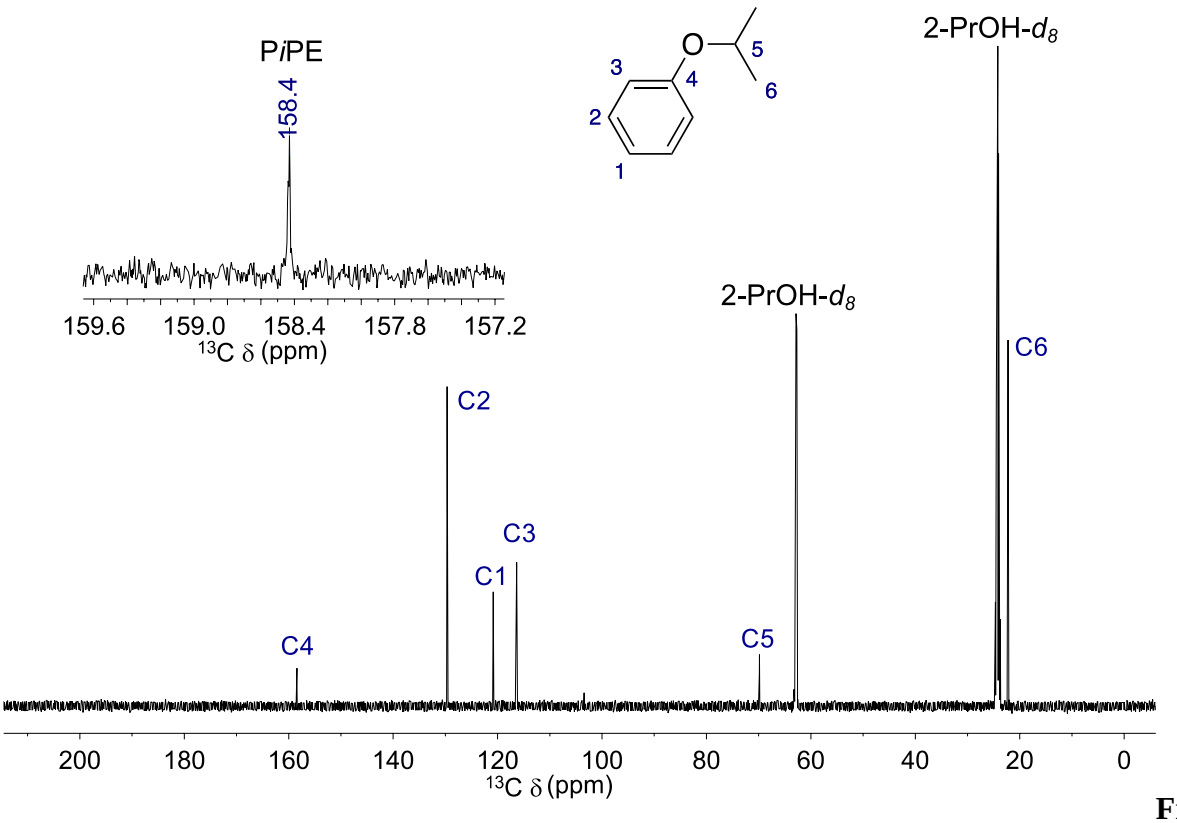

Figure S2.11. Solution-state ^{13}C NMR spectrum of phenyl isopropyl ether (P*i*PE) in 2-propanol-d_8, acquired at 125 MHz (recycle delay: 5 s, 128 scans) highlighting the C4 peak position of P*i*PE in the inset.

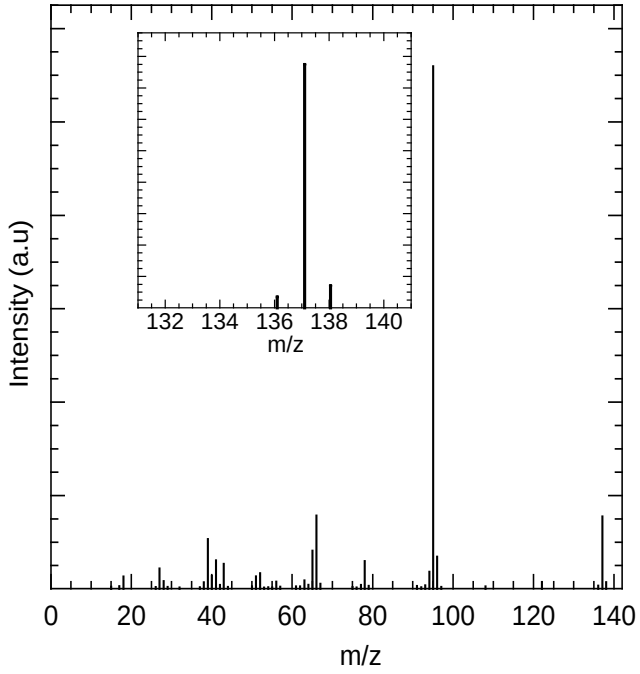

Figure S2.12. Mass spectrum of P*i*PE from gas chromatogram of the post-reaction mixture shown in **Figure 5**. The inset shows the molecular ion (m/z = 137) of P*i*PE ^{13}C-labeled at the phenolate position.

2.7.1 Additional References

(1) Jung, H. B.; Carroll, K.; Kabilan, S.; Heldebrant, D. J.; Hoyt, D.; Zhong, L.; Varga, T.; Stephens, S.; Adams, L.; Bonneville, A. Stimuli-Responsive/Rheoreversible Hydraulic Fracturing Fluids as a Greener Alternative to Support Geothermal and Fossil Energy Production. *Green Chem.* **2015**, *17*, 2799-2812.

(2) This paper.

(3) Qi, L.; Alamillo, R.; Elliott, W. A.; Andersen, A.; Hoyt, D. W.; Walter, E. D.; Han, K. S.; Washton, N. M.; Rioux, R. M.; Dumesic, J. A.; Scott, S. L. Operando Solid-State NMR Observation of Solvent-Mediated Adsorption-Reaction of Carbohydrates in Zeolites. *ACS Catal.* **2017**, 3489-3500.

(4) Bowers, G. M.; Schaef, H. T.; Loring, J. S.; Hoyt, D. W.; Burton, S. D.; Walter, E. D.; Kirkpatrick, R. J. Role of Cations in CO_2 Adsorption, Dynamics, and Hydration in Smectite Clays under in Situ Supercritical CO_2 Conditions. *J. Phys. Chem. C* **2017**, *121*, 577-592.

(5) Hoffman, R. E.; Becker, E. D. Temperature Dependence of the ^{1}H Chemical Shift of Tetramethylsilane in Chloroform, Methanol, and Dimethylsulfoxide. *J. Magn. Reson.* **2005**, *176*, 87-98.

(6) Bielecki, A.; Burum, D. P. Temperature dependence of ^{207}Pb MAS spectra of solid lead nitrate. An accurate, sensitive thermometer for variable-temperature MAS. *J. Magn. Reson., Ser A* **1995**, *116*, 215-220.

Chapter 3: Unraveling the Dynamic Network in the Reactions of an Alkyl Aryl Ether Catalyzed by Ni/γ–Al_2O_3 in 2-Propanol

3.1 Abstract

The reductive cleavage of aryl ether linkages is a key step in the disassembly of lignin to its monolignol components, where selectivity is determined by the kinetics of multiple parallel and consecutive liquid-phase reactions. Triphasic hydrogenolysis of ^{13}C-labeled benzyl phenyl ether (BPE, a model compound with the same C-O bond energy as the major β-O-4 linkage in lignin), catalyzed by Ni/γ-Al_2O_3, was observed directly at elevated temperatures (150 - 175 °C) and pressures (79-89 bar) using *operando* magic-angle spinning NMR spectroscopy. Liquid-vapor partitioning in the NMR rotor was quantified using the ^{13}C NMR resonances for the 2-propanol solvent, whose chemical shifts report on the internal reactor temperature. At 170 °C, BPE is converted to toluene and phenol with k_1 = 0.17 s^{-1} g_{cat}^{-1}, and an apparent activation barrier of (80 ± 8) kJ mol^{-1}. Subsequent phenol hydrogenation occurs much more slowly (k_2 = 0.0052 s^{-1} g_{cat}^{-1} at 170-175 °C), such that cyclohexanol formation is significant only at higher temperatures. Toluene is stable under these reaction conditions, but its methyl group undergoes facile H/D exchange (k_3 = 0.046 s^{-1} g_{cat}^{-1} at 175 °C). While the source of the reducing equivalents for both hydrogenolysis and hydrogenation is exclusively H_2/$D_{2(g)}$ rather than the alcohol solvent at these temperatures, the initial isotopic composition of adsorbed H/D on the catalyst surface is principally determined by the solvent isotopic composition (2-PrOH/D). All reactions are preceded by a pronounced induction period associated with catalyst activation. In air, Ni nanoparticles are passivated by a surface oxide monolayer, whose removal under H_2 proceeds with an apparent activation barrier of (72 ± 13) kJ mol^{-1}. The *operando* NMR spectra provide

molecularly-specific, time-resolved information about the multiple simultaneous and sequential processes as they occur at the solid-liquid interface.

3.2 Introduction

Liquid-phase reactions catalyzed by supported metals are important in the upgrading of low volatility chemical feedstocks, notably those obtained from renewable biomass. The presence of water, organic co-solvents, reactive solutes and spectator species, including ions, represent significant challenges for understanding and predicting reactions that occur at or near solid-liquid interfaces, especially when the conditions involve elevated temperatures and pressures.[1] For example, the reductive depolymerization of lignin which liberates aromatic monomers via hydrogenolysis of the aryl ether C-O linkages typically takes place in a triphasic solid-liquid-gas mixture at T > 100 °C and P > 10 bar.[2-6] Although computational studies can provide valuable guidance regarding the possible behaviors of various functional groups on well-defined metal surfaces,[7-12] they generally do not account for the complex reaction networks and realistic reaction conditions involved in the catalytic depolymerization of lignin. Most experimental studies have been conducted using compositional analysis of quenched reaction mixtures,[4] which often suffer from poor mass balance, and generate few kinetic or mechanistic insights.[13]

Since the C-O bond strength in benzyl phenyl ether (BPE) is predicted[14] to be comparable to that of the major β-O-4 aryl ether C-O linkages in lignin,[15] BPE has been widely used as a simple model for the biopolymer in studies of the kinetics and mechanism of C-O bond cleavage and subsequent reactions (although the presence of hydroxy and/or methoxy substituents may alter actual rates appreciably). Reaction occurs at the Ar-O bond for diaryl and simple alkyl aryl ethers, but switches to the Bn-O bond for aryl benzyl ethers

such as BPE,[16-18] as well as in in lignin itself. The hydrogenolysis of simple ethers and lignin ether bonds is catalyzed by a variety of soluble and solid phase catalysts.[19] In this work, we investigated Ni-catalyzed BPE hydrogenolysis via *operando* NMR experiments performed at elevated temperatures/pressures in magic-angle spinning (MAS) rotors capable of acquiring high-resolution spectra for three-phase mixtures (solid, liquid, and gas). The expected reactions are hydrogenolysis and competing aromatic hydrogenation, Scheme 3.1.

Highly dispersed Cu or Pd catalysts are well-established for use in hydrogenolysis reactions,[20-21] but Ni-based catalysts have emerged recently as interesting substitutes. Ni is more Earth-abundant than Pd, and it activates H_2 more readily than Cu.[22-25] However, unlike Pd and Cu, Ni nanoparticles more readily undergo surface oxidation, which results in their passivation upon exposure to air.[26-28] When a Ni catalyst is activated *in situ*, the need to remove overlayers on the catalyst surface, catalyst restructuring, and/or the formation of active sites can lead to substantial induction periods.[29-31]

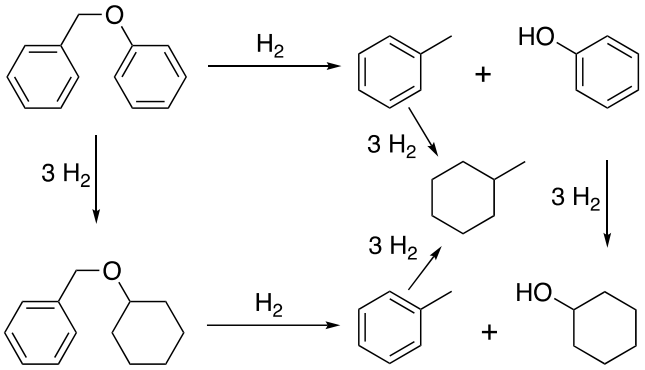

Scheme 3.1. Possible reactions in benzyl phenyl ether (BPE) hydrogenolysis to toluene and phenol, with competing aromatic hydrogenation.

Unfortunately, kinetic and mechanistic information inferred from yields measured at extended times convolute the rate of activation with the kinetics of subsequent catalytic reactions. In this study, high-quality *operando* NMR data combined with isotopic labeling

provide details on the kinetics and mechanism of Ni/γ-Al_2O_3 activation, the length of the induction period and the nature of its termination, the activity of the catalyst towards each of the organic components in solution as a function of the extent of reaction, the participation of the solvent, and the dynamic network of H/D exchange reactions that accompany catalytic ether hydrogenolysis.

3.3 Results and discussion

3.3.1 Design of the *Operando* NMR Study

Recently, we demonstrated the use of sealed MAS NMR rotors in reactions conducted in near-supercritical 2-PrOH (225 °C, P = 200 bar).[32-33] At room temperature, the ^{13}C MAS-NMR spectrum of 2-PrOH consists of two singlets at δ 25.3 (methyl) and 63.6 (methine) ppm, Figure 3.1. As the temperature of the sealed NMR rotor approaches 150 °C, the methyl and methine resonances shift to lower and higher frequencies, respectively, while two new resonances emerge at δ 23.2 and 63.1 ppm. The intensities of the latter increase with temperature, at the expense of the original 2-PrOH resonances. The positions of the new resonances also shift gradually to higher frequencies as the temperature rises.

The position of the new resonances is not consistent with a chemical reaction (e.g., the condensation of 2-PrOH to form diisopropyl ether). Furthermore, their appearance is readily reversible: when the rotor is cooled to room temperature, the intensities decrease and the resonances vanish. On this basis, we assign the new resonances to 2-PrOH vapor. Their intensities are consistent with the saturation vapor pressure of 2-PrOH (e.g., at 150 °C, the solvent is 5.5 % vaporized, corresponding to a pressure of ca. 10 bar, compared to the saturation vapor pressure of 9 bar at this temperature). The lower frequencies of both vapor-phase resonances relative to the corresponding liquid-phase resonances are consistent with

reduced intermolecular interactions, such as H-bonding, which are generally deshielding.[34] Three of the four 2-PrOH resonances shift linearly with temperature, Figure S3.1. The chemical shift of the methine resonance of liquid 2-PrOH is an exception, exhibiting slightly non-monotonic behavior.

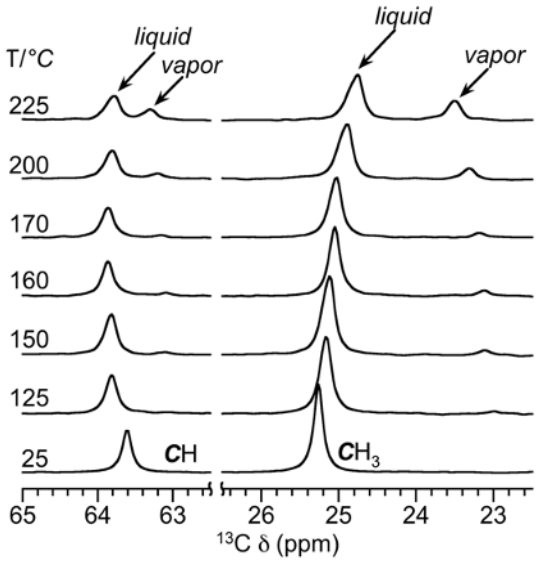

Figure 3.1. Variable temperature direct polarization ^{13}C MAS-NMR spectra of 2-PrOH, recorded in a sealed rotor, and showing distinct resonances for liquid and vapor phase species. The 5-mm o.d. NMR rotor (internal volume 140 μL) was charged with 40 μL 2-PrOH and 50 bar H_2 at room temperature. The estimated total internal pressure, including the saturated vapor pressure of 2-PrOH, rises from 71 bar at 125 °C to 118 bar at 225 °C. Each spectrum represents 32 scans with a recycle delay of 60 s and line broadening of 15 Hz. MAS rate: 5 kHz.

Usually, the temperature in solid-state NMR experiments must be estimated using an external thermal reference, such as $^{207}Pb(NO_3)_2$.[35-36] Here, direct observation of temperature-dependent chemical shifts for the solvent, and its vapor-liquid equilibrium, allow us to measure the internal temperature of the NMR rotor and to assess its thermal stability during

operando experiments. Using the intensity ratios of 2-PrOH liquid and vapor phase resonances, we estimate the time required for the internal rotor temperature to stabilize after the probe temperature reaches 150 °C to be ≤14 min. During this time, the rotor temperature rises *ca.* 5 °C, as judged by the 0.02 ppm change in chemical shift for the methyl resonance of 2-PrOH. Subsequent thermal drift, which would change the liquid:vapor ratio, was not detected. The integrity of the rotor seals is also readily assessed. A leak would cause the area of the liquid resonance to decrease continuously, while the area of the corresponding vapor resonance would grow initially as the liquid volume shrinks. The constant combined areas of liquid and vapor peaks in the spectra in Figure 3.1 confirm that the NMR rotor lost no material during the course of the experiment. The spectra are unchanged in the presence of $H_{2(g)}$.

Partial solvent vaporization causes the liquid-phase concentrations of non-volatile components in the NMR rotor to vary significantly with temperature. The extent of vaporization is readily quantified by integration of the internal solvent resonances. In the experiment shown in Figure 3.1, (6.1 ± 0.8) % of the 2-PrOH was present in the vapor phase at 150 °C, rising to (30.1 ± 1.5) % at 225 °C. Taking both solvent vaporization and liquid expansion into account, a dissolved solute will experience an increase in concentration of 6.5 % at 150 °C, and 43 % at 225 °C, relative to its initial concentration at room temperature. These concentration changes have significant implications for non-first-order reaction kinetics.

3.3.2 Catalytic Hydrogenolysis of Benzyl Phenyl Ether (BPE)

To enhance sensitivity in the NMR experiments, BPE was selectively ^{13}C-labeled as shown in Scheme 3.2. In 2-PrOH at room temperature, the ^{13}C MAS-NMR spectrum

consists of two singlets at δ 70.1 and 159.3 ppm, corresponding to the methylene and phenolate-C1 carbons, respectively. The appearance of the spectrum was unchanged in the presence of either γ-Al_2O_3 or Ni/γ-Al_2O_3 (2 wt% Ni), Figure S3.2, therefore the presence of superparamagnetic[37] Ni nanoparticles does not impede the detection of organic molecules in the solution phase. The concentrations of species adsorbed on the catalyst surface are presumably below the detection limit.

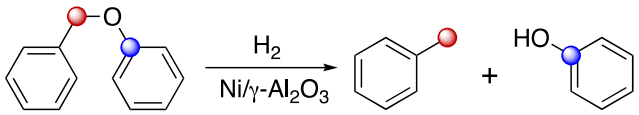

Scheme 3.2. Benzyl phenyl ether (BPE, selectively ^{13}C-labeled at the benzylic (red, BPE-B) and phenolate-C_1 (blue, BPE-P) positions. Hydrogenolysis results in toluene-α-^{13}C and phenol-1-^{13}C.

After standing for 3 d at 25 °C under 50 bar H_2, there were no changes in the ^{13}C MAS-NMR spectrum. However, when the rotor was heated to 150 °C, a reaction was detected within the first hour. A typical array of NMR spectra is shown in Figure 3.2. The two BPE ^{13}C resonances began to disappear after an initial induction period. The onset of BPE conversion coincides with the appearance of phenol-1-^{13}C and toluene-α-^{13}C resonances, which appear as singlets at δ 157.8 and 20.8 ppm, respectively. At the end of the reaction, the selectivities for both products exceeds 95 %. These values include the contribution at δ 18.3 ppm for toluene vapor (which disappeared when the rotor was cooled to room temperature). No vapor phase peaks for BPE or phenol were detected at any of the temperatures in this study, due to their lower volatilities. Since no benzene was detected (ca. 128.4 ppm), hydrogenolytic cleavage of BPE occurs selectively at the Bn-O bond, as expected owing to its lower bond dissociation energy relative to the Ph-O bond.[38-39]

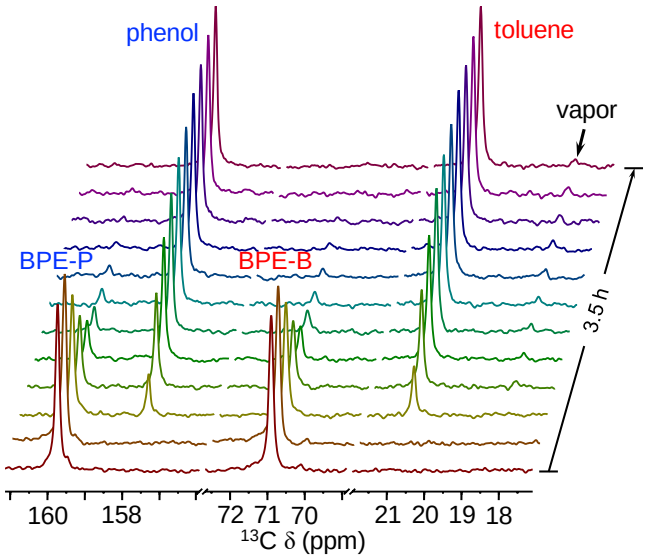

Figure 3.2. *Operando* array of direct polarization ^{13}C MAS-NMR spectra recorded during BPE hydrogenolysis at 150 °C, showing conversion of BPE to toluene-α-^{13}C and phenol-$^{13}C_1$. The ^{13}C-labeled positions of BPE are indicated as BPE-B (benzylic) and BPE-P (phenolate-C_1). The rotor was initially loaded with 2 wt% Ni/γ-Al_2O_3 (10 mg, air exposed), BPE (2.0 mg, 0.011 mmol), and 2-PrOH (40 μL, 0.52 mmol), and pressurized with 50 bar H_2 (0.20 mmol) at room temperature (giving a H_2 pressure of 70 bar and 2-PrOH pressure of 9 bar, for a total pressure of 79 bar at 150 °C). MAS rate: 5 kHz.

No hydrogenation of either BPE or toluene was observed, although some hydrogenation of toluene was seen previously at a higher temperature and pressure (225 °C, 120 bar H_2).[32] However, phenol is more reactive,[13] and it was partially hydrogenated to cyclohexanol (ca. 3 % conversion in 10 h at 150 °C, Figure S3.3).

3.3.3 Kinetics of BPE Hydrogenolysis

Kinetic profiles extracted from time-resolved *operando* ^{13}C MAS-NMR spectra are shown in Figure 3.3. The extended induction period is attributed to catalyst activation,

which lasts slightly longer than the thermal equilibration period of the NMR rotor (≤ 14 min at 150 °C). This temporal separation between catalyst activation and BPE conversion is fortuitous, since it ensures the collection of isothermal kinetic data during the hydrogenolysis reaction. Reaction profiles were truncated to eliminate measurements made during the induction period prior to kinetic analysis (however, we note that this approach is not justified when there is significant temporal overlap of the kinetic phases). The remaining data were analyzed with a first-order rate equation, to give the curvefits shown in Figure 3.3. All four pseudo-first-order rate constants ($k_{1,obs}$) extracted from data for each of the four observed ^{13}C resonances (i.e., BPE-B, BPE-P, toluene-C□, and phenol-1-C) are very similar, with an average value of (0.56 ± 0.04) x 10^{-3} s^{-1} at 150 °C (Table 3.1).

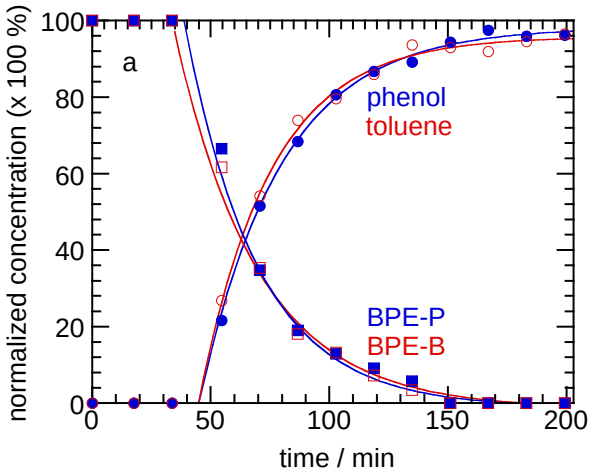

Figure 3.3. Kinetic profiles for BPE hydrogenolysis to toluene and phenol, in a rotor loaded with air-exposed 2 wt% Ni/γ-Al_2O_3 in 2-PrOH and 50 bar H_2 (giving a total pressure of 79 bar at 150 °C), based on resonance intensities normalized to the initial BPE concentration, for the two BPE resonances (squares) and its two primary hydrogenolysis products (circles). Data recording started when the NMR probe reached 150 °C. The curvefits (solid lines) were obtained by fitting the first-order rate equation to the portion of the data remaining after removal of measurements made during the initial induction period.

Table 3.1. Temperature-dependence of pseudo-first-order rate constants and kinetic isotope effects for BPE hydrogenolysis catalyzed by Ni/γ-Al_2O_3 in 2-propanol

Exp	T °C	Catalyst mass mg	Solvent [a]	Gas	D/(H+D) [b] %	$10^3 k_{1,obs}$ (s^{-1}) [c] BPE-B	BPE-P	BPE (avg)	Toluene	Phenol	Phenol+Cyclo-hexanol
1	150	9.8	2-PrOH	H_2	0	0.59(2)	0.60(3)	0.60(2)	0.54(2)	0.50(2)	n.a.
2	160	10.0	2-PrOH	H_2	0	1.16(15)	1.17(12)	1.16(14)	0.91(10)	1.12(51)	n.a.
3	170	10.1	2-PrOH	H_2	0	1.63(8)	1.70(10)	1.66(8)	1.37(21)	1.10(14)	n.a.
4	175	10.1	2-PrOD	D_2	100	1.51(14)	1.28(16)	1.38(15)	1.43(14)	1.00(7) [d]	1.55(18)
5	175	10.0	2-PrOH	D_2	43	1.82(13)	1.73(16)	1.78(14)	1.62(17)	1.18(10) [d]	1.49(11)
6	175	10.1	2-PrOD	H_2	57	1.10(6)	0.95(5)	1.03(5)	0.96(7)	0.61(4) [d]	0.79(8)

[a] 2-PrOH is $(CH_3)_2CHOH$; 2-PrOD is $(CD_3)_2CDOD$. [b] Fractional abundance (%) of exchangeable H/D atoms, contributed by H_2/D_2 (two atoms per molecule) and 2-PrOH/D (one atom per molecule). [c] Except where noted, all rate constants were obtained from non-linear least-squares fits of the first-order rate equation to concentration profiles obtained in *operando* MAS-NMR experiments, after data truncation to remove the induction period. Values in parentheses represent non-linear least-squares curvefit errors. [d] Obtained from a non-linear least-squares fit of a biexponential rate equation[44] to the concentration profile, to account for sequential ether hydrogenolysis and hydrogenation of phenol to cyclohexanol. n.a. = not applicable (because the yield of cyclohexanol was negligible).

The dependence of k_{obs} on $P(H_2)$ is weak, as shown by kinetic profiles recorded in rotors charged with initial H_2 pressures of $50 \leq P(H_2) \leq 125$ bar (Figure S3.4), consistent with previous work.[40] In the ^1H MAS-NMR spectrum, $H_{2(g)}$ appears as a singlet at δ 4.2 ppm while dissolved H_2 is a singlet at δ 4.6 ppm,[41-42] Figure S3.5. Since it was initially present in

ca. 20-fold excess relative to BPE, the change in H_2 concentration over the course of the reaction is small. Indeed, the intensities of the 4.2 and 4.6 ppm resonances, measured at 25 °C before and after reaction, decreased negligibly. Temperature effects on H_2 solubility are reported to be weak in the temperature range of interest.[43] However, the concentration of dissolved H_2 increased slightly, from 0.35 M at 150 °C to 0.47 M at 170 °C, due to the increase in pressure.

To ensure that environmental conditions specific to the NMR rotor (such as magic-angle spinning) do not influence the kinetics, and that mass transport limitations do not affect the rate, the reaction was also conducted in a 25 mL batch reactor at 150 °C using the same BPE concentration, catalyst:BPE ratio, solvent, and $P(H_2)$. The reaction progress was monitored by *ex situ* GC analysis of liquid aliquots removed at timed intervals. A short induction period (ca. 10 min) was observed when air-exposed Ni/γ-Al_2O_3 (2 wt%) was used as the catalyst, Figure S3.6. Both BPE conversion and toluene formation are pseudo-first-order. Despite the lower time resolution of the batch reactor experiment, the observed rate constants are comparable to those obtained by the *operando* NMR method.

Similar NMR experiments conducted at 160 and 170 °C are shown in Figure 3.4a. Because $k_{1,obs}$ does not depend on the concentration of BPE (the limiting reagent), the pseudo-first-order rate constants are not affected by temperature-dependent changes in the extent of solvent vaporization. At the highest reaction temperature, the rate of phenol formation is slower than that of toluene (Table 3.1). However, this effect disappears when the combined rate of formation of phenol and cyclohexanol is analyzed.

Pseudo-first-order rate constants were normalized by dividing the average k_{obs} value measured for BPE conversion (i.e., the mean of values obtained using the data from the BPE-B and BPE-P resonances) by the catalyst mass, and the normalized rate constants were

used to construct the Arrhenius plot in Figure 3.4b. The apparent activation energy (including adsorption/desorption energies and intrinsic reaction barriers) for BPE hydrogenolysis in 2-PrOH is (80 ± 8) kJ mol^{-1}. This value is essentially the same as a previous report, 72 kJ mol^{-1} (no error reported), for the same reaction catalyzed by silica-supported Ni nanoparticles suspended in water.[40] It is a small but significant fraction of the calculated Bn-O bond dissociation energy (236 kJ mol^{-1}),[14] which DFT calculations suggest is the rate-determining step.[45]

3.3.4 H/D Isotopic Exchange during Aryl Ether Hydrogenolysis

The small volume of the solid-state NMR rotor facilitates the use of isotopically-labeled gases and solvents in mechanistic studies. When the reaction of BPE was conducted with D_2 in 2-PrOH at 175 °C, a new ^{13}C NMR resonance at δ 63.8 ppm (assigned to a methine resonance of 2-PrOH) was detected near the end of the induction period, just before the appearance of toluene (Figure 3.S7). Initially, it emerged as a low frequency shoulder on the original solvent methine resonance (δ 64.0 ppm), then grew in at the expense of that peak. H/D exchange in the methine group of 2-PrOH can be ruled out, since such exchange would give rise to a 1:1:1 triplet characteristic of C-D coupling. This result also shows that solvent is not serving as a significant source of H_2 under the reaction conditions, since its dehydrogenation-rehydrogenation would result in such isotopic exchange at the methine C-H bond, Scheme 3.3a. Furthermore, the spectra show no evidence for H/D exchange in the CH_3 groups of 2-propanol (as would be expected from alcohol dehydration-rehydration), Scheme 3.3b. Aluminas are known to catalyze 2-propanol dehydration in the gas phase, but at higher temperatures (> 200 °C).[46] A blank experiment conducted at 175 °C with BPE in the presence of 2-PrOH and the alumina support (i.e., no Ni or H_2). After 12 h, there was no

conversion of BPE, and no ^{13}C NMR peaks for either diisopropyl ether (dehydration product) or acetone (dehydration product).

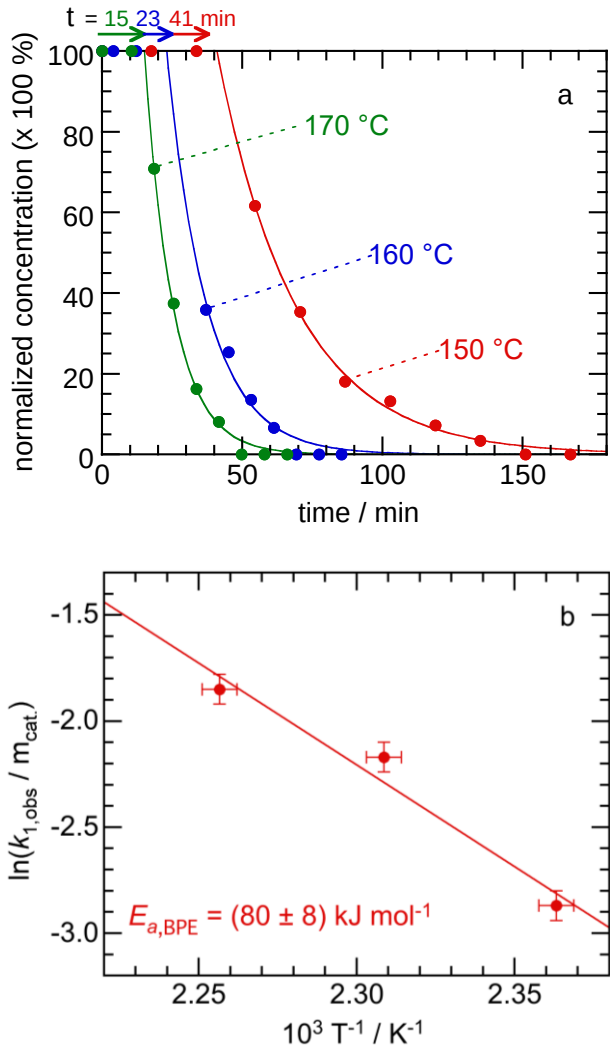

Figure 3.4. (a) Variable temperature reaction profiles for hydrogenolysis of BPE (2.0 mg, 0.011 mmol) in 2-PrOH (40 μL, 0.52 mmol) with 50 bar H_2 (0.20 mmol) catalyzed by Ni/γ-Al_2O_3 (2 wt% Ni, ca. 10 mg, air-exposed). Total internal pressures at 150-170 °C were estimated to be 79-86 bar. Curvefits (lines) were obtained using a first-order rate law, after truncation to remove data recorded during the induction period (see Table 3.1 for rate constants). The length of the induction period (τ) was estimated by extrapolating the first-order kinetic curvefit to 0 % conversion. (b) Arrhenius plot of pseudo-first-order rate constants for BPE hydrogenolysis (normalized by catalyst mass; the uncertainty reflects full error propagation in the Arrhenius equation,[47] not the error in the linear fit parameters).

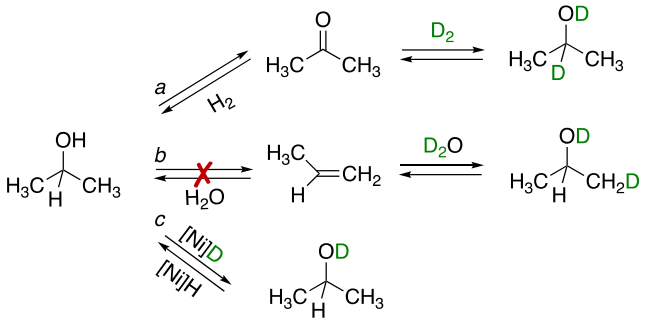

Scheme 3.3. Three possible routes for H/D exchange in 2-PrOH, catalyzed by Ni/γ-Al_2O_3. Only route (c) was detected experimentally for temperatures ≤ 175 °C.

Definitive assignment of the new ^{13}C NMR resonance at 63.8 ppm to $(CH_3)_2CHO\boldsymbol{D}$ was achieved by comparison to the solution-state ^{13}C NMR spectrum of an equimolar mixture of $(CH_3)_2CHO\boldsymbol{D}$ and $(CH_3)_2CHO\boldsymbol{H}$, Figure S3.8. The methine ^{13}C chemical shifts of these isotopologs differ by only 15.2 Hz, mostly likely due to slight differences in intermolecular interactions. The difference in the methyl ^{13}C chemical shifts caused by OH/OD exchange is even smaller (6.8 Hz), and is not visible in the MAS-NMR spectra.

Thus 2-PrOH undergoes slow exchange with D_2 *only* at its hydroxyl group, Scheme 3.3c. A kinetic profile for this reaction, catalyzed by Ni/γ-Al_2O_3, is shown in Figure S3.9. The pronounced induction period (40 min at 175 °C) suggests that exchange is catalyzed by the activated (i.e., reduced) form of the catalyst (*vide infra*). The final conversion to $(CH_3)_2CHO\boldsymbol{D}$, 44 %, is essentially the same as the initial fraction of exchangeable deuterium D/(D+H), 43 %, present in the 2-PrO<u>H</u>/<u>D_2</u> mixture.

The effect of isotopic substitution in either the solvent or the gas (H_2/D_2) on the rate of the principal reaction, BPE cleavage, is minor, Table 3.1. The apparent kinetic isotope effect (KIE), $k_{1,H}/k_{1,D}$ = (1.3 ± 0.2), is the ratio of the average rate constants obtained using the two BPE signals in Expts 3 and 4 (note that the reaction temperatures are slightly different, but

the higher temperature in Expt 4 with D_2 will attenuate, not enhance, the rate difference). A small (i.e., secondary) KIE value is consistent with rate-determining C-O bond cleavage.

3.3.5 Phenol Hydrogenation

Formation of cyclohexanol becomes significant only at $T \geq 170$ °C, as shown by the appearance of a singlet at δ 69.7 ppm for cyclohexanol-1-^{13}C. In principle, cyclohexanol could be formed via partial hydrogenation of BPE to give benzyl cyclohexyl ether followed by C-O bond cleavage, or directly by phenol hydrogenation (Scheme 3.1). However, no ^{13}C NMR signals were detected for benzyl cyclohexyl ether. Furthermore, the rate of disappearance of the BPE-P signal is the same as that of the BPE-B signal (Table 3.1). Consequently, we can confidently infer that cyclohexanol is formed via phenol hydrogenation.

Cyclohexanol can undergo reversible acid-catalyzed dehydration to cyclohexene, which would cause the ^{13}C label to be distributed over all six cyclohexanol carbons.[48] This scrambling would reduce the intensity of the cyclohexanol-1-^{13}C resonance over time, and lead to the appearance of several new cyclohexanol resonances (□ 34.7, 25.1, and 23.7 ppm).[48] Since this effect was not observed, cyclohexanol dehydration (as well as 2-PrOH dehydration) is not significant under the reaction conditions. We can also rule out rapid hydrogenation of cyclohexene to cyclohexane, since the latter was not detected either, although cyclohexane was observed in our previous study conducted at a higher reaction temperature.[32]

The kinetic profile for phenol shown in Figure 3.5 has the typical biexponential shape of a reaction intermediate. The curve was analyzed using two pseudo-first-order rate constants. Kinetic ambiguity precludes *a priori* assignment of the rate constants.[44] However, the larger

value is similar to the $k_{1,obs}$ value obtained from single exponential fit to the BPE profiles (Table 3.1), and is therefore attributed to BPE hydrogenolysis. We attribute the smaller of the two values, $k_{2,obs}$ = (5.2 ± 0.4) x 10^{-5} s^{-1}, to phenol hydrogenation. This value corresponds to k_2 = (5.2 ± 0.4) x 10^{-3} s^{-1} g_{cat}^{-1} at 175 °C, making phenol conversion to cyclohexanol ca. 30x slower than C-O bond cleavage under the reaction conditions.

When BPE hydrogenolysis was conducted in the presence of readily-exchangeable deuterium (present either in the solvent, as 2-PrOD, or in the gas, as D_2), a new cyclohexanol resonance appeared adjacent to the singlet at δ 69.7 ppm (Figure S3.10). The signal, at δ 69.2 ppm (*t*, 1:1:1, $^1J_{C\text{-}D}$ = 21.5 Hz), reflects H/D exchange at the C_1 position, Scheme 3.4. Presumably, D is also incorporated at other ring positions during phenol hydrogenation, but the effect is not detectable because the other ring carbons do not become ^{13}C-labeled. The hydroxyl protons of both phenol and cyclohexanol are also expected to undergo rapid H/D exchange in the presence of exchangeable deuterium.

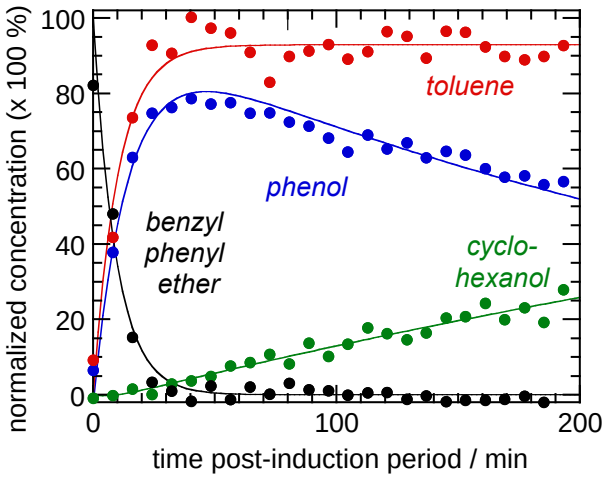

Figure 3.5. Kinetic analysis of individual ^{13}C NMR profiles recorded during BPE conversion in a rotor loaded with air-exposed Ni/γ-Al_2O_3 (2 wt%) and 50 bar D_2 in 2-PrOH, after heating to 175 °C (resulting in a total pressure of 89 bar). Data collected during the induction period were removed prior to non-linear least-squares curvefitting. The BPE and toluene profiles were analyzed with a single exponential rate equation; the phenol and cyclohexanol profiles were analyzed with a biexponential rate equation.

When BPE cleavage was performed in 2-PrOH in the presence of D_2, no KIE for phenol ring saturation was observed. However, conducting the reaction in 2-PrOD in the presence of H_2 resulted in an inverse kinetic isotope effect of $k_{2,H}/k_{2,D}$ = (0.66 ± 0.14). In these experiments, the total amounts of exchangeable D contributed by the gas and the solvent were comparable. Inverse KIEs of 0.5 - 0.8 have been reported for ring saturation of benzene and simple alkylaromatics, where they arise due to the sp^2-to-sp^3 rehybridization of ring carbons.[49-52] Comparing the reaction rates in either 2-PrOH with $D_{2(g)}$, or in 2-PrOD with $H_{2(g)}$, revealed that the kinetics of phenol saturation is influenced primarily by the isotopic composition of the solvent. The solvent kinetic isotope effect is unexpected, considering that the experiments described above showed the reducing agent to be

exclusively $H_2/D_{2(g)}$, not 2-propanol. It suggests that the catalyst activates only a small fraction of the available $H_2/D_{2(g)}$ at a given time, and that exchange between adsorbed H/D and $H_2/D_{2(g)}$ is slow relative to exchange between adsorbed atomic H/D and 2-PrOH/D.

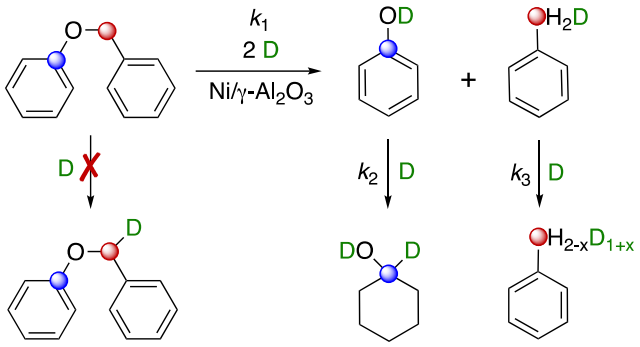

Scheme 3.4. Deuterium incorporation into ^{13}C-labeled BPE and its reaction products, in the presence of D_2 and/or 2-PrOD.

The H/D exchange reaction on the surface of the catalyst is shown in eq 3.1, where H*/D* represents the adsorbed H/D.

$$H^* + \text{2-PrOD} \leftrightarrows D^* + \text{2-PrOH} \qquad (3.1)$$

From the Ni(0) dispersion, we estimate the maximum amount of adsorbed H/D to be ca. 0.06 %, relative to the exchangeable H/D initially present as H_2/D_2 in the rotor. In the early stages of phenol hydrogenation, the isotopic composition of adsorbed H/D will therefore be determined principally by the isotopic composition of the solvent (2-PrOH/D), assuming that exchange is fast between adsorbed H/D and the solvent. Based on the conversion of 2-PrOH to 2-PrOD in the presence of D_2, measured by observing the formation of the new ^{13}C resonance for 2-PrOD at 63.8 ppm, the exchange rate constant was estimated to be (0.044 ± 0.008) s^{-1} g_{cat}^{-1} at 175 °C (Figure S3.9). At longer reaction times, when extensive H/D exchange between gas and solvent has occurred, the effect on k_2 is minor, since phenol hydrogenation is already largely complete.

3.3.6 H/D Isotopic Exchange in Toluene.

No methylcyclohexane was detected in any experiment, although our previous study reported slow catalytic hydrogenation of toluene at a higher reaction temperature, 225 °C.[32] However, when BPE cleavage was conducted in 2-PrOD at 175 °C, the appearance of the expected singlet at 20.6 ppm for the toluene methyl group was accompanied by several new peaks at slightly lower frequencies, Figure 3.6a. The peaks show the characteristic ^{13}C-D coupling patterns of partially deuterated methyl groups, Figure 3.6b. The chemical shifts for each toluene isotopolog, extracted from these spectra, are shown in Table S3.3. D incorporation into toluene was also confirmed by MS analysis, Figure S3.11.

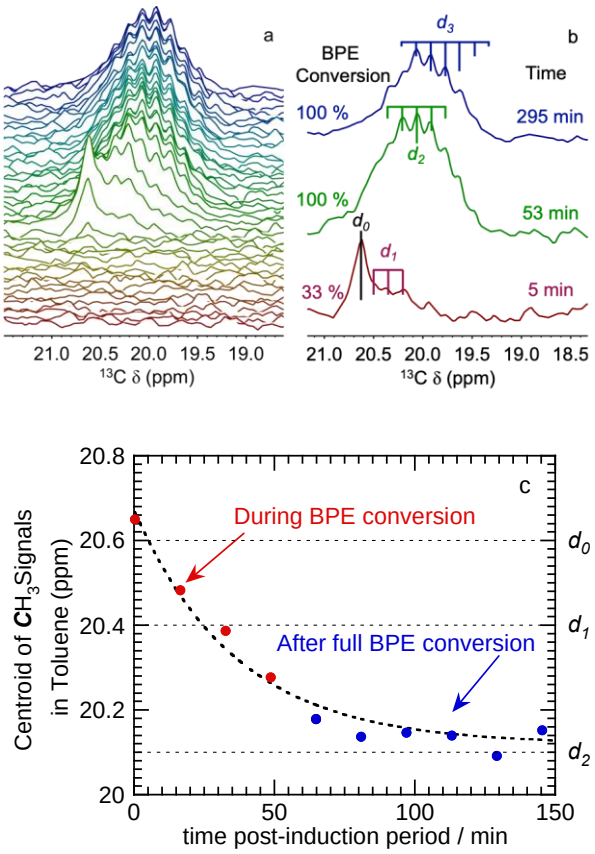

Figure 3.6. Formation of toluene-α-d_n during BPE hydrogenolysis in a rotor loaded with Ni/γ-Al_2O_3 (10.0 mg, 2 wt% Ni) in 2-PrOD and 50 bar H_2 and heated to 175 °C (resulting in a total pressure of 89 bar, and a ratio of exchangeable D/(H+D) = 0.57): (a) time-resolved

array of *operando* ^{13}C MAS-NMR spectra, showing the evolution of the $^{13}CH_{3-x}D_x$ resonances; (b) comparison of characteristic ^{13}C-^{2}H coupling patterns with ^{13}C resonances observed 5 min after the end of induction period (at 33 % BPE conversion), 48 min later (at 100 % BPE conversion), and at the end of the experiment; (c) time evolution of the centroid for the $^{13}CH_{3-x}D_x$ resonance (points), with a single exponential curvefit for H/D exchange (bold dashed line), and indicators for the chemical shifts for the various toluene methyl isotopologs (light dashed lines).

The first spectrum in Figure 3.6a was recorded shortly after the end of the induction period (when BPE conversion was just 33 %). It represents a mixture of toluene-α-d_0 and -d_1 (Figure 3.6b). H/D exchange in the BPE methylene group prior to C-O bond cleavage was not detected (Scheme 3.4). We infer that toluene-α-d_1 is a direct result of the reaction of adsorbed D with adsorbed benzyl-α-d_0 (formed by C-O bond cleavage of BPE), eq 3.2, rather than a product of H/D exchange in the benzylic position of BPE prior to aryl ether cleavage.

$$PhCH_2* + D* \leftrightarrows PhCH_2D + 2 * \quad (3.2)$$

Figure 3.6a shows that the number of peaks in the toluene methyl region changes over time, reflecting the increasing extent of methyl deuteration. After 53 min, the ^{13}C singlet for toluene-d_0 was no longer visible; the resonances correspond to a mixture of toluene-α-d_1, -d_2, and -d_3 (Figure 3.6b). The peaks in the methyl region continued to evolve after the maximum production of toluene was reached, ca. 100 min after the onset of BPE conversion (Figure 3.6b-c). This finding demonstrates that H/D exchange also occurs independent of C-O bond cleavage. Indeed, H/D exchange was observed when toluene-α-^{13}C itself was heated at 175 °C in 2-PrOH with 50 bar D_2 in the presence of Ni/γ-Al_2O_3, Figure S3.12. In that experiment, the final centroid location for the methyl resonances, 20.3 ppm, indicates a D

content of 44 at% (by linear interpolation of the chemical shifts for toluene-α-d_0 and -d_1). This composition matches the fraction of exchangeable D (43 at%).

After BPE conversion was complete, the final centroid location for the toluene methyl resonances (20.1 ppm) is close to the chemical shift of toluene-α-d_2, Figure 3.6c. The overall D content in the methyl group (63 at%, estimated by linear interpolation of the chemical shifts for toluene-α-d_1 and -d_2) resembles the fraction of exchangeable D (57 at%) in the reaction mixture (0.52 mmol 2-PrOD and 0.20 mmol H_2). The pseudo-first-order fit to the kinetic profile for the appearance of deuterated toluene from BPE in 2-PrOD under 50 bar H_2 yielded k_3 = (0.046 ± 0.006) s^{-1} g_{cat}^{-1} at 175 °C, Figure 3.6c. A slightly smaller value, k_3 = (.021 ± 0.006) s^{-1} g_{cat}^{-1}, was measured for the reaction of toluene in 2-PrOH with 50 bar D_2 (corresponding to a similar total exchangeable D fraction, 43 at%), Figure S3.12.

3.3.7 Catalyst Activation

A pronounced induction period is evident in the kinetic profile for BPE hydrogenolysis in Figure 3.3. Its duration (ca. 41 min at 150 °C, estimated by extrapolating a first-order curvefit of the post-induction period kinetic profile to 100 % conversion) was reproducible in duplicate runs at the same temperature. At 135 °C or below, the induction period was prohibitively long. Attempts to follow the reaction at such temperatures using the same reactant and catalyst loadings resulted in no discernable BPE conversion even after *ca.* 15 h. At 160 and 170 °C, the induction period was shortened to ca. 23 and 15 min, respectively, Figure 3.4a. These observations suggest that activation of the Ni/γ-Al_2O_3 catalyst is slow under the reaction conditions.

3.3.8 Origin of the Extended Induction Period

The observed induction period is consistent with the reported kinetics of H_2 reduction of Ni/NiO materials, including those involving oxide monolayers[53] and bilayers,[54] as well as core/shell[55] structures. For example, removal of the oxide shell in $MgAl_2O_4$-supported Ni/NiO core/shell nanoparticles (3.2 nm) was reported to occur in the range 140-180 °C.[56] The reaction starts at the outermost NiO-covered surface, and occurs without the formation of intermediate oxide phases.[57-58]

In this study, the only Ni-containing phase visible in the powder XRD pattern of the air-exposed catalyst is Ni(0), with a mean nanoparticle diameter of ca. 14 nm (Figure S3.13). Variable-temperature EPR spectra, recorded in air between -170 and 20 °C, are also consistent with Ni(0). At the lower temperatures, the EPR resonance is dramatically broadened and shifted to lower fields (Figure 3.7). This behavior is characteristic of superparamagnetic Ni(0) nanoparticles.[37] EPR spectra of the air-exposed catalyst were also recorded in flowing H_2. The spectrum acquired at 20 °C was unchanged, but the EPR signal intensity increased slightly when the temperature was ramped to 170 °C, held for 30 min, then returned to room temperature, Figure S3.14. This change is consistent with reduction of an EPR-silent[59] surface oxide layer, causing the amount of EPR-active Ni(0) to increase.

XPS measurements were performed with 10.5 wt% Ni/□-Al_2O_3 to increase sensitivity. They confirm the presence of a minor NiO component associated with the air-exposed Ni nanoparticles,[60] Figure S3.15 and Table S3.2. HAADF-STEM imaging with EDX suggests that the NiO is present as a surface layer (Figure S3.16). The presence of a surface oxide was further verified by temperature-programmed reduction (TPR) of an air-exposed sample (Figure S3.17). The H_2 consumption corresponds to reduction of ca. 6 % of total Ni, in

agreement with the H_2 consumption expected for reduction of an oxide monolayer (ca. 7%, Table S3.1).

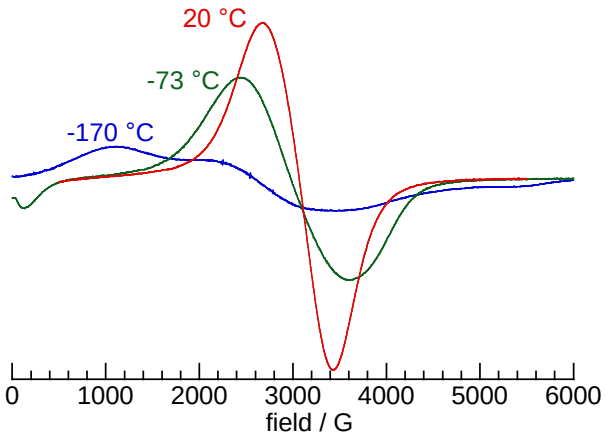

Figure 3.7. Variable-temperature EPR spectra of air-exposed Ni/γ-Al_2O_3 (2 wt% Ni, ca. 14 nm average diameter nanoparticles).

Unlike Ni(0), NiO is an ineffective catalyst for hydrogenation and hydrogenolysis.[61] In this study, the reaction temperatures (150-175 °C) are too low to cause reduction of NiO nanoparticles (> 200 °C),[62] but they are consistent with reduction of a superficial oxide formed on Ni(0) nanoparticles exposed to O_2 at room temperature.[26-28] The as-prepared Ni/γ-Al_2O_3 catalyst was typically stored in air at room temperature for several days prior to use. The barrier for catalyst activation was estimated from the reciprocal of the induction time, τ. The Arrhenius plot gives a barrier of (72 ± 13) kJ mol^{-1}, Figure 3.8. Although literature values for NiO reduction are highly dependent on the reaction conditions, kinetically-controlled values fall in the range 65-98 kJ mol^{-1}.[57]

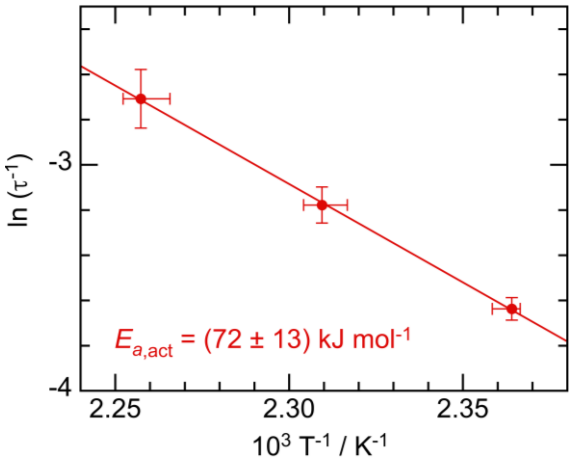

Figure 3.8. Arrhenius plot for the activation of air-exposed Ni/γ-Al_2O_3 by H_2 in 2-PrOH (red), based on the reciprocal of the duration of the induction period (τ) in BPE hydrogenolysis. The temperature error bars represent the thermal variability during the induction period, ca. 5 °C (estimated using 2-PrOH chemical shifts). The uncertainty in $E_{a,act}$ reflects error propagation in the Arrhenius equation,[47] not the error in the linear fit parameters.

Long induction periods have been reported for H_2 reduction of oxide-covered Ni surfaces.[57-58, 63-65] The H_2 sticking coefficient is low,[66] however, adsorption of water on the oxidized Ni surface is strongly exothermic (-170 to -117 kJ mol^{-1}, depending on coverage).[67] H_2 activation on oxygen vacancies[65, 68] can occur only after dehydration of the hydroxyl-terminated surface.[57, 69-70] Heterolytic dissociation of H_2 at a vacancy site produces adjacent [NiH] and [NiOH] sites. When the hydride migrates (as a proton) to a neighboring oxygen, a second hydroxyl group is formed and a Ni(II) ion is reduced to Ni(0). Reduction is strongly autocatalytic, because Ni(0) activates H_2 much more readily than NiO.[57-58]

Finally, when a reduced Ni/γ-Al_2O_3 catalyst was stored under an inert atmosphere to avoid surface oxidation, then used in hydrogenolysis of BPE at 150 °C, the reaction commenced almost immediately, Figure S3.18.

3.3.9 Reaction Network for BPE Hydrogenolysis Catalyzed by Ni(0) Nanoparticles

A Langmuir-Hinshelwood mechanism for the primary reaction is shown in eq 3.3-3.7, where * indicates an unoccupied site on the Ni surface.

$$H_2 + 2\,* \leftrightarrows 2\,H^* \quad (3.3)$$

$$PhCH_2OPh + * \leftrightarrows PhCH_2OPh^* \quad (3.4)$$

$$PhCH_2OPh^* + * \rightarrow PhCH_2^* + PhO^* \quad (3.5)$$

$$PhCH_2^* + H^* \leftrightarrows PhCH_3^* + * \quad (3.6)$$

$$PhO^* + H^* \leftrightarrows PhOH^* + * \quad (3.7)$$

C-O bond cleavage precedes aromatic hydrogenation, and is rate-determining. Adsorption of BPE is likely to require more than one site, but the first-order kinetic behavior suggests that the surface coverage of BPE is low. The weak dependence of the rate on $P(H_2)$ implies that H_2 and BPE do not compete directly for the same adsorption sites.

The 2-PrOH solvent does not supply adsorbed H under the reaction conditions, but its hydroxyl group does undergo rapid Ni(0)-catalyzed exchange with adsorbed H/D. This reaction makes the solvent the primary determinant of the isotopic composition of the adsorbed reducing equivalents. Both of the primary hydrogenolysis products, toluene and phenol, undergo subsequent reactions. Phenol is slowly hydrogenated to cyclohexanol, although subsequent dehydration of cyclohexanol was not observed. While toluene is not

readily hydrogenated, Ni(0) catalyzes facile H/D exchange in its methyl group. The principal reactions are depicted in Scheme 3.5.

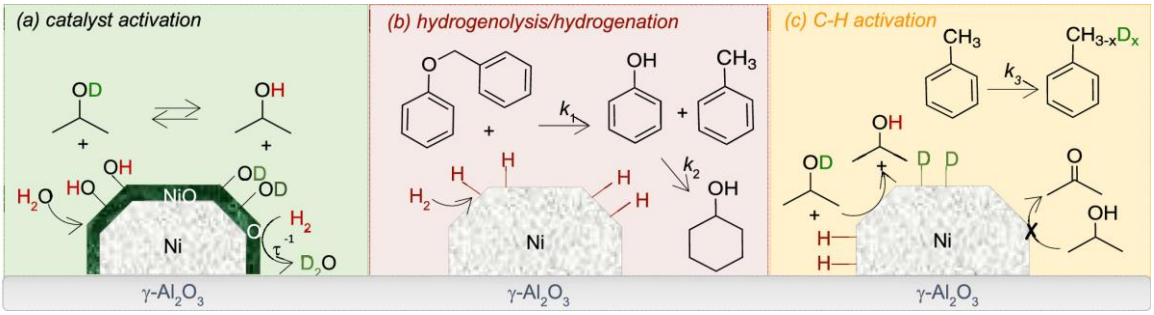

Scheme 3.5. Reaction network for catalytic hydrogenolysis of benzyl phenyl ether (BPE), depicting (a) Ni/γ-Al_2O_3 activation by reduction of the native surface (hydr)oxide, and H/D exchange with the 2-propanol solvent; (b) hydrogenolysis of BPE and subsequent hydrogenation of phenol; and (c) H/D exchange in the solvent and toluene.

3.4 Conclusions

Operando MAS-NMR spectroscopy provides detailed kinetic and mechanistic information about dynamic networks of reactions such as those that occur during hydrogenolysis of lignin and lignin model compounds catalyzed by supported metal catalysts in solution and in the presence of $H_{2(g)}$. Significant amounts of the solvent, as well as some solutes, are present in the vapor phase under these reaction conditions, but can be quantified by simple integration of their NMR signals. Temperature-sensitive solvent chemical shifts serve as an internal thermometer. Fortuitously, the prolonged induction period caused by catalyst activation, as well as its abrupt end, facilitated the collection of high-quality isothermal kinetic data for BPE hydrogenolysis. Benzylic C-O bond cleavage is faster than H/D exchange in toluene, which in turn is faster than phenol hydrogenation.

Efforts are currently underway to examine the kinetics and mechanisms of reductive cleavage of other biomass model compounds, as well as whole lignin/biomass, extending the *operando* MAS-NMR technique to higher temperatures and pressures, and to examine variations in mechanism that arise due to the nature of the metal catalyst.

3.5 Experimental Methods

3.5.1 Chemicals

The following were purchased from commercial suppliers and used as-received: toluene-α-^{13}C and phenol-1-^{13}C (98 %, 99 atom % ^{13}C, Cambridge Isotopes), MnO_2 (≥ 99 %, Reagent Plus, Sigma-Aldrich), K_2CO_3 (99.7 %, Certified ACS, Fisher), 2-PrOH (anhydrous, 99.5 %, Sigma-Aldrich), 2-propanol-d_1 (99 %, 98 atom % D, Sigma-Aldrich), 2-propanol-d_8 (99 %, 99.5 atom % D, Sigma-Aldrich), D_2 (99.995 %, 99.96 atom % D, Sigma-Aldrich), DMSO-d_6 (≥ 99 %, 99.96 atom % D, Sigma-Aldrich), $Ni(NO_3)_2$•$6H_2O$ (98.5 %, Sigma-Aldrich), Br_2 (99.5 %, Merck), CH_2Cl_2, $(CH_3)_2CO$, ethyl acetate, and hexanes (all 99.9 %, Certified ACS), silica gel (230-400 Mesh, Fisher), γ-Al_2O_3 (≥ 97 %, pore volume: 0.40 mL/g, B.E.T. surface area 185 m^2/g, Strem), hydrochloric acid (36.5 wt%, ACS grade, VWR), nitric acid (68 wt%, ACS grade, EMD-Millipore), H_2 (UHP grade, 99.999 %, Oxarc), and N_2O (9.99 vol% in He, Praxair).

3.5.2 Synthesis of ^{13}C-Labelled Benzyl Phenyl Ether (BPE)

^{13}C-labelled benzyl bromide was prepared following a modified literature procedure.[71] Toluene-α-^{13}C (100 mg, 1.07 mmol) was stirred with MnO_2 (93 mg, 1.07 mmol) and Br_2 (60 µL, 1.17 mmol) in CH_2Cl_2 (10 mL) for 1 h in a round-bottom flask (100 mL) until the solution became colorless. The mixture was filtered using a fritted glass Buchner funnel,

then the benzyl bromide was purified on a silica column (elution with 5 % ethyl acetate in hexanes). Yield 145 mg, 80 %.

^{13}C-labelled benzyl phenyl ether (BPE) was synthesized from the labeled benzyl bromide and phenol-1-^{13}C using a modified literature procedure.[72] A 100 mL round-bottom flask equipped with a magnetic stir bar and a condenser was charged with benzyl bromide (145 mg), phenol (100 mg), K_2CO_3 (180 mg) and $(CH_3)_2CO$ (10 mL). The mixture was refluxed for 4 h until benzyl bromide consumption was complete according to TLC. After cooling to room temperature, the reaction mixture was filtered, and the product was purified by elution from a silica column with hexanes. ^{1}H and ^{13}C spectra were recorded on a Varian Unity Inova 500 MHz spectrometer. Chemical shifts were referenced using solvent peaks as internal standards. ^{1}H NMR (500 MHz, DMSO-d_6): δ 5.10 (d, 2H), 7.00-7.02 (m, 2H), 7.28-7.39 (m, 7H). ^{13}C NMR (125 MHz, DMSO-d_6): δ 69.03, 158.29 (^{13}C-labeled positions only, Figure S3.19). Yield 130 mg, 66 %.

3.5.3 Synthesis and Characterization of Ni/γ-Al_2O_3

The catalyst was prepared via incipient wetness impregnation, by stirring γ-Al_2O_3 (0.980 g) with an aqueous solution of $Ni(NO_3)_2$•$6H_2O$ (62.3 mg in 0.400 mL deionized water). The solid was dried in an oven at 75 °C for 4 h, then calcined in air at 850 °C for 5 h, to give a material containing 1.9 wt% Ni (measured by ICP-AES). The metal is fully dispersed as Ni(II) ions in a pseudo-spinel structure according to powder XRD (Figure S3.13). Reduction at 850 °C for 2 h in flowing 5% H_2/N_2 (H5N, Airgas, 99.98 %) resulted in partial (ca. 55 %, based on H_2 uptake) extrusion of Ni(0). According to H_2 chemisorption, the nanoparticles have an average diameter of ca. 14 nm. The dispersion is 7 %, based on the total nickel content of the material.

Prior to the temperature-programmed reduction experiment, a sample of this H_2-reduced catalyst (250 mg, ca. 2 wt% Ni) was exposed to air for 6 d at room temperature (Figure S3.17). To increase sensitivity in XPS measurements, a similar material containing 10.5 wt% Ni was prepared. Details of catalyst characterization by XPS, powder XRD, chemisorption, and HAADF-STEM/EDX mapping are presented in the Supporting Information.

3.5.4 *In situ* EPR Spectroscopy

EPR spectra were acquired on a Bruker Elexsys 580 spectrometer equipped with a SHQE resonator and a Bruker continuous flow liquid nitrogen cryostat (ER4131VT). The microwave frequency was typically 9.34 GHz with a power of 0.2 mW. The field was swept from 0 to 8000 G in 84 s and modulated at a frequency of 100 kHz with 0.5 G amplitude. A time constant of 20 ms was employed.

3.5.5 *Operando* MAS-NMR Spectroscopy

Magic-angle-spinning (MAS) NMR experiments were performed on an Agilent-Varian VNMRS NMR spectrometer equipped with an 11.7 T magnet, operating at 125.7747 MHz for the ^{13}C channel and 500.1822 MHz for the ^{1}H channel. A 5-mm home-built magic-angle spinning (MAS) double resonance HX probe with a custom Pd–coated coil was used to maximize sample magnetic homogeneity. Calibration of the spectrometer temperature setting was performed by acquiring ^{207}Pb NMR spectra of $Pb(NO_3)_2$.[35-36]

In direct polarization (DP) ^{13}C MAS-NMR experiments, a 35 kHz ^{1}H decoupling field was employed, with an acquisition time of 300 ms. The ^{13}C spectral width was 50 kHz, and 15,000 data points were acquired per transient, using a relaxation delay of 60 s to ensure

quantitative analysis. At 25 °C, the T_1 values for the methylene and 1-phenolate ^{13}C resonances of BPE, measured by saturation recovery experiments, are 4.4 and 15.3 s, respectively. For ^{1}H MAS-NMR experiments, spectra were collected by averaging 16 scans, with an acquisition time of 1 s and a relaxation delay of 10 s.

In a typical high *T*/*P* experiment, a customized[32] 5 mm ZrO_2 rotor was loaded with BPE (2.0 mg, 0.011 mmol), Ni/γ-Al_2O_3 (10 mg, 2 wt% Ni) and 2-PrOH (40 μL), then pressurized with 50 bar H_2 (0.16 mmol) at room temperature. The total internal pressure at each temperature was estimated by summing the estimated partial pressures of H_2 and 2-propanol, calculated for a headspace volume that includes the volume of 2-PrOH liquid that vaporized. The MAS rate was 5 kHz. The first spectrum was collected when the probe reached its set temperature, typically 10-15 min after heating of the rotor commenced. Each transient spectrum was acquired by averaging 8 or 16 scans. ^{13}C chemical shifts were referenced to TMS using adamantane as a secondary standard (37.48 ppm).[73]

3.5.6 Batch Reactor Kinetics

BPE hydrogenolysis was conducted in a 25 mL stirred microreactor (Parr 4590) equipped with a sampling port. The reactor was charged with 2-PrOH (10 mL), BPE (0.54 mmol, 100 mg), Ni/γ-Al_2O_3 (ca. 2 wt%, 500 mg), H_2 (50 bar), and *n*-decane (0.054 mmol, 10.5 μL) as internal standard. The reactor was stirred at 300 rpm and heated to 150 °C (requiring a heating time of ca. 10 min for the temperature to stabilize). Aliquots (0.25 mL) were removed at timed intervals for analysis on a Shimadzu GC-2010 gas chromatograph coupled to a Shimadzu GCMS-QP2010 mass spectrometer. The former instrument is equipped with a 30 m × 0.25 mm Agilent DB-1 column with a dimethylpolysiloxane stationary phase (0.25 μm).

3.5.7 Kinetic analyses

Kinetic profiles for conversion of BPE and production of toluene and phenol were analyzed by non-linear least-squares curvefitting using KaleidaGraph (Synergy Software). Concentrations of all species were normalized using the initial concentration of BPE.

3.6 References

(1) Sievers, C.; Noda, Y.; Qi, L.; Albuquerque, E. M.; Rioux, R. M.; Scott, S. L. Phenomena Affecting Catalytic Reactions at Solid–Liquid Interfaces. *ACS Catal.* **2016**, *6*, 8286.

(2) Ragauskas, A. J.; Beckham, G. T.; Biddy, M. J.; Chandra, R.; Chen, F.; Davis, M. F.; Davison, B. H.; Dixon, R. A.; Gilna, P.; Keller, M.; Langan, P.; Naskar, A. K.; Saddler, J. N.; Tschaplinski, T. J.; Tuskan, G. A.; Wyman, C. E. Lignin Valorization: Improving Lignin Processing in the Biorefinery. *Science* **2014**, *344*.

(3) Tuck, C. O.; Pérez, E.; Horváth, I. T.; Sheldon, R. A.; Poliakoff, M. Valorization of Biomass: Deriving More Value from Waste. *Science* **2012**, *337*, 695.

(4) Zakzeski, J.; Bruijnincx, P. C. A.; Jongerius, A. L.; Weckhuysen, B. M. The Catalytic Valorization of Lignin for the Production of Renewable Chemicals. *Chem. Rev.* **2010**, *110*, 3552.

(5) Calvo-Flores, F. G.; Dobado, J. A. Lignin as Renewable Raw Material. *ChemSusChem* **2010**, *3*, 1227.

(6) Azadi, P.; Inderwildi, O. R.; Farnood, R.; King, D. A. Liquid Fuels, Hydrogen and Chemicals from Lignin: A Critical Review. *Renew. Sust. Energ. Rev.* **2013**, *21*, 506.

(7) Kandanarachchi, P. H.; Autrey, T.; Franz, J. A. Model Compound Studies of the β-O-4 Linkage in Lignin: Absolute Rate Expressions for β-Scission of Phenoxyl

Radical from 1-Phenyl-2-phenoxyethanol-1-yl Radical. *J. Org. Chem* **2002**, *67*, 7937.

(8) Parthasarathi, R.; Romero, R. A.; Redondo, A.; Gnanakaran, S. Theoretical Study of the Remarkably Diverse Linkages in Lignin. *J. Phys. Chem. Lett.* **2011**, *2*, 2660.

(9) Beste, A.; Buchanan, A. C. Role of Carbon–Carbon Phenyl Migration in the Pyrolysis Mechanism of β-O-4 Lignin Model Compounds: Phenethyl Phenyl Ether and α-Hydroxy Phenethyl Phenyl Ether. *J. Phys. Chem. A* **2012**, *116*, 12242.

(10) Lankau, T.; Yu, C.-H. Intermediate Oxiranes in the Base-Catalyzed Depolymerisation of Lignin. *Green Chem.* **2016**, *18*, 1590.

(11) Lu, J.; Wang, M.; Zhang, X.; Heyden, A.; Wang, F. β-O-4 Bond Cleavage Mechanism for Lignin Model Compounds over Pd Catalysts Identified by Combination of First-Principles Calculations and Experiments. *ACS Catal.* **2016**, *6*, 5589.

(12) Li, Q.; López, N. Chirality, Rigidity, and Conjugation: A First-Principles Study of the Key Molecular Aspects of Lignin Depolymerization on Ni-Based Catalysts. *ACS Catal.* **2018**, 4230.

(13) Bernt, C. M.; Bottari, G.; Barrett, J. A.; Scott, S. L.; Barta, K.; Ford, P. C. Mapping Reactivities of Aromatic Models with a Lignin Disassembly Catalyst. Steps Toward Controlling Product Selectivity. *Catal. Sci. Tech.* **2016**, *6*, 2984.

(14) Kim, S.; Chmely, S. C.; Nimlos, M. R.; Bomble, Y. J.; Foust, T. D.; Paton, R. S.; Beckham, G. T. Computational Study of Bond Dissociation Enthalpies for a Large Range of Native and Modified Lignins. *J. Phys. Chem. Lett.* **2011**, *2*, 2846.

(15) Froass, P. M.; Ragauskas, A. J.; Jiang, J.-E. Chemical Structure of Residual Lignin from Kraft Pulp. *J. Wood Chem. Technol.* **1996**, *16*, 347.

(16) Tobisu, M.; Chatani, N. Catalytic Hydrogenolysis of C-O Bonds in Aryl Ethers. *ChemCatChem* **2011**, *3*, 1410.

(17) Samant, B. S.; Kabalka, G. W. Hydrogenolysis-Hydrogenation of Aryl Ethers: Selectivity Pattern. *Chem. Commun.* **2012**, *48*, 8658.

(18) Kelley, P.; Lin, S.; Edouard, G.; Day, M. W.; Agapie, T. Nickel-Mediated Hydrogenolysis of C–O Bonds of Aryl Ethers: What Is the Source of the Hydrogen? *J. Am. Chem. Soc.* **2012**, *134*, 5480.

(19) Zaheer, M.; Kempe, R. Catalytic Hydrogenolysis of Aryl Ethers: A Key Step in Lignin Valorization to Valuable Chemicals. *ACS Catal.* **2015**, *5*, 1675.

(20) Sun, Z.; Fridrich, B.; de Santi, A.; Elangovan, S.; Barta, K. Bright Side of Lignin Depolymerization: Toward New Platform Chemicals. *Chem. Rev.* **2018**, *118*, 614.

(21) Schutyser, W.; Renders, T.; Van den Bosch, S.; Koelewijn, S. F.; Beckham, G. T.; Sels, B. F. Chemicals from Lignin: an Interplay of Lignocellulose Fractionation, Depolymerisation, and Upgrading. *Chem. Soc. Rev.* **2018**, *47*, 852.

(22) Song, Q.; Wang, F.; Cai, J.; Wang, Y.; Zhang, J.; Yu, W.; Xu, J. Lignin Depolymerization (LDP) in Alcohol over Nickel-Based Catalysts via a Fragmentation-Hydrogenolysis Process. *Energy Environ. Sci.* **2013**, *6*, 994.

(23) Zhang, X.; Chen, X.; Jin, S.; Peng, Z.; Liang, C. Ni/Al_2O_3 Catalysts Derived from Layered Double Hydroxide and Their Applications in Hydrodeoxygenation of Anisole. *ChemistrySelect* **2016**, *1*, 577.

(24) Gómez-Monedero, B.; Ruiz, M. P.; Bimbela, F.; Faria, J. Selective Hydrogenolysis of α-O-4, β-O-4, 4-O-5 CO Bonds of Lignin-Model Compounds and Lignin-Containing Stillage Derived from Cellulosic Bioethanol Processing. *Appl. Catal., A* **2017**, *541*, 60.

(25) Cui, X.; Yuan, H.; Junge, K.; Topf, C.; Beller, M.; Shi, F. A Stable and Practical Nickel Catalyst for the Hydrogenolysis of C-O Bonds. *Green Chem.* **2017**, *19*, 305.

(26) Payne, B. P.; Grosvenor, A. P.; Biesinger, M. C.; Kobe, B. A.; McIntyre, N. S. Structure and Growth of Oxides on Polycrystalline Nickel Surfaces. *Surf. Interface Anal.* **2007**, *39*, 582.

(27) Song, P.; Wen, D.; Guo, Z. X.; Korakianitis, T. Oxidation Investigation of Nickel Nanoparticles. *Phys. Chem. Chem. Phys.* **2008**, *10*, 5057.

(28) D'Addato, S.; Grillo, V.; Altieri, S.; Tondi, R.; Valeri, S.; Frabboni, S. Structure and Stability of Nickel/Nickel Oxide Core-Shell Nanoparticles. *J. Phys. Condens. Matter* **2011**, *23*, 175003.

(29) Gómez, S.; Torres, C.; García Fierro, J. L.; Apesteguía, C. R.; Reyes, P. Hydrogenation of Nitrobenzene on Au/ZrO_2 Catalysts. *J. Chil. Chem. Soc.* **2012**, *57*, 1194.

(30) Gu, S.; Wunder, S.; Lu, Y.; Ballauff, M.; Fenger, R.; Rademann, K.; Jaquet, B.; Zaccone, A. Kinetic Analysis of the Catalytic Reduction of 4-Nitrophenol by Metallic Nanoparticles. *J. Phys. Chem. C* **2014**, *118*, 18618.

(31) Konuspaev, S. R.; Zhanbekov, K. N.; Kul'Kova, N. V.; Murzin, D. Y. Kinetics of 4-Tert-butylphenol Hydrogenation Over Rhodium. *Chem. Eng. Technol.* **1997**, *20*, 144.

(32) Walter, E. D.; Qi, L.; Chamas, A.; Mehta, H. S.; Sears, J. A.; Scott, S. L.; Hoyt, D. W. Operando MAS NMR Reaction Studies at High Temperatures and Pressures. *J. Phys. Chem. C* **2018**, *122*, 8209.

(33) Chamas, A.; Qi, L.; Mehta, H. S.; Sears, J. A.; Scott, S. L.; Walter, E. D.; Hoyt, D. W. High Temperature/Pressure MAS-NMR for the Study of Dynamic Processes in Mixed Phase Systems. *Magn. Reson. Imaging* **2019**, *56*, 37.

(34) True, N. S., Gas Phase Applications of NMR Spectroscopy. In Encyclopedia of Spectroscopy and Spectrometry, 2nd ed.; Academic Press: Oxford, 2010; pp 749.

(35) Bielecki, A.; Burum, D. P. Temperature Dependence of ^{207}Pb MAS Spectra of Solid Lead Nitrate. An Accurate, Sensitive Thermometer for Variable-temperature MAS. *J. Magn. Reson., Ser. A* **1995**, *116*, 215.

(36) Langer, B.; Schnell, I.; Spiess, H. W.; Grimmer, A.-R. Temperature Calibration under Ultrafast MAS Conditions. *J. Magn. Reson.* **1999**, *138*, 182.

(37) Sharma, V. K.; Baiker, A. Superparamagnetic Effects in the Ferromagnetic Resonance of Silica Supported Nickel Particles. *J. Chem. Phys.* **1981**, *75*, 5596.

(38) Kong, L.; Li, G.; Jin, L.; Hu, H. Effects of the Oxygen Substituent on the Pyrolysis of Phenyl Ethers on a Fixed-Bed Reactor. *J. Anal. Appl. Pyrolysis* **2015**, *115*, 362.

(39) Luo, Y.-R., Comprehensive Handbook of Chemical Bond Energies. CRC Press: 2007; p 325.

(40) He, J.; Zhao, C.; Lercher, J. A. Ni-Catalyzed Cleavage of Aryl Ethers in the Aqueous Phase. *J. Am. Chem. Soc.* **2012**, *134*, 20768.

(41) Krüger, M. B.; Selle, C.; Heller, D.; Baumann, W. Determination of Gas Concentrations in Liquids by Nuclear Magnetic Resonance: Hydrogen in Organic Solvents. *J. Chem. Eng. Data* **2012**, *57*, 1737.

(42) Limbach, H.-H.; Pery, T.; Rothermel, N.; Chaudret, B.; Gutmann, T.; Buntkowsky, G. Gas Phase ^{1}H NMR Studies and Kinetic Modeling of Dihydrogen Isotope

Equilibration Catalyzed by Ru-Nanoparticles under Normal Conditions: Dissociative vs. Associative Exchange. *Phys. Chem. Chem. Phys.* **2018**, *20*, 10697.

(43) Jaatinen, S.; Touronen, J.; Karinen, R.; Uusi-Kyyny, P.; Alopaeus, V. Hydrogen Solubility in Furfural and 2-Propanol: Experiments and Modeling. *J. Chem. Thermodyn.* **2017**, *112*, 1.

(44) Espenson, J. H., Chemical Kinetics and Reaction Mechanisms. McGraw-Hill: New York, 2002.

(45) Qi, S.-C.; Zhang, L.; Kudo, S.; Norinaga, K.; Hayashi, J.-i. Theoretical Study on Hydrogenolytic Cleavage of Intermonomer Linkages in Lignin. *J. Phys. Chem. A* **2017**, *121*, 2868.

(46) Kang, M.; DeWilde, J. F.; Bhan, A. Kinetics and Mechanism of Alcohol Dehydration on γ-Al_2O_3: Effects of Carbon Chain Length and Substitution. *ACS Catal.* **2015**, *5*, 602.

(47) Steigel, A.; Sauer, J.; Kleier, D. A.; Binsch, G. Nitrogen Analogs of Cycloheptatrienes and Norcaradienes. Nuclear Magnetic Resonance Study of their Thermodynamic and Kinetic Properties. *J. Am. Chem. Soc.* **1972**, *94*, 2770.

(48) Vjunov, A.; Hu, M. Y.; Feng, J.; Camaioni, D. M.; Mei, D.; Hu, J. Z.; Zhao, C.; Lercher, J. A. Following Solid-Acid-Catalyzed Reactions by MAS NMR Spectroscopy in Liquid Phase—Zeolite-Catalyzed Conversion of Cyclohexanol in Water. *Angew. Chem. Int. Ed.* **2014**, *53*, 479.

(49) Capponi, M.; Gut, I. G.; Hellrung, B.; Persy, G.; Wirz, J. Ketonization Equilibria of Phenol in Aqueous Solution. *Can. J. Chem.* **1999**, *77*, 605.

(50) Mamaladze, L. M.; Gudkov, B. S.; Kiperman, S. L. Mechanism of Catalytic Hydrogenation of Toluene on Nickel Catalyst. *Bull. Acad. Sci. USSR, Div. Chem. Sci.* **1974**, *23*, 2512.

(51) Alshehri, F.; Weinert, H. M.; Jackson, S. D. Hydrogenation of Alkylaromatics over Rh/Silica. *React. Kinet., Mech. Catal.* **2017**, *122*, 699.

(52) Shin, E.-J.; Keane, M. A. Gas-Phase Hydrogenation/Hydrogenolysis of Phenol over Supported Nickel Catalysts. *Ind. Eng. Chem. Res.* **2000**, *39*, 883.

(53) Vonk, V.; Khorshidi, N.; Stierle, A. Structure and Oxidation Behavior of Nickel Nanoparticles Supported on YSZ(111). *J. Phys. Chem. C* **2017**, *121*, 2798.

(54) Allen, G. C.; Tucker, P. M.; Wild, R. K. Surface Oxidation of Nickel Metal as Studied by X-Ray Photoelectron Spectroscopy. *Oxid. Met.* **1978**, *13*, 223.

(55) Rellinghaus, B.; Stappert, S.; Wassermann, E. F.; Sauer, H.; Spliethoff, B. The Effect of Oxidation on the Structure of Nickel Nanoparticles. *Eur. Phys. J. D* **2001**, *16*, 249.

(56) Kehres, J.; Andreasen, J. W.; Fløystad, J. B.; Liu, H.; Molenbroek, A.; Jakobsen, J. G.; Chorkendorff, I.; Nielsen, J. H.; Høydalsvik, K.; Breiby, D. W.; Vegge, T. Reduction of a Ni/Spinel Catalyst for Methane Reforming. *J. Phys. Chem. C* **2014**, *119*, 1424.

(57) Richardson, J. T.; Scates, R.; Twigg, M. V. X-ray Diffraction Study of Nickel Oxide Reduction by Hydrogen. *Appl. Catal., A* **2003**, *246*, 137.

(58) Rodriguez, J. A.; Hanson, J. C.; Frenkel, A. I.; Kim, J. Y.; Perez, M. Experimental and Theoretical Studies on the Reaction of H_2 with NiO: Role of O Vacancies and Mechanism for Oxide Reduction. *J. Am. Chem. Soc.* **2002**, *124*, 346.

(59) Xu, S.; Walter, E. D.; Zhao, Z.; Hu, M. Y.; Han, X.; Hu, J. Z.; Bao, X. Dynamic Structural Changes of SiO_2 Supported Pt–Ni Bimetallic Catalysts over Redox Treatments Revealed by NMR and EPR. *J. Phys. Chem. C* **2015**, *119*, 21219.

(60) Alonso, F.; Riente, P.; Sirvent, J. A.; Yus, M. Nickel Nanoparticles in Hydrogen-Transfer Reductions: Characterisation and Nature of the Catalyst. *Appl. Catal., A* **2010**, *378*, 42.

(61) Borgschulte, A.; Westerwaal, R. J.; Rector, J. H.; Dam, B.; Griessen, R. Hydrogen Sorption Mechanism of Oxidized Nickel Clusters. *Appl. Phys. Lett.* **2004**, *85*, 4884.

(62) Salagre, P.; Fierro, J. L. G.; Medina, F.; Sueiras, J. E. Characterization of Nickel Species on Several γ-alumina Supported Nickel Samples. *J. Mol. Catal. A: Chem.* **1996**, *106*, 125.

(63) Syed-Hassan, S. S. A.; Li, C.-Z. NiO Reduction with Hydrogen and Light Hydrocarbons: Contrast Between SiO_2-Supported and Unsupported NiO Nanoparticles. *Appl. Catal., A* **2011**, *398*, 187.

(64) Furstenau, R. P.; McDougall, G.; Langell, M. A. Initial Stages of Hydrogen Reduction of NiO(100). *Surf. Sci.* **1985**, *150*, 55.

(65) Villarrubia, J. S.; Ho, W. Reaction of Hydrogen with Adsorbed Oxygen on Ni(110). *Surf. Sci.* **1984**, *144*, 370.

(66) Hock, M.; Küppers, J. Interaction of Hydrogen and Oxygen at Ni(111) Surfaces. *Surf. Sci.* **1987**, *188*, 575.

(67) Zhao, W.; Bajdich, M.; Carey, S.; Vojvodic, A.; Nørskov, J. K.; Campbell, C. T. Water Dissociative Adsorption on NiO(111): Energetics and Structure of the Hydroxylated Surface *ACS Catal.* **2016**, *6*, 7377.

(68) Benton, A. F.; Emmett, P. H. The Reduction of Nickelous and Ferric Oxides by Hydrogen. *J. Am. Chem. Soc.* **1924**, *46*, 2728.

(69) Xu, Q.; Cheah, S.; Zhao, Y. Initial Reduction of the NiO(100) Surface in Hydrogen. *J. Chem. Phys.* **2013**, *139*, 024704.

(70) Chen, J. G.; Fischer, D. A.; Hardenbergh, J. H.; Hall, R. B. A Fluorescence-Yield Near-Edge Spectroscopy (FYNES) Investigation of the Reaction Kinetics of NiO/Ni(100) with Hydrogen. *Surf. Sci.* **1992**, *279*, 13.

(71) Mathew, K. M.; Ravi, S.; Unny, V. K. P.; Sivaprasad, N. Microwave-Assisted Synthesis of (RS) Methyl-2-([2'-^{14}C]4,6-dimethoxypyrimidin-2'-yloxy)-2-phenyl [1-^{14}C]ethanoate. *J. Label. Compd. Radiopharm* **2006**, *49*, 699.

(72) Wu, W.-B.; Huang, J.-M. Electrochemical Cleavage of Aryl Ethers Promoted by Sodium Borohydride. *J. Org. Chem* **2014**, *79*, 10189.

(73) Morcombe, C. R.; Zilm, K. W. Chemical Shift Referencing in MAS Solid State NMR. *J. Magn. Reson.* **2003**, *162*, 479.

3.7 Appendix II

3.7.1 Characterization of Ni/γ-Al_2O_3

Elemental analysis by ICP-AES was conducted on a Thermo Model iCAP 6300 instrument. The catalyst (50.0 mg) was digested overnight in 2.4 mL aqua regia (3:1 v/v HCl:HNO_3) at 80 °C, then diluted to 20 mL with deionized water. Calibration curves were constructed with four solutions (0.1, 1, 10, and 100 ppm) prepared by diluting a standard solution (Inorganic Ventures, 1000 ppm Ni in 2 % HNO_3). Data were processed with the software iTEVA.

The accessible metal surface area was determined by selective oxidation of surface Ni atoms with N_2O, followed by titration with H_2,[1] using a Micrometrics Autochem ii 2920. A U-shaped quartz reactor was packed with a plug of quartz wool which supported a catalyst bed of 110 mg. A thermocouple was attached to the outside of the reactor, at the level of the middle of the bed. The temperature was ramped to 300 °C at 10 °C min^{-1} under flowing Ar. After holding at 300 °C for 1 h, the reactor was cooled to room temperature under flowing Ar. The catalyst was then heated in H_2/Ar (10 vol%) to 850 °C at a ramp rate of 10 °C min^{-1} and was held at 850 °C for 2 h before cooling to room temperature under flowing He. The reduced material was heated in flowing N_2O (9.99 vol% in He) at 60 °C for 45 min to oxidize surface Ni atoms, eq S3.1. The Ni surface area was then determined by the H_2 uptake during temperature-programmed reduction (TPR), eq S3.2.

$$Ni(0) + N_2O \rightarrow NiO + N_2 \qquad \text{(S3.1)}$$

$$NiO + H_2 \rightarrow Ni(0) + H_2O \qquad \text{(S3.2)}$$

The metal surface area, SA_{Ni} (m^2 g_{Ni}^{-1}), estimated nanoparticle size, d_{Ni} (nm), and Ni dispersion, D_{Ni} (%), were calculated using eq S3.3-S3.5, assuming spherical Ni nanoparticles.

$$SA_{Ni}(m^2\ g_{Ni}{}^{-1}) = \frac{n_{H_2}\ N_A\ SF}{m_{cat}\ W_{Ni}\ A_{Ni}} \quad \text{(S3.3)}$$

$$d_{Ni}(nm) = \frac{6 \times 10^3}{SA_{Ni}\ \rho_{Ni}} \quad \text{(S3.4)}$$

$$D_{Ni}(\%) = \frac{n_{H_2}\ M_{Ni}\ SF}{W_{Ni}\ m_{cat}} \times 100\,\% \quad \text{(S3.5)}$$

Here, n_{H2} is the amount of H_2 consumed, N_A is Avogadro's number, SF is the stoichiometric coefficient of H_2 in eq S3.2, m_{cat} is the mass of catalyst, W_{Ni} is the weight fraction of Ni determined by ICP (i.e., 1.9% or 10.5%), A_{Ni} is the areal density of metallic Ni, 1.54 x 10^{19} atoms m^{-2}, ρ_{Ni} is the bulk Ni density, 8.90 g cm^{-3}, and M_{Ni} is the atomic mass of Ni. The catalyst containing ca. 2 wt% Ni has a metal surface area of 48 m^2 g_{Ni}^{-1}. Based on the total metal content, this surface area corresponds to 14 nm particles (Table S3.1). However, the material contains ca. 55 % Ni(0) and 45 % residual Ni^{2+}, according to H_2 uptake during reduction of the calcined catalyst precursor (see main text). The dispersion (surface Ni(0) sites) represents ca. 7 % of the total Ni content. The catalyst containing 10 wt% Ni has a similar metal surface area, 46 m^2 g_{Ni}^{-1}, corresponding to 15 nm particles and ca. 7 % dispersion based on total Ni content.

The powder X-ray diffraction (XRD) pattern of Ni/γ-Al_2O_3 was collected on a Philips X'PERT MPD, using Cu K_α (1.5405 Å) radiation. The diffractogram was indexed using the X'PERT High Score software package. It shows three new, broad reflections at 2θ = 44.4, 51.9, 76.9 and 93.1 °, in addition to the expected reflections for γ-Al_2O_3 (see Figure S3.13).

The latter are shifted slightly to lower angles relative to unmodified γ-Al_2O_3, presumably because of the presence of residual Ni^{2+} in the latttice. The new reflections were indexed to metallic Ni with a cubic close-packed structure in the *Fm3m* space group.[2] The peak widths suggest that the Ni nanoparticles are ca. 20 nm in diameter.

Table S3.1. Properties of Ni nanoparticles supported on γ-Al_2O_3

Ni Loading	Ni surface area (m^2 g_{Ni}^{-1})	Average particle size (nm)[a]	Ni dispersion (%)
2 wt%	47.7(4)	14.1(1)	7.2(1)
10 wt%	45.8(9)	14.7(3)	6.9(2)

[a] Estimated from the measured Ni(0) surface area.

X-ray photoelectron spectroscopy (XPS) was performed on a Kratos Ultra system equipped with an Al-Kα (1559 eV) radiation source. Prior to data collection, a baseline vacuum of 1 x 10^{-8} Torr was achieved. High resolution scans were acquired with a band pass energy of 40 eV. Binding energies were calibrated using the 1s peak of adventitious carbon at 284.6 eV. Deconvolution of the Ni $2p_{3/2}$ region was performed using the Casa XPS software package. The calcined catalyst precursor shows a well-defined $2p_{3/2}$ peak at 855.8 eV, with a small contribution at 857.8 eV (Figure S3.15a). These peak positions are consistent with the presence of NiO (major component) and $NiAl_2O_4$ (minor component), respectively.[3-4] The broad feature at 862.1 eV is a result of the multi-electron shake-up process that is observed only for cationic nickel. After high temperature H_2 reduction, a new feature appeared at 852.4 eV, corresponding to a metallic Ni phase (Figure S3.15b). It persisted despite air exposure of the sample.[5] Peak positions and assignments are summarized in Table S3.2. The signal-to-noise ratio in the Ni 2*p* region of the spectrum is

much lower for the reduced catalyst compared to the spectrum of the calcined catalyst precursor. This is likely a result of overcoating by γ-Al_2O_3, which is known to occur during the extrusion of Ni nanoparticles.[6]

Table S3.2. XPS binding energies in the Ni 2*p* region (eV)

Material	$2p_{3/2}$			Satellite	$2p_{1/2}$	Satellite
	Ni(0)	NiO	$NiAl_2O_4$			
Catalyst precursor	-	855.8	857.8	862.1	873.4	879.8
Ni/γ-Al_2O_3 (air-exposed)	852.4	855.9	n.d.	861.9	873.2	880.3

n.d. not detected.

To prepare a sample for transmission electron microscopy (TEM) imaging, the catalyst was first ground in a mortar with a pestle, then suspended in absolute ethanol and sonicated for 15 min. The resulting suspension was drop-cast onto a Cu-coated ultrathin carbon grid and allowed to dry in air for 15 min to allow the solvent to evaporate. High angle annular dark field scanning transmission electron microscopy (HAADF STEM) images were acquired on a FEI Tecnai G^2 F20 S-Twin field emission transmission electron microscope. EDX mapping shows evidence for Ni-Al segregation in the reduced Ni catalyst, and suggests the presence of a surface oxide on the metal nanoparticles (Figure S3.16).

Variable temperature EPR spectra of air-exposed Ni/γ-Al_2O_3 were collected in a 4 mm OD quartz tube (Wilmad). In situ EPR spectra of reduced Ni/γ-Al_2O_3 were acquired by immobilizing the sample in a 3 mm OD × 2 mm ID quartz tube with open ends with a plug of quartz wool on either side. This smaller tube was placed in a 5 mm OD EPR tube and the gas path controlled with a T-fitting such that the incoming gas flowed first down the space inside the 5 mm tube and outside the 3 mm tube, then turned and flowed over the sample inside the 3 mm tube and out to exhaust. This route was chosen so that when the assembly

was placed in a variable temperature insert in the EPR resonator, the flowing gas equilibrated its temperature with that of the VT insert before entering the sample.

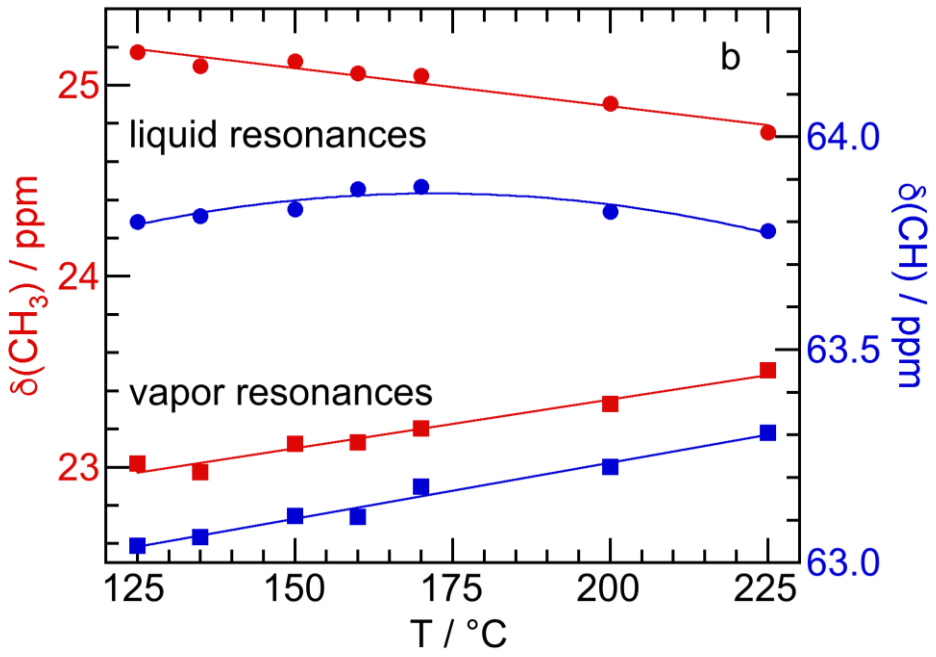

Figure S3.1. Temperature evolution of the methyl and methine resonances in both liquid (circles) and vapor (squares) phases of 2-PrOH sealed in a high T/P rotor, recorded by direct polarization ^{13}C MAS-NMR spectroscopy. The 5-mm o.d. NMR rotor (internal volume 140 μL) was charged with 40 μL 2-PrOH and 50 bar H_2 at room temperature. Total internal pressures were estimated to range from 71 bar at 125 ºC to 118 bar at 225 ºC.

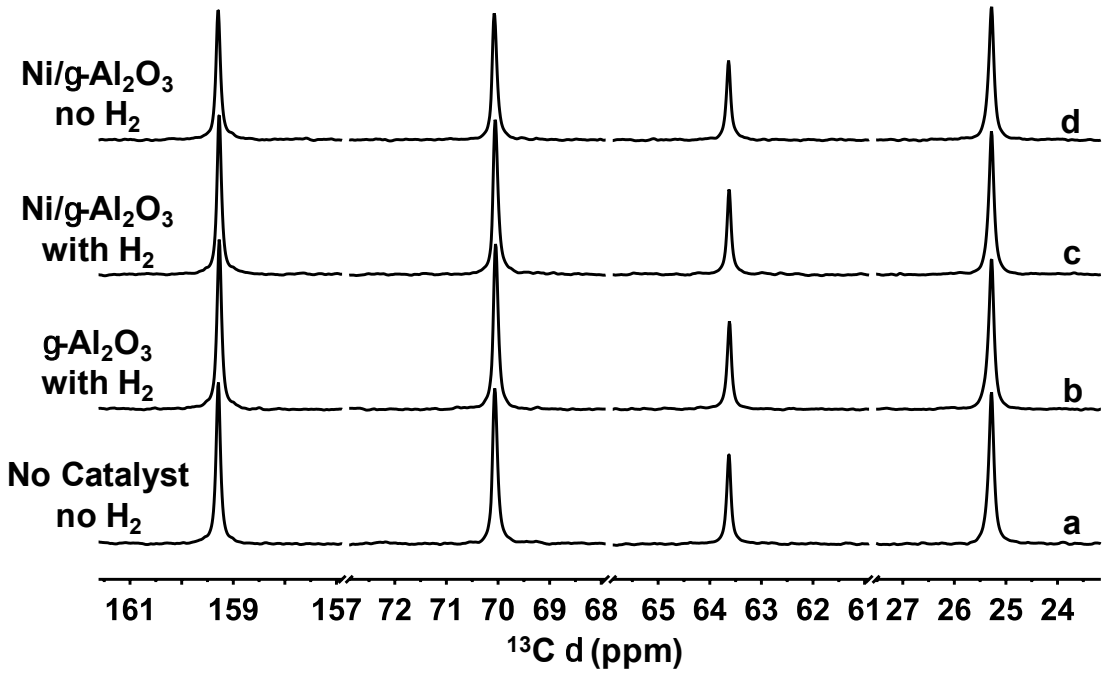

Figure S3.2. ^{13}C MAS-NMR spectra of ^{13}C-labeled BPE in 2-PrOH, recorded at 25 °C: (a) without catalyst or H_2; (b) with γ-Al_2O_3 (10 mg) and 50 bar H_2; (c) with 2 wt% Ni/γ-Al_2O_3 (10 mg) and 50 bar H_2 (estimated total internal pressure 79 bar at 150 °C); and (d) with 2 wt% Ni/γ-Al_2O_3 (10 mg) but no H_2. In all spectra, there is no apparent difference in either lineshape or chemical shift for any of the signals of BPE or 2-PrOH due to the presence of solids or H_2. MAS rate: 5 kHz.

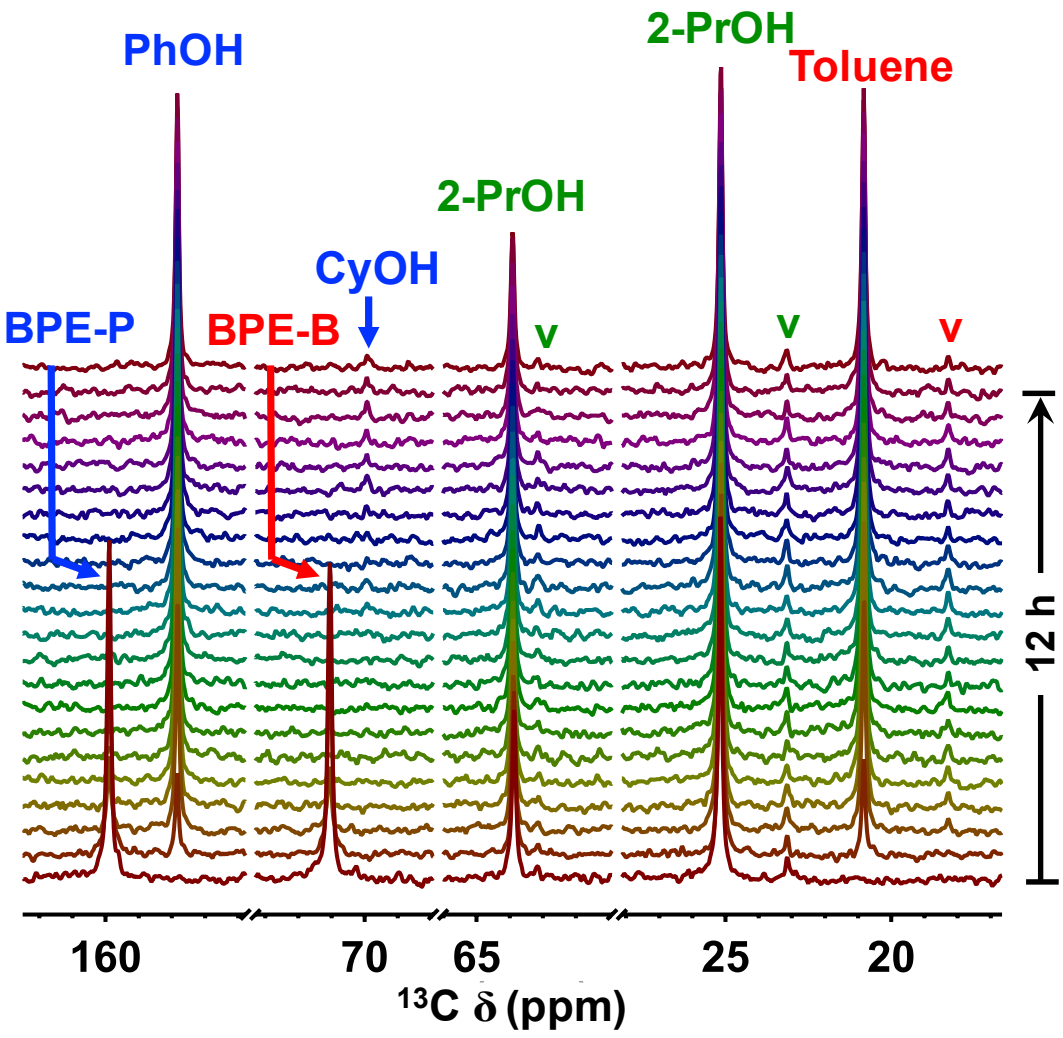

Figure S3.3. *Operando* ^{13}C MAS-NMR spectra recorded during the reaction of BPE (2.0 mg, 0.011 mmol) in 2-PrOH (40 μL, 0.52 mmol) with 50 bar H_2 (0.20 mmol), catalyzed by 2 wt% Ni/γ-Al_2O_3 (10 mg, air-exposed) at 150 °C, showing the formation of cyclohexanol (CyOH) at extended reaction times. Each spectrum was acquired with 16 scans and a recycle delay of 60 s. MAS rate: 5 kHz. Vapor phase signals are indicated by v. Estimated total internal pressure 79 bar at 150 ºC.

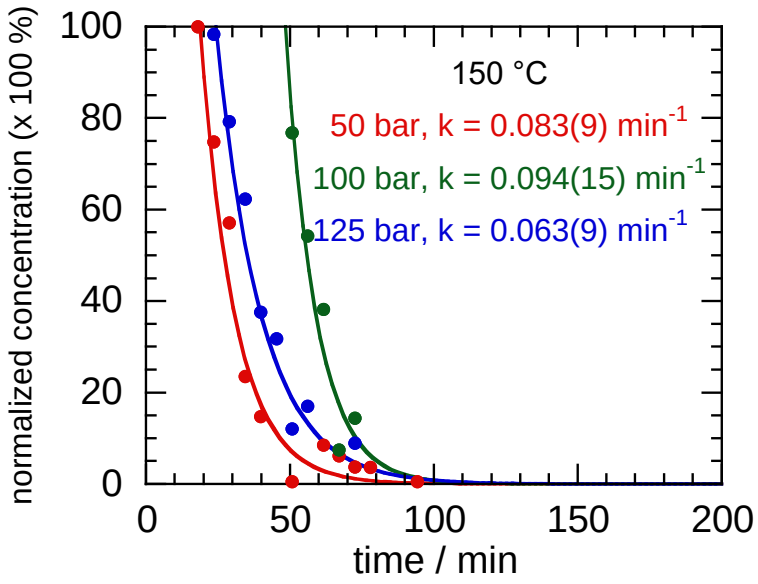

Figure S3.4. Comparison of reaction profiles for BPE conversion in 2-PrOH, catalyzed by Ni/γ-Al_2O_3 (2 wt%, H_2-reduced then air-exposed) at 150 °C, in a rotor charged with 50 (red), 100 (green), and 125 (blue) bar H_2 (estimated total internal pressures: 79, 149, and 184 bar, respectively). Concentrations were calculated from the peak area of the BPE-B ^{13}C resonance at 70.1 ppm. Solid lines are non-linear least-squares curvefits to the first-order rate equation. Data collected during the induction period were removed prior to curvefitting.

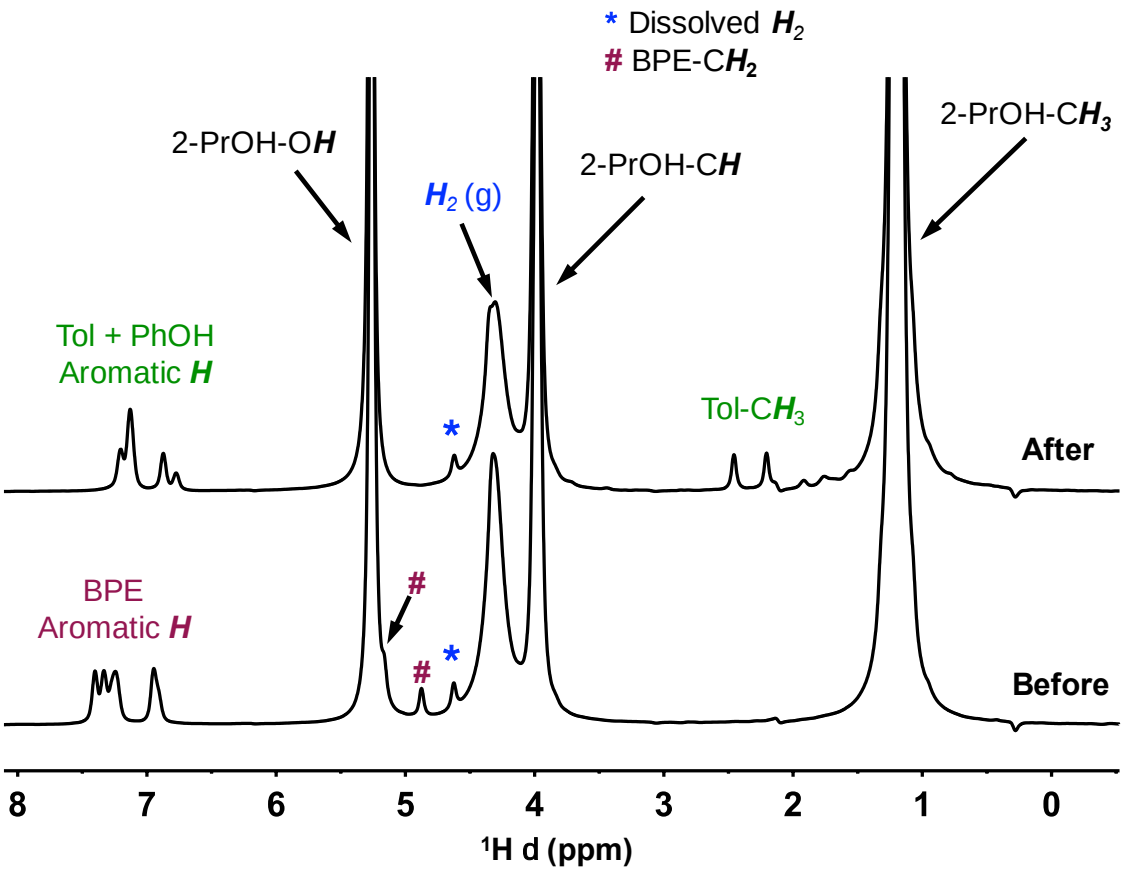

Figure S3.5. ^{1}H MAS-NMR spectra of ^{13}C-labeled BPE (2.0 mg, 0.011 mmol) in 2-PrOH (40 μL, 0.52 mmol) with 50 bar H_2 (0.20 mmol) over Ni/γ-Al_2O_3 (10 mg), recorded at 25 °C before reaction at 150 °C for 10 h in a high T/P rotor (5 mm), as well as after the reaction (and cooling the rotor to 25 °C). The total internal pressure was estimated to be 79 bar at 150 °C. Spectra were collected by averaging 16 scans, with an acquisition time of 1 s and a relaxation delay of 10 s. Line broadening of 15 Hz was applied. * and # denote signals for dissolved H_2 and BPE-methylene, respectively.

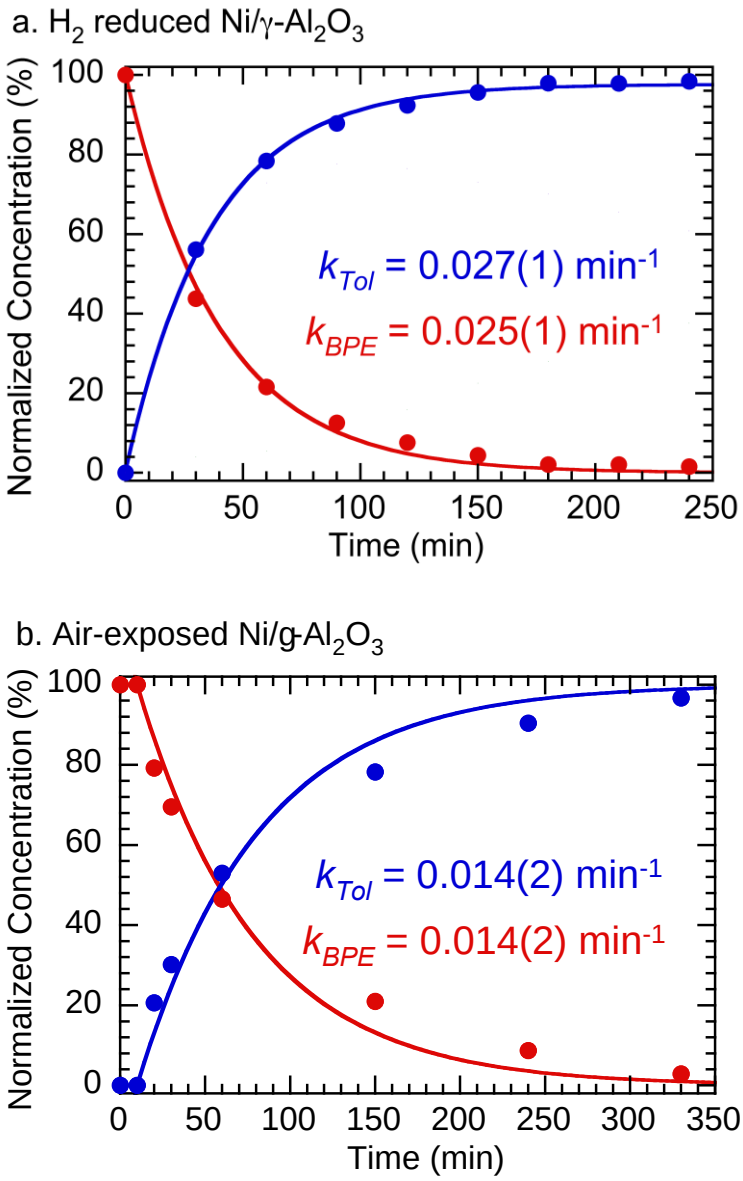

Figure S3.6. First-order curvefits of kinetic profiles and pseudo-first-order rate constants (min^{-1}) for conversion of BPE (100 mg, 0.54 mmol) and formation of toluene in 2-PrOH (10 mL), recorded in the presence of (a) 2 wt% Ni/γ-Al_2O_3 (500 mg, H_2-reduced), and (b) 2 wt% Ni/γ-Al_2O_3 (500 mg, air-exposed) with 50 bar H_2 (total internal pressure estimated to be 79 bar at 150 ºC) in a 25 mL Parr batch reactor. The data shown represents aliquots withdrawn after the reactor temperature reached 150 °C. The curvefits in (b) were performed excluding the first two data points, corresponding to the induction period.

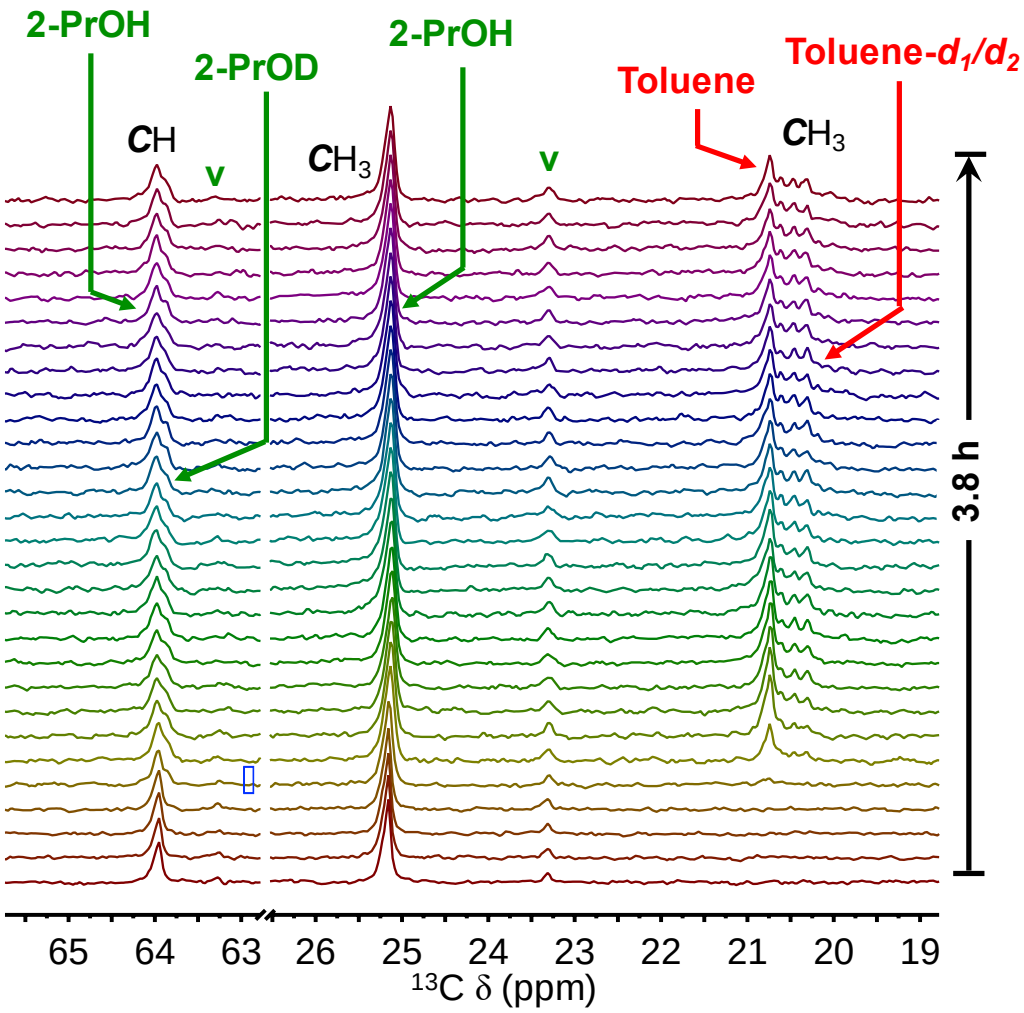

Figure S3.7. *Operando* ^{13}C MAS-NMR spectra recorded for BPE (2.0 mg, 0.011 mmol) in 2-PrOH (40 μL, 0.52 mmol) with 50 bar D_2 (0.20 mmol) catalyzed by air-exposed 2 wt% Ni/γ-Al_2O_3 (10 mg) at 175 °C, emphasizing the methine and methyl resonances of 2-PrOH, and the methyl resonance of toluene. Total internal pressure estimated to be 89 bar at 175 °C. ★ denotes the first spectrum at which onset of H/D exchange in 2-PrOH becomes visible. Each spectrum was acquired with 16 scans and a recycle delay of 60 s. MAS rate: 5 kHz.

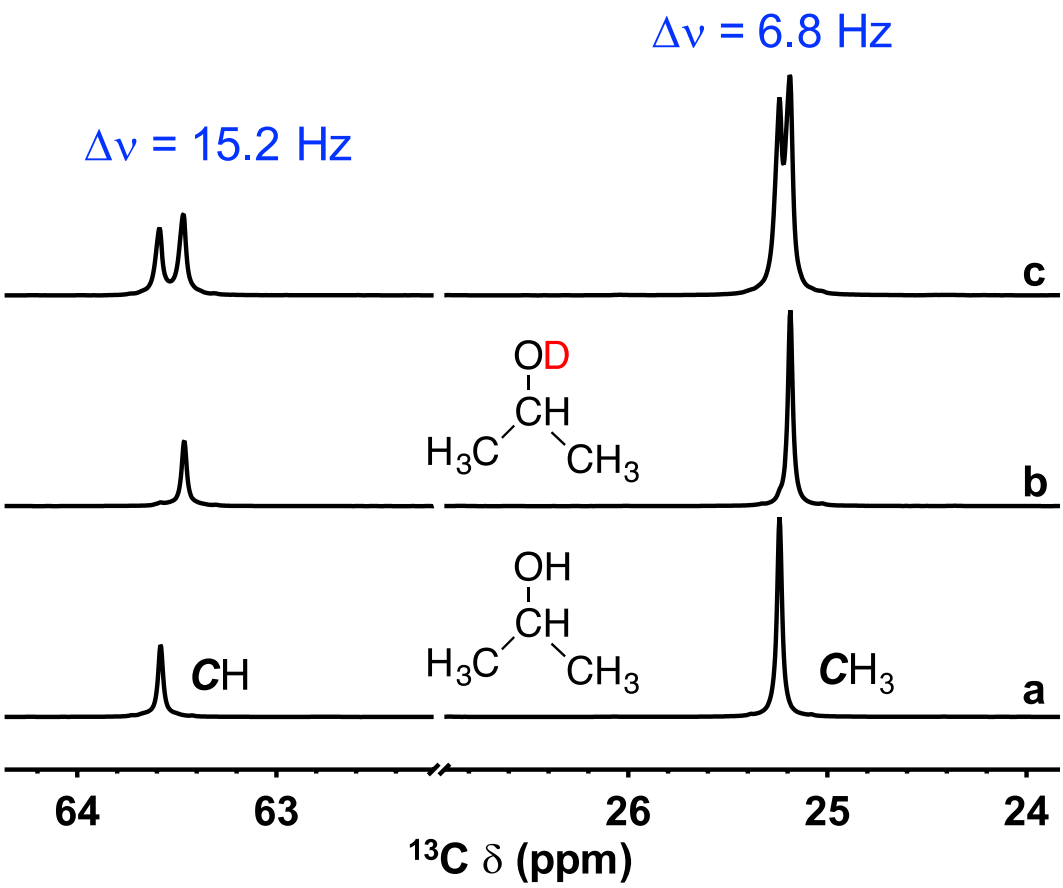

Figure S3.8. Solution-state ^{13}C NMR spectra of (a) 2-PrOH, (b) 2-PrOD-d_1, and (c) an approx. equimolar mixture of 2-PrOH and 2-PrOD-d_1, all recorded at room temperature.

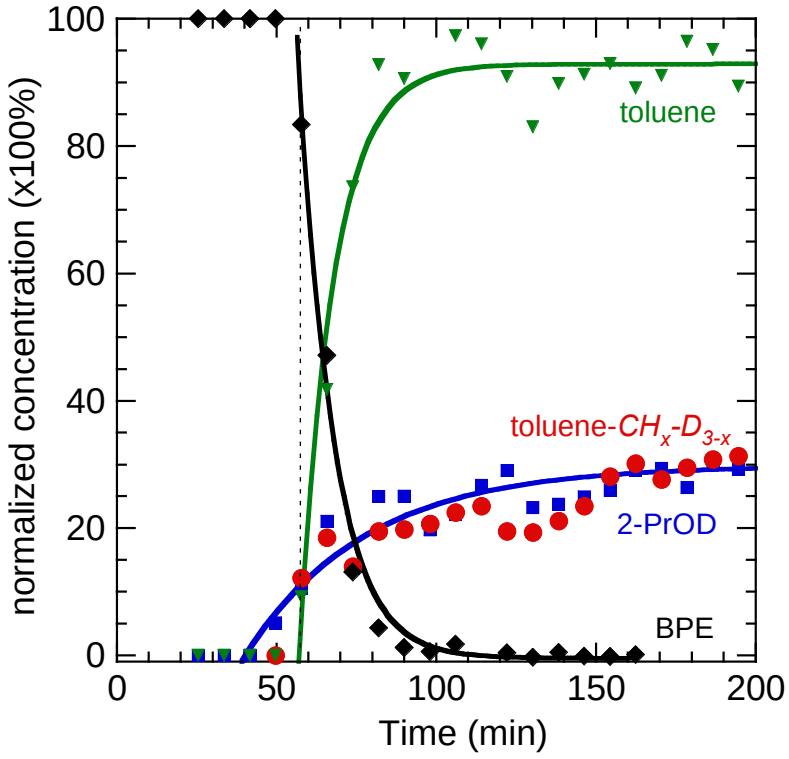

Figure S3.9. Kinetic profiles for the conversion of BPE (2.0 mg, 0.011 mmol) at 175 °C in 2-PrOH (40 µL) with 50 bar D_2 (total internal pressure estimated to be 89 bar at 175 ºC) and air-exposed 2 wt% Ni/γ-Al_2O_3 (10 mg), showing profiles for H/D exchange in the toluene methyl and 2-PrOH hydroxyl groups. The kinetic profiles were extracted from the *operando* ^{13}C MAS-NMR spectra. Each spectrum was acquired with a recycle delay of 60 s at a MAS rate of 5 kHz. The dashed line represents the time at which BPE conversion was first detected.

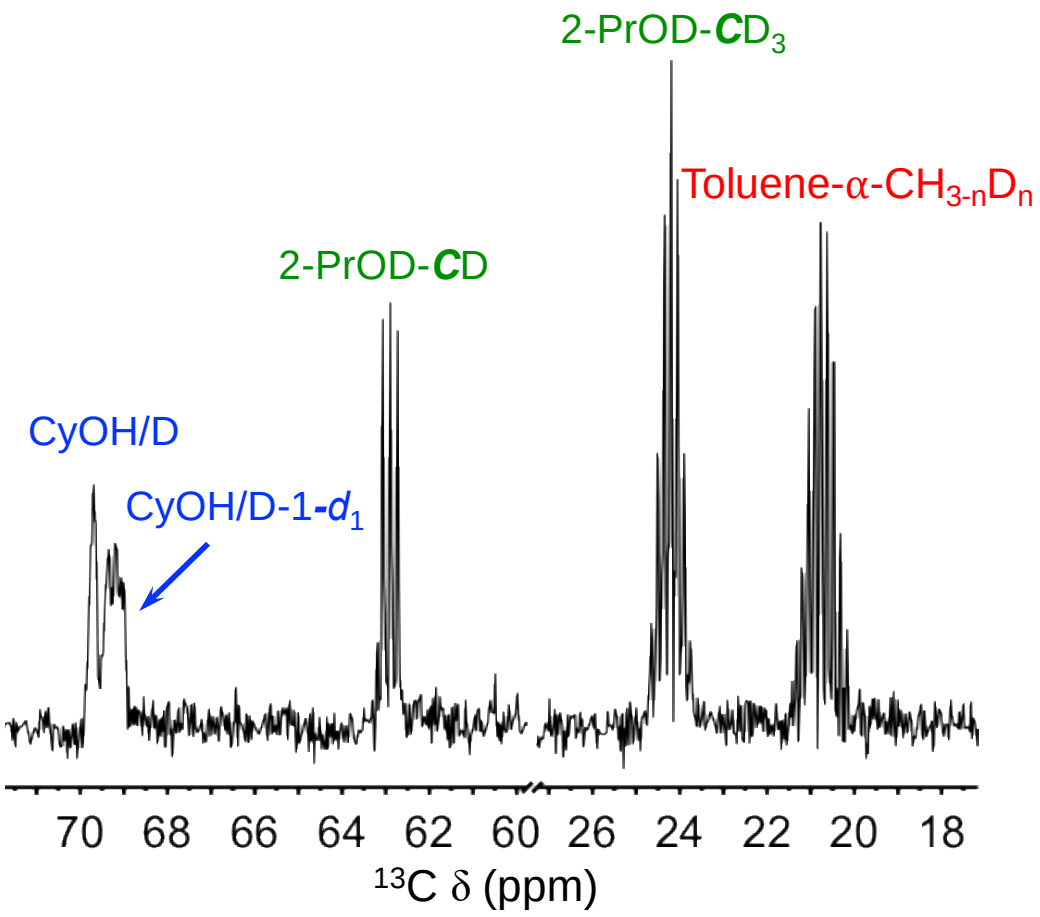

Figure S3.10. ^{13}C MAS-NMR spectra recorded at 25 °C after reaction of ^{13}C-labeled BPE in 2-PrOD-d_8 with 50 bar H_2 (total internal pressure estimated to be 89 bar at 175 ºC) over Ni/γ-Al_2O_3 at 175 °C in a high T/P rotor. Spectra were collected by averaging 16 scans, with a relaxation delay of 60 s. Line broadening of 5 Hz was applied. Cyclohexanol is denoted as CyOH.

Table S3.3. ^{13}C chemical shifts[a] for isotopically-labeled toluenes in 2-PrOD-d_8, extracted from operando MAS-NMR spectra in Figure 3.6a.

Species	Chemical shift (ppm)	
	25 °C	175°C
Toluene-d_0	21.4	20.6
Toluene-d_1	21.1	20.4
Toluene-d_2	20.9	20.1
Toluene-d_3	20.6	19.8

[a] After calibration of the CD_3 signal of 2-PrOD-d_8 at 24.2 ppm[7] at 25 °C. $^1J_{CD}$ values for all species are *ca.* 18 Hz, at both 25 and 175 °C.

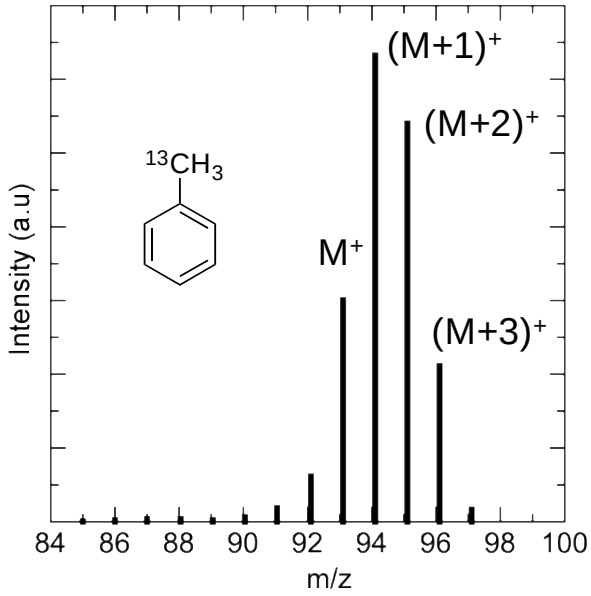

Figure S3.11. Mass spectrum of toluene (m/z = 93 for the molecular ion of toluene-α-$^{13}CH_3$), formed by catalytic hydrogenolysis of ^{13}C-labeled BPE in 2-PrOD-d_8 in the presence of 2 wt% Ni/γ-Al_2O_3 with 50 bar H_2 at 150 °C. The aliquot was sampled after 12 h reaction.

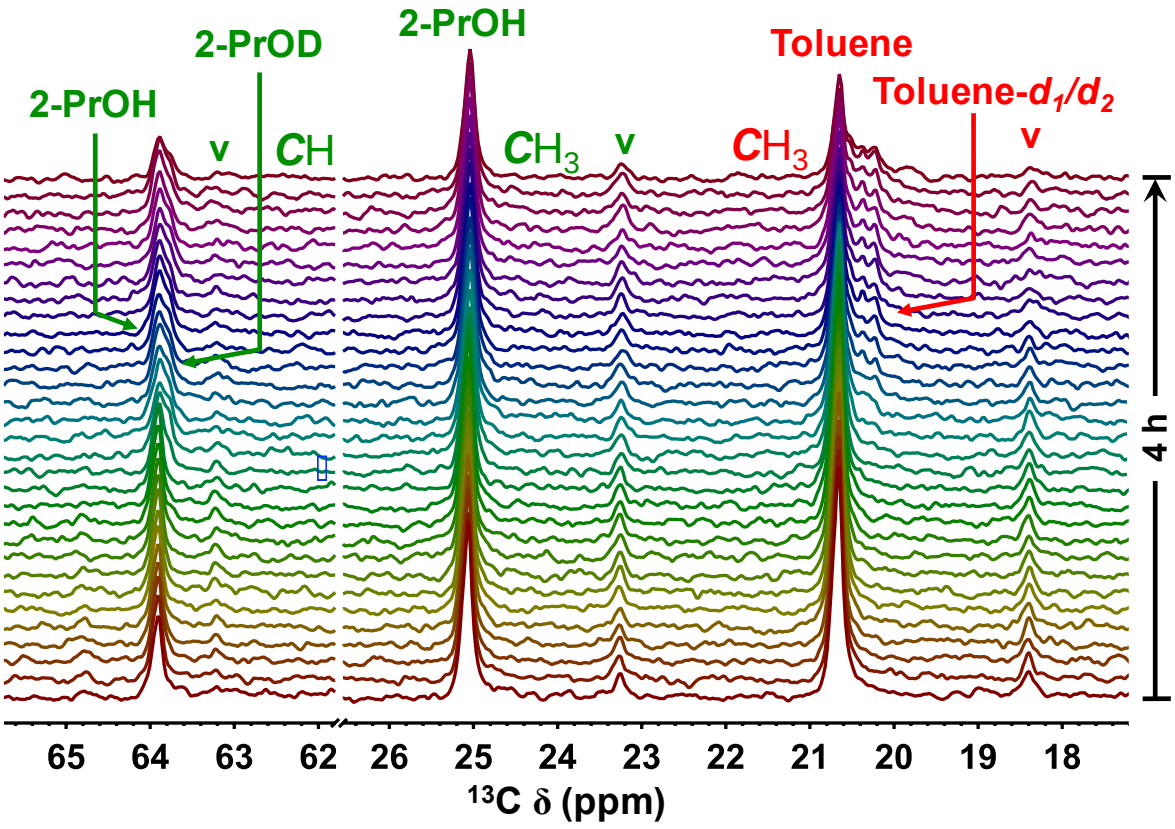

Figure S3.12. *Operando* ^{13}C MAS-NMR spectra of toluene-α-^{13}C (2.0 mg, 0.022 mmol) in 2-PrOH (40 μL, 0.52 mmol) undergoing exchange with 50 bar D_2 (0.20 mmol) catalyzed by air-exposed 2 wt% Ni/γ-Al_2O_3 (10 mg) at 175 °C, showing H/D exchange in the toluene methyl and 2-propanol hydroxyl groups. Total internal pressure estimated to be 89 bar at 175 ºC. ★ denotes the first spectrum at which onset of H/D exchange in 2-PrOH and toluene was detected. Each spectrum was acquired with 8 scans and a recycle delay of 60 s. MAS rate: 5 kHz.

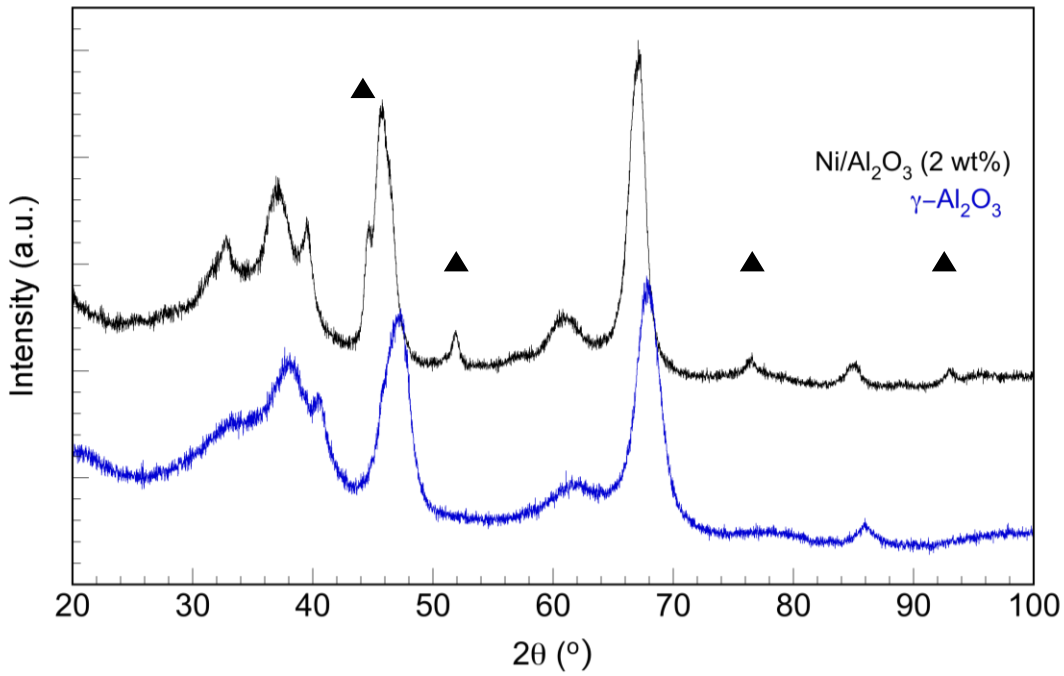

Figure S3.13. Powder X-ray diffraction patterns of Ni/γ-Al_2O_3 (2 wt% Ni), after reduction in H_2 at 850 °C and air-exposure at room temperature (black), as well as the γ-Al_2O_3 support (blue). The locations of the reflections of *fcc*-Ni are indicated by triangles. Slight shifts in the positions of the γ-Al_2O_3 reflections for the reduced catalyst indicate that some (est. ca. 45 %, by TPD) of the Ni^{2+} ions remain associated with the alumina lattice.

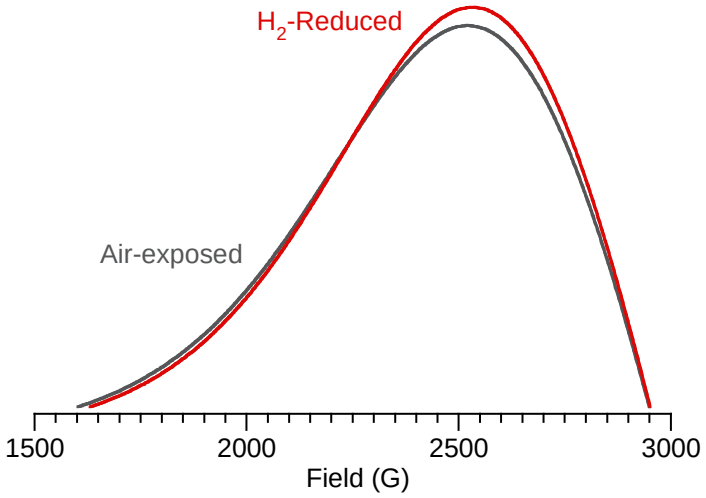

Figure S3.14. A portion of the room temperature EPR spectrum of reduced Ni/γ-Al_2O_3, recorded after 1 h exposure to air at room temperature (gray), and after its re-reduction in flowing H_2 at 170 °C for 30 min, followed by cooling to room temperature (red).

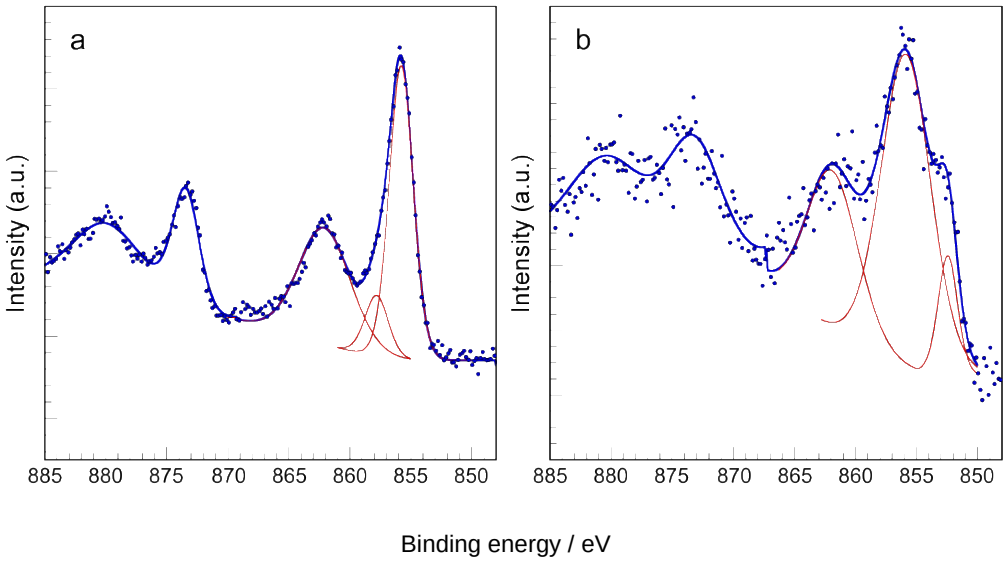

Figure S3.15. High resolution XPS in the Ni 2*p* region, for (a) the calcined catalyst precursor, with both $NiAl_2O_4$ and NiO components, and (b) the H_2-reduced catalyst, with both Ni/γ-Al_2O_3 and NiO/γ-Al_2O_3 components (after air-exposure). The data are represented as blue points; the deconvoluted components are shown as red lines, and the overall fitted spectrum is a blue line. Peak positions and assignments are summarized in Table S3.2.

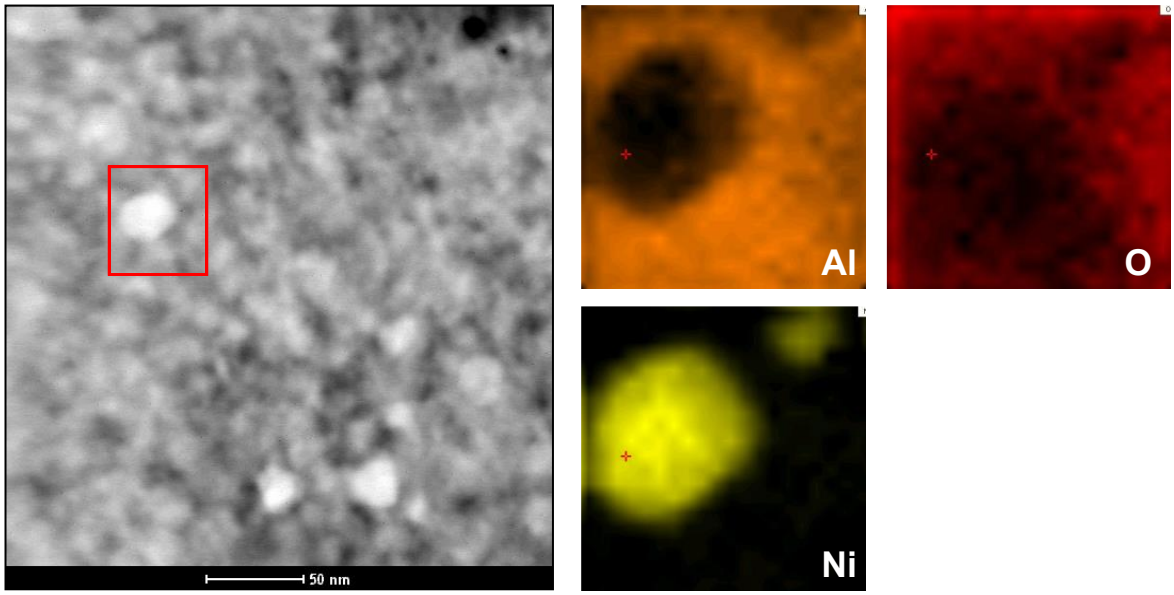

Figure S3.16. High angle annular dark field scanning transmission electron microscopy (HAADF STEM) image of the H_2-reduced catalyst, Ni/Al_2O_3, after air exposure at room temperature. The red square represents the region selected for energy dispersive X-ray (EDX) spectroscopy mapping analysis for the elements Al (orange), Ni (yellow) and O (red). Despite the slight displacement of the image, the O EDX image clearly shows a small amount of oxygen superimposed on the Ni nanoparticle location.

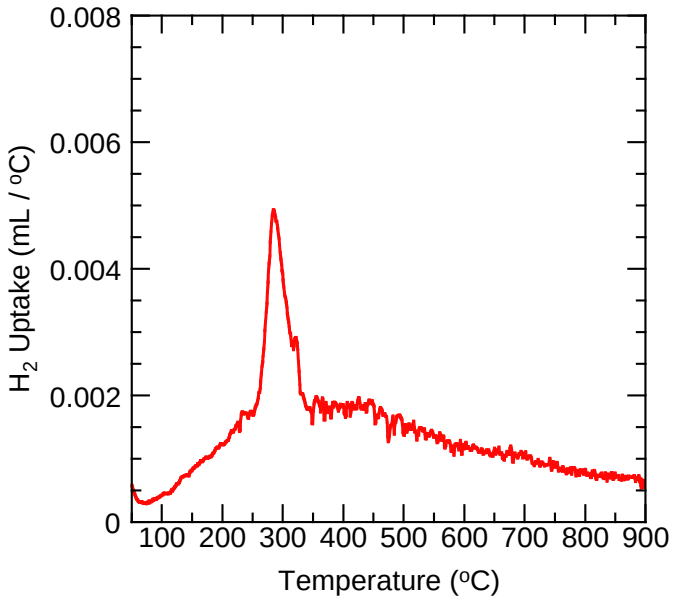

Figure S3.17. Temperature programmed reduction (TPR) of pre-reduced 2 wt% Ni/γ-Al_2O_3 (250 mg), recorded after 6 d exposure to air at room temperature. Integration of the peak centered at 280 ºC yields an area corresponding to ca. 0.12 mL of H_2, which corresponds to reduction of 6.2% of Ni atoms in the sample.

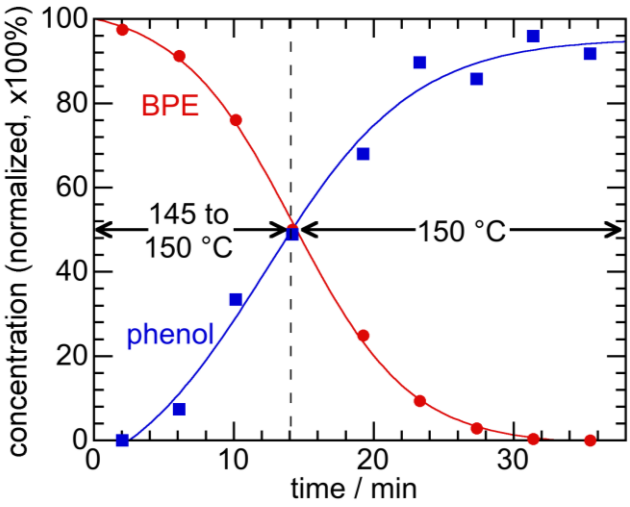

Figure S3.18. Reaction profiles for BPE hydrogenolysis (2.0 mg, 0.011 mmol) in 2-PrOH (40 µL, 0.52 mmol) with 50 bar H_2 (0.20 mmol) catalyzed by H_2-reduced Ni/γ-Al_2O_3 (2 wt% Ni, 10 mg, not air-exposed), measured by *operando* ^{13}C MAS-NMR. Total internal pressure estimated to be 79 bar at 150 ºC. BPE conversion (red circles) and phenol yield (blue squares) were measured while the internal temperature of the NMR rotor rose from ca. 145 °C (time = 0 min) to stabilize at 150 °C (after ca. 14 min). The concentrations of both species were normalized based on the initial intensity of the BPE benzylic resonance (BPE-B). Lines are drawn only to guide the eye.

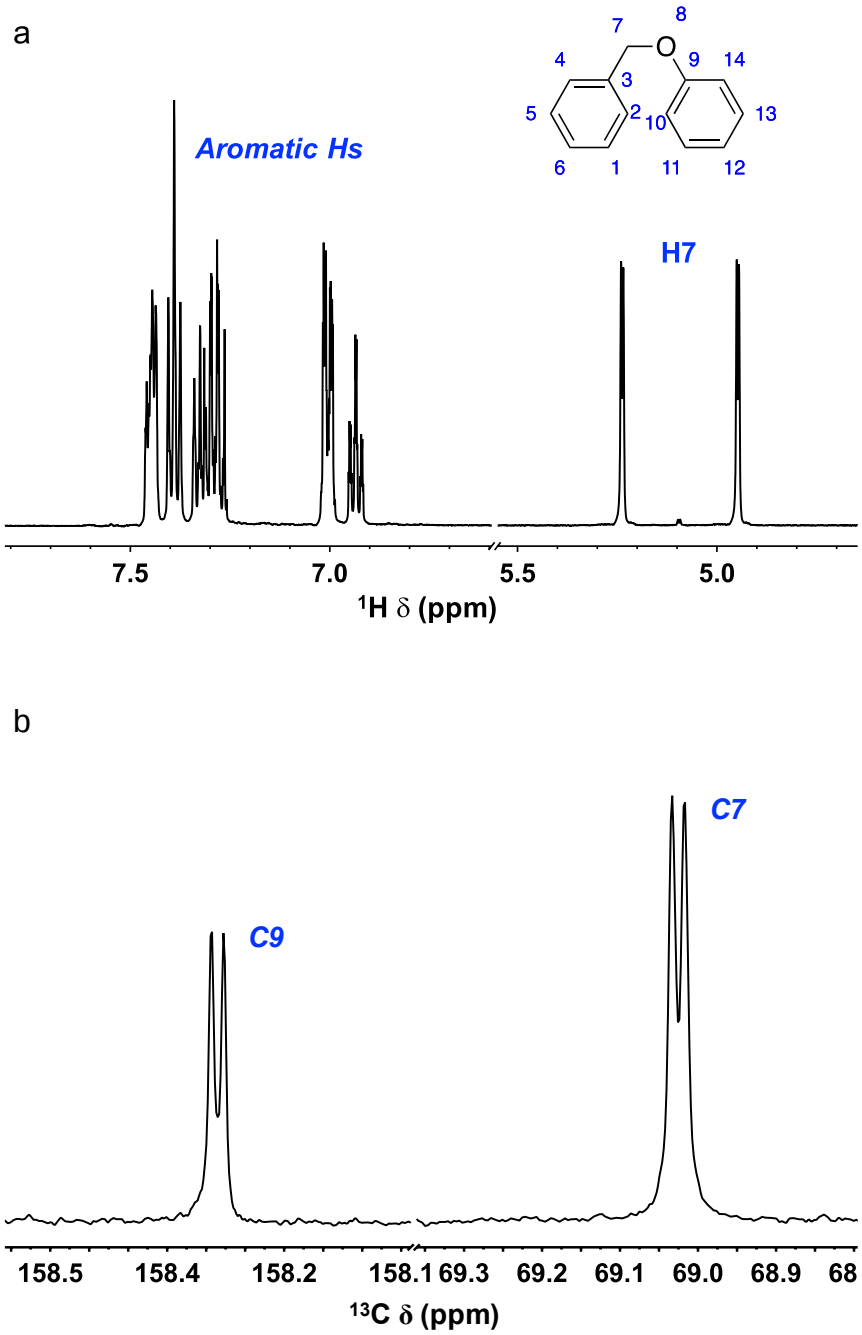

Figure S3.19. Solution-state NMR spectra of BPE (^{13}C-labeled at C7 and C9), recorded in DMSO-d_6 at 23 °C: (a) ^{1}H spectrum, acquired at 500 MHz (recycle delay 20 s, 16 scans), and (b) ^{13}C spectrum, acquired at 125 MHz (recycle delay 60 s, 16 scans).

3.7.2 Additional References

(1) Tada, S.; Yokoyama, M.; Kikuchi, R.; Haneda, T.; Kameyama, H. N_2O Pulse Titration of Ni/α-Al_2O_3 Catalysts: A New Technique Applicable to Nickel Surface-Area Determination of Nickel-Based Catalysts. *J. Phys. Chem. C* **2013**, *117*, 14652.

(2) Wyckoff, R. W. G., Crystal Structures. Interscience Publishers: 1963; Vol. 1.

(3) Legrand, D. L.; Nesbitt, H. W.; Bancroft, G. M. X-ray Photoelectron Spectroscopic Study of a Pristine Millerite (NiS) Surface and the Effect of Air and Water Oxidation. *Am. Mineral.* **1988**, *83*, 1256.

(4) Cheng, Z. X.; Zhao, X. G.; Li, J. L.; Zhu, Q. M. Role of Support in CO_2 Reforming of CH_4 over a Ni/γ-Al_2O_3 Catalyst. *Appl. Catal. A* **2001**, *205*, 31.

(5) Chen, Y.-G.; Ren, J. Conversion of Methane and Carbon Dioxide into Synthesis Gas over Alumina-Supported Nickel Catalysts. Effect of Ni-Al_2O_3 Interactions. *Catal. Lett.* **1994**, *29*, 39.

(6) Mette, K.; Kühl, S.; Tarasov, A.; Willinger, M. G.; Kröhnert, J.; Wrabetz, S.; Trunschke, A.; Scherzer, M.; Girgsdies, F.; Düdder, H.; Kähler, K.; Ortega, K. F.; Muhler, M.; Schlögl, R.; Behrens, M.; Lunkenbein, T. High-Temperature Stable Ni Nanoparticles for the Dry Reforming of Methane. *ACS Catal.* **2016**, *6*, 7238.

(7) Kegley, S. E.; Pinhas, A. R., Problems and Solutions in Organometallic Chemistry. University Science Books: 1986.

Chapter 4: Using Strong Solvent Effects to Direct the Selectivity of Ether Hydrogenolysis Towards Phenolics

4.1 Abstract

The composition of the liquid phase environment can have a profound impact on the rates of hydrogenolysis and hydrogenation reactions, through solvent competition for active sites and solvation of the reactant. The rates of benzyl phenyl ether hydrogenolysis catalyzed by Ni/γ-Al_2O_3 at 448 K are similar in 2-propanol and *n*-decane, but the rate of subsequent phenol hydrogenation is strongly solvent-dependent, being much faster in *n*-decane. The result is a strong solvent-dependence of the reaction selectivity (to toluene and phenol in 2-propanol, vs. toluene and cyclohexanol in *n*-decane). The solvent dependence of the phenol hydrogenation rate was measured independently in a wide range of protic and aprotic solvents, leading to a variation of two orders of magnitude. However, the rate is not a simple function of solvent polarity. Instead, the rate is linearly correlated with the extent of phenol adsorption. The slope and intercept of the linear correlation differ for protic vs. aprotic solvents. In protic solvents, adsorption is suppressed by hydrogen bonding interactions which stabilize phenol in solution. In aprotic solvents, competitive adsorption of the solvent on the Ni active sites suppresses adsorption. Consequently, the rate of phenol hydrogenation is fastest in protic solvents that are weak hydrogen-bond donors, or aprotic solvents that adsorb weakly on the metal. Selectivity in ether hydrogenolysis can be tuned by solvent selection without compromising catalytic activity.

4.2 Introduction

Lignocellulosic biomass is the largest natural source of aromatics, making it a promising source of renewable arenes and phenolics. The production of fine chemicals from lignocellulosic biomass, and in particular the lignin fraction, using a heterogeneous catalyst commonly requires the presence of a solvent, which may influence the activity and selectivity of the chemical transformation at the solid–liquid interface. Solvation of reactants, intermediates, and transition states, in solution as well as on the surface, affects activity and selectivity.[1,2] The investigation of adsorption and reaction at solid-liquid interfaces is challenging, particularly under conditions involving elevated temperatures and pressures.[3]

Much work has been done exploring solvent effects in enzymatic and homogeneous catalysis,[4,5] however reports of such phenomena in heterogeneous systems are sparse. Although there are several examples with good correlations between hydrogenation rates and solvent parameters such as polarity or other empirical parameters,[6–9] the interpretation was generally incomplete. For example, the hydrogenation of acetophenone over a Rh/Al_2O_3 catalyst in 13 different solvents at 353 K showed higher conversion in water or nonpolar solvents than in polar solvents, suggesting the hydrogenation of acetophenone was enhanced by solvation.[10] In a separate study on the solvent effects on the hydrogenation of 2-butanone in 10 different solvents, a strong influence of the solvent polarity on the rate of hydrogenation was shown.[11] A correlation between hydrogenation of 2-butanone and hydrogen-bond donating ability of the solvents was observed, and it was suggested that the hydrogen bonding lowers the activation energy barrier and leads to high hydrogenation rates. For the polar aprotic solvents, it was suggested that the solvent could strongly adsorb

onto the catalyst surface and block the Ru active sites leading to an inhibition of the hydrogenation, however no adsorption measurements were provided. A more rigorous investigation into the origin of these solvent effects is needed to predict the activity and selectivity of the hydrogenolysis and hydrogenation reactions useful in lignin valorization.

Previously, sealed high-pressure and -temperature solid state NMR rotors were used to study the hydrogenolysis of ^{13}C-labeled benzyl phenyl ether (BPE) in 2-propanol.[12] The hydrogenolysis was initiated after a short induction period (corresponding to catalyst activation by reduction of the surface oxide on Ni), to give toluene and phenol (PhOH) as the major products, Scheme 1.[13] No hydrogenation of either BPE or toluene was observed, although some toluene hydrogenation was reported previously even under severe reaction conditions (498 K, 120 bar H_2).[14] However, PhOH is slowly hydrogenated at temperatures above 423 K.

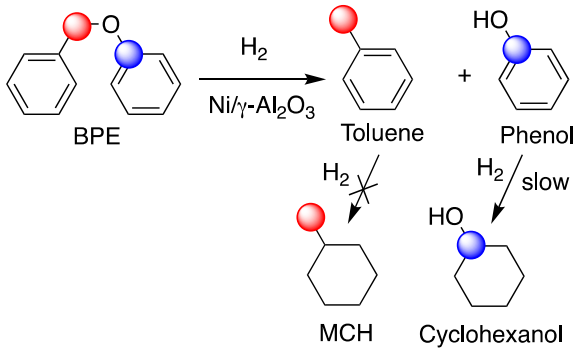

Scheme 1. Hydrogenolysis of benzyl phenyl ether (BPE), selectively ^{13}C-labeled at the benzylic (Red, BPE-B) and phenolate-1-C (Blue, BPE-P) positions, results in toluene-α-^{13}C and phenol-1-^{13}C. Slow, subsequent hydrogenation of phenol-1-^{13}C to cyclohexanol-1-^{13}C occurs without accompanying toluene hydrogenation to methylcyclohexane (MCH).

In the present study, solvent effects on the hydrogenolysis of BPE and hydrogenation of PhOH are investigated. The rates of PhOH hydrogenation are strongly dependent on the

extent of phenol adsorption on the catalyst surface, implicating the balance between phenol solvation and competitive adsorption. Detailed kinetic analysis and a Langmuir Hinshelwood model were used to extract rate and equilibrium constants for PhOH hydrogenation in a wide range of protic and aprotic solvents. PhOH adsorption experiments onto the Ni/γ-Al_2O_3 catalyst showed a strong correlation between rates of hydrogenation and equilibrium adsorption constants.

4.3 Results and discussion

4.3.1 Solvent Effect on the Rate and Selectivity of Benzyl Phenyl Ether Hydrogenolysis

To provide a basis for understanding solvent effects on catalytic lignin depolymerization, the kinetics of Ni-catalyzed hydrogenolysis of a model ether, BPE, were compared in 2-propanol and *n*-decane. The former solvent was used extensively in our previous study of BPE hydrogenolysis,[13,14] while nonpolar aprotic solvents such as *n*-heptane, methylcyclohexane, and decalin were reported to enhance the rate of Ni-catalyzed diphenyl ether hydrogenolysis relative to polar protic solvents such as methanol, ethanol, and *t*-butanol.[15]

The ^{13}C resonances for doubly-^{13}C-labeled BPE (at the phenyl and benzyl positions, 159.3 and 70.1 ppm, respectively), toluene-α-^{13}C (20.8 ppm), phenol-1-$^{13}C_1$ (157.8 ppm), and cyclohexanol-1-$^{13}C_1$ (69.7 ppm) are all clearly resolved in the *operando* MAS NMR spectra shown in Figure 1. In both solvents, the BPE signals disappear rapidly, as signals for the primary reaction products toluene and PhOH grow in. The toluene signal stabilizes at longer times, with no evidence for its hydrogenation to methylcyclohexane under these reaction conditions. However, the PhOH signal passes through a maximum then starts to

decline at longer times as PhOH is slowly hydrogenated to cyclohexanol. Integration of the signals gave the kinetic profiles shown in Figure 4.2. In both solvents, hydrogenolysis of BPE is complete in ca. 10 min at 448 K, Figure S4.1. Subsequent PhOH hydrogenation to cyclohexanol is much faster in the non-polar solvent. In both solvents, the total mass balance decreases abruptly in the first few minutes, then is gradually restored, Figure S4.2.

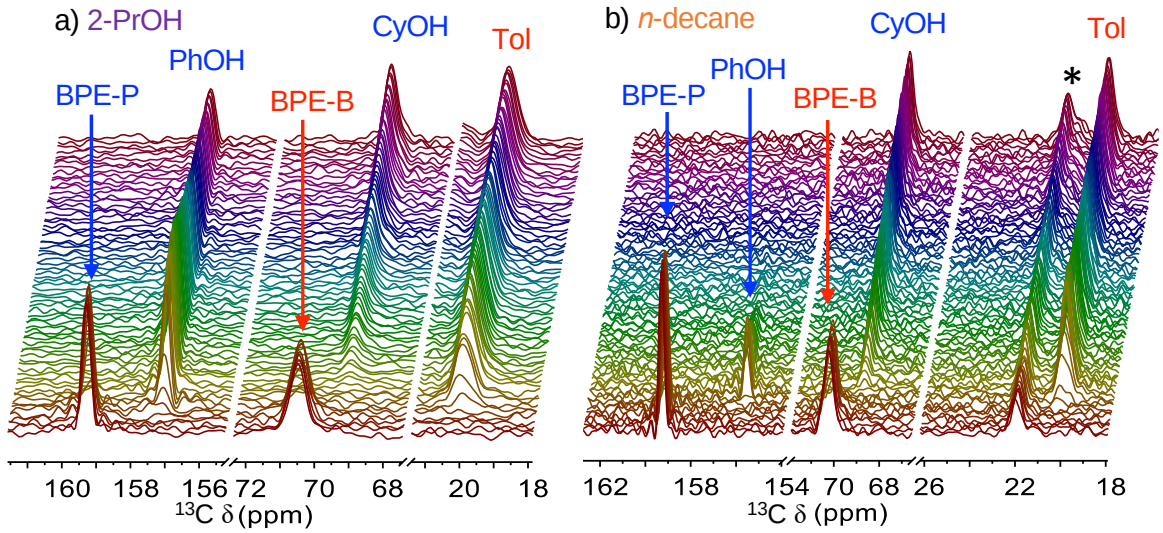

Figure 4.1. *Operando* array of direct polarization ^{13}C MAS NMR spectra, recorded during BPE hydrogenolysis at 448 K, in (a) 2-propanol, or (b) *n*-decane. The two ^{13}C-labeled positions of BPE are indicated as BPE-B (benzylic) and BPE-P (phenolic). The spectra show BPE conversion to toluene-α-^{13}C (Tol) and phenol-1-^{13}C (PhOH), as well as the subsequent hydrogenation of phenol-1-^{13}C to cyclohexanol-1-^{13}C (CyOH). The NMR rotor was initially loaded with 2 wt% Ni/γ-Al_2O_3 (30 mg, air exposed), BPE (6.0 mg, 0.033 mmol), 2-propanol (120 μL, 1.56 mmol) or *n*-decane (120 μL, 0.60 mmol), and pressurized with 50 bar H_2 at room temperature (0.60 mmol). MAS rate: 3 kHz. * denotes a solvent peak.

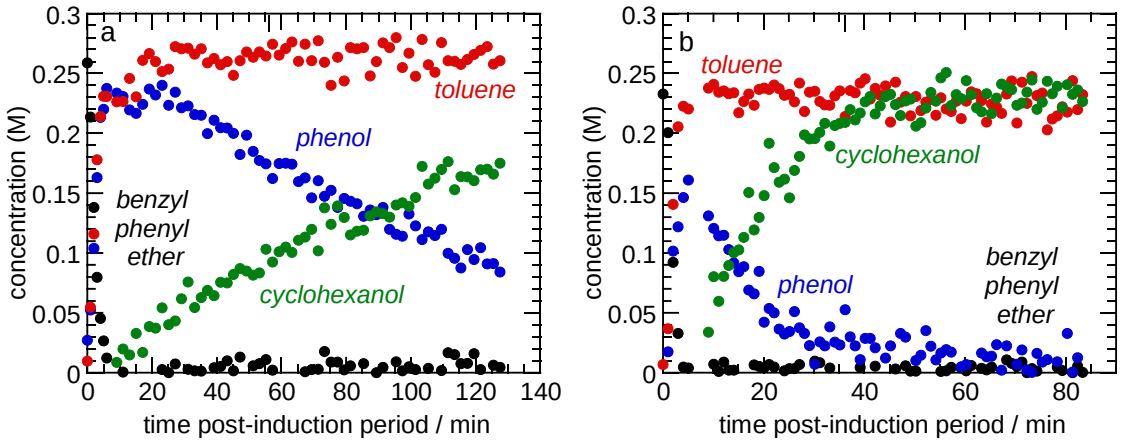

Figure 4.2. Kinetic profiles obtained by integrating signals in the *operando* ^{13}C MAS NMR spectra during hydrogenolysis of BPE (0.33 mmol) catalyzed by Ni/γ-Al_2O_3 (30 mg, 2 wt% Ni) at 448 K with 50 bar H_2, in either (a) 2-propanol, or (b) *n*-decane as solvent (120 mL). Since the catalyst was air-exposed prior to use, all profiles had a short induction period (ca. 5 min, not shown), attributed to reduction of the surface oxide.

4.3.2 Solvent Effect on Phenol Hydrogenation

To explore the origin of the change in selectivity caused by the choice of a polar vs. non-polar solvent, the kinetics of PhOH hydrogenation were explored directly. In addition to 2-propanol and *n*-decane, a wide range of other solvents was also used, including various aromatics (anisole, benzene, toluene, *p*-xylene, pyridine), alcohols (1-decanol, *t*-butanol, 1-butanol, ethanol, methanol, ethylene glycol), and water. Their polarities vary widely, as reflected in dielectric constants that range from 2 (*n*-decane) to 80 (water),[16] Table 1. In each solvent (with the exception of pyridine), PhOH is fully converted to CyOH as the sole product, with no NMR-detectable intermediates. However, the solvent effect on the rate is very large. For example, the reaction goes to completion ca. 50 times faster in *n*-decane than

in ethylene glycol, Figure 4.3. No reaction was observed in pyridine, presumably due to its very strong adsorption on the catalyst surface, blocking the active sites.

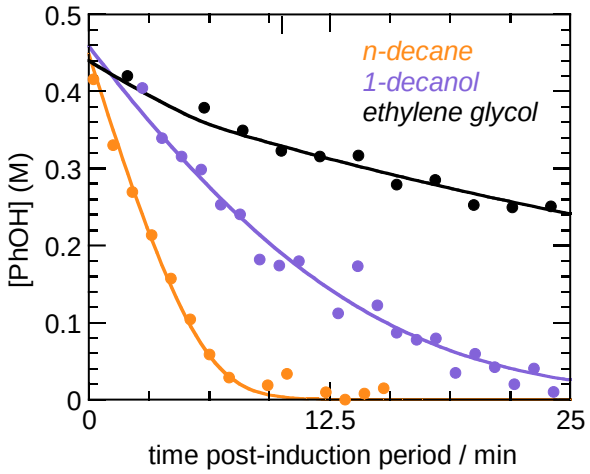

Figure 4.3. Comparison of PhOH hydrogenation profiles in *n*-decane, 1-decanol, and ethylene glycol during the reaction of PhOH (0.64 mmol) with H_2 (50 bar) catalyzed by Ni/γ-Al_2O_3 (30 mg, 2 wt% Ni) at 473 K in the indicated solvent (120 mL). Solid lines represent curvefits using eq. 4.9.

Kinetic profiles were obtained by integrating PhOH resonances in the *operando* ^{13}C MAS NMR spectra, shown in Figure 4.4. Since the catalyst was air-exposed prior to use, the profiles in all solvents showed a short induction period (ca. 5 min), attributed to reduction of the surface oxide on Ni (full kinetic profiles shown in Figure S4.3.) Among the alcohol solvents, PhOH hydrogenation proceeds fastest in *t*-butanol, and slowest in methanol. The reaction is generally faster in less polar alcohols, although the reactions in both of the straight-chain alcohols (1-decanol and 1-butanol) are slower than expected based on their polarity,[17] and have nearly identical kinetic profiles to the reaction in 2-propanol. For the aprotic solvents, a similar trend is observed: reactions in less polar solvents are generally

faster. In addition, the rates in aromatic solvents increase as the number of methyl groups on the benzene ring increases.

Table 4.1. Comparison of solvent effects on the rate parameters[a] for PhOH hydrogenation catalyzed by Ni/γ-Al_2O_3 at 473 K

Solvent	Dielectric constant (ε)	k'_{PhOH} ($M\ s^{-1}$)	K'_{PhOH} (M^{-1})	$k'_{obs,PhOH}$[b] (s^{-1})	K'_{cat}[c] (M^{-1})
n-decane	1.99	6.0(2.3)	8.8(10.)	53(25)	9.0
p-xylene	2.27	5.1(1.6)	3.7(2.2)	19(3.0)	4.3
benzene	2.28	4.7(2.3)	1.7(1.2)	8.1(3.0)	3.1
toluene	2.38	4.6(1.6)	2.8(1.6)	13(3.0)	3.5
anisole	4.30	5.2(3.5)	1.2(1.0)	5.9(4.0)	2.7
pyridine	13.2	-[d]	-[d]	-[d]	1.4
1-decanol	7.93	3.4(1.5)	2.9(2.3)	10(3.0)	0.83
t-butanol	12.5	4.1(1.0)	5.2(2.9)	21(3.0)	1.0
1-butanol	17.8	4.1(9.0)	2.4(9.0)	9.8(0.9)	0.71
2-propanol	20.2	4.3(4.1)	2.6(4.2)	11(18)	0.88
ethanol	25.3	5.4(7.4)	0.70(1.1)	3.8(0.8)	0.49
methanol	33.3	4.3[e]	0.12(1)	0.51(2)	0.093
ethylene glycol	41.4	4.3[e]	0.31(1)	1.3(1)	0.19
water	80.1	4.8(2.8)	2.0(1.8)	9.7(5.0)	0.88

[a] Rate and equilibrium constants are extracted from the kinetic profiles during PhOH (0.64 mmol) hydrogenation with H_2 (50 bar) catalyzed by Ni/γ-Al_2O_3 (30 mg, 2 wt% Ni) at 473 K in the indicated solvent (120 mL). Values in parentheses represent 95% confidence intervals from the curve fit. [b] The rate constant $k'_{obs,PhOH}$ is the product of rate constant k'_{PhOH} and equilibrium constant K'_{PhOH}. [c] The equilibrium constant K'_{cat} is defined in Eq S4.11. [d] No reaction was observed in pyridine. [e] Values for methanol and ethylene glycol produced significantly larger confidence intervals because the profiles are close to being simple exponentials, therefore k'_{PhOH} values were fixed at 4.7 $M\ s^{-1}$ (average value for all other solvents).

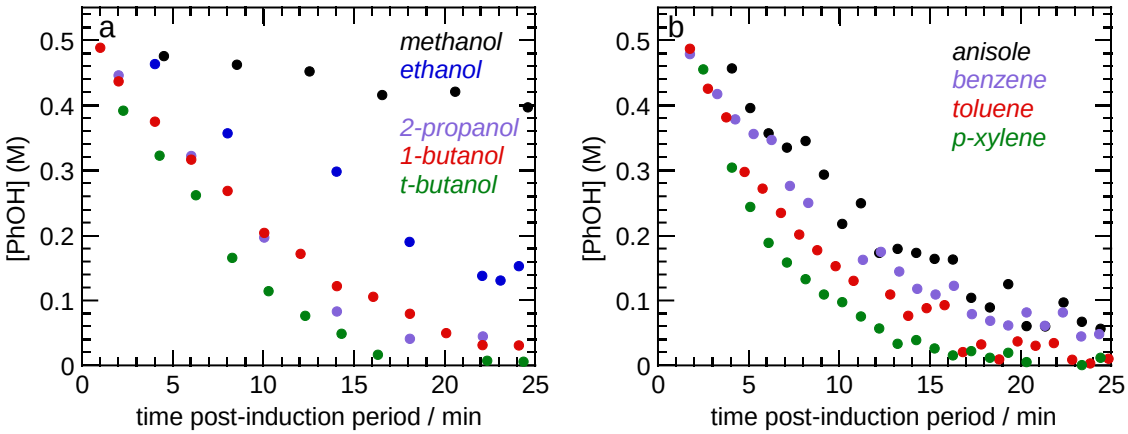

Figure 4.4. Solvent dependence of the kinetic profiles for PhOH hydrogenation obtained by integrating signals in the *operando* ^{13}C MAS NMR spectra, during the reaction of PhOH (0.64 mmol) with H_2 (50 bar) catalyzed by Ni/γ-Al_2O_3 (30 mg, 2 wt% Ni) at 473 K in the specified solvent (120 mL), which is either (a) protic, or (b) aprotic. Since the catalyst was air-exposed prior to use, all profiles had a short induction period (ca. 5 min), attributed to reduction of the surface Ni oxide. Full kinetic profiles are shown in Figure S4.3.

4.3.3 Kinetic Model for Phenol Hydrogenation

In the majority of solvents (methanol and ethylene glycol being exceptions), the kinetic profiles for PhOH hydrogenation are not well-described by a pseudo-first-order rate law, Figure S4.4. Instead, a simple Langmuir-Hinshelwood model was used, eqs 4.1-4.3.

$$H_2 + 2\,Solv* \rightleftarrows 2H* \qquad K_H \qquad (4.1)$$

$$PhOH + Solv* \rightleftarrows PhOH* + Solv \qquad K_{PhOH} \qquad (4.2)$$

$$PhOH* + 6H* + Solv \rightarrow CyOH + Solv* \qquad k_{PhOH} \qquad (4.3)$$

where * represents an adsorption site. Eq 4.1 is the dissociative chemisorption of H_2 on active sites covered by solvent (Solv). Eq 4.2 describes the adsorption of the PhOH on the

active sites, also by displacing adsorbed solvent molecules. Eq 4.3 shows the reaction between adsorbed PhOH and atomic H. This step is not elementary, but since no partially hydrogenated intermediates are observed, it is represented by a single kinetic equation.

The rate-determining step is eq 4.3 since eq 4.1-4.2 are assumed to be quasi-equilibrated. The rate of PhOH consumption is given by eq 4.4:

$$-\frac{dn_{PhOH}}{dt} = k_{PhOH}\theta_{PhOH}\theta_H n_{Ni} \tag{4.4}$$

where n_{Ni} is the number of moles of Ni active sites. Assuming there are no unoccupied active sites in the liquid phase, the site balance is:

$$\theta_{Solv} + \theta_H + \theta_{PhOH} = 1 \tag{4.5}$$

where θ_i is the fractional surface coverage of species *i*. H_2 is present in excess (5× on a molar basis). Furthermore, experiments conducted with higher P(H_2) resulted in no significant differences in rate (Figure S4.5). Therefore H_2 chemisorption is not competitive with PhOH adsorption, implying that θ_H is constant. Thus the site balance simplifies to eq 4.6, with the surface coverage of PhOH given by eq 4.7:

$$\theta_{Solv} + \theta_{PhOH} = 1 \tag{4.6}$$

$$\theta_{PhOH} = \frac{K_{PhOH}C_{PhOH}}{C_{Solv} + K_{PhOH}C_{PhOH}} \tag{4.7}$$

where C_i is the solution concentration of species *i*. The rate of PhOH hydrogenation is shown in eq 4.8:

$$-\frac{dn_{PhOH}}{dt} = k_{PhOH}\left(\frac{K_{PhOH}C_{PhOH}}{C_{Solv} + K_{PhOH}C_{PhOH}}\right)\theta_H n_{Ni} \tag{4.8}$$

Since the rate has dimensions [mol s^{-1}], and K_{PhOH} is a dimensionless equilibrium constant, k_{PhOH} is a "first-order" rate constant with dimensions [s^{-1}]. Eq 4.8 can be rewritten in a form more convenient for curvefitting:

$$-\frac{dC_{PhOH}}{dt} = \frac{k_{PhOH}}{V}\left(\frac{K'_{PhOH}C_{PhOH}}{1+K'_{PhOH}C_{PhOH}}\right)\theta_H n_{Ni} = \frac{k'_{PhOH}K'_{PhOH}C_{PhOH}}{(1+K'_{PhOH}C_{PhOH})} \qquad (4.9)$$

where $\frac{K'_{PhOH}=K_{PhOH}}{C_{Solv}}$, and V is the liquid volume under reaction conditions. Here, the composite rate constant $\frac{k'_{PhOH}=k_{PhOH}\theta_H n_{Ni}}{V}$ is a "pseudo-zeroth-order" rate constant with dimensions [M s^{-1}], and K'_{PhOH} is a conditional equilibrium constant with dimensions [M^{-1}].

Since the solvents used in these experiments vaporize partially under the reaction conditions (473 K), the fraction of liquid present in the rotor (volume 450 µL) was estimated by comparing the areas of the NMR resonances for the vapor phase and liquid phase, Table S4.1. For solvents with a vapor fraction less than ca. 5 %, this method was not very accurate. Therefore values were also estimated using the Antoine equation and the vapor pressure of each solvent.[18,19] The liquid fractions calculated using both methods are in good agreement. PhOH was assumed to be non-volatile; there is no NMR evidence for it in the vapor phase under the reaction conditions. PhOH concentrations were calculated using the liquid solvent fraction and the thermal expansion of the solvent, Table S4.1.

Each kinetic profile was analyzed by non-linear least-squares curvefitting using eq 4.9, with two variable parameters (k'_{PhOH} and K'_{PhOH}). The results are shown in Table 4.1. The rate constant k'_{PhOH} is remarkably similar across 11 solvents (excluding methanol and ethylene glycol). Across this group of solvents, the value varies by less than a factor of two, from 3.4 s^{-1} in 1-decanol to 6.0 s^{-1} in *n*-decane, with an average value of (4.7 ± 0.8) s^{-1}.

Attempts to fit the kinetic profiles in methanol and ethylene glycol resulted in large uncertainties for both k'_{PhOH} and K'_{PhOH}, Table S4.2.

For solvents with small values of K'_{PhOH}, eq 9 simplifies to a simple, pseudo-first-order kinetic equation:

$$-\frac{dC_{PhOH}}{dt} = \frac{k'_{PhOH}K'_{PhOH}C_{PhOH}}{(1+K'_{PhOH}C_{PhOH})} \approx k'_{PhOH}K'_{PhOH}C_{PhOH} = k_{obs,PhOH}C_{PhOH} \quad (4.10)$$

In the case of methanol and ethylene glycol, the kinetic data is well-described by eq 4.10, giving $k_{obs,PhOH}$ values of 0.49(1) and 1.3(1) s^{-1}, respectively, Table S4.3. Assuming k'_{PhOH} = 4.7 s^{-1} in these solvents as well, the corresponding values of K'_{PhOH} are 0.10 M^{-1} and 0.28 M^{-1}, respectively. With $C_{PhOH,0}$ = 0.47 M, the maximum values of $K'_{PhOH}C_{PhOH,}$ are 0.047 and 0.13, respectively, justifying the pseudo-first-order simplification in eq 4.10. In comparison, using eq 4.9 with a fixed k'_{PhOH} value yields $k'_{obs,PhOH}$ values of 0.51(2) and 1.3(1) s^{-1} for methanol and ethylene glycol, respectively, which are identical to the values extracted from the pseudo-first order fit.

In contrast to the insensitivity of k'_{PhOH} to the nature of the solvent, values of K'_{PhOH} are highly solvent-dependent. They vary by nearly two orders of magnitude, from 0.12 M^{-1} in methanol up to 8.8 M^{-1} in *n*-decane. The large variation in PhOH hydrogenation rates in different solvents is therefore a direct result of the sensitivity of K'_{PhOH}. In order to compare rate parameters in all solvents, we compute $k'_{obs,PhOH}$ values corresponding to reaction conditions where K'_{PhOH} and/or C_{PhOH} are small, so that $K'_{PhOH}C_{PhOH} << 1$. In general, less polar solvents (Figure 4.5) or solvents with smaller dielectric constants (Figure S4.6) show larger $k'_{obs,PhOH}$ values (Table 4.1), presumably reflecting stronger PhOH adsorption. However, polarity is clearly not the only factor responsible for determining the rate: the protic and aprotic solvents belong to different groups.

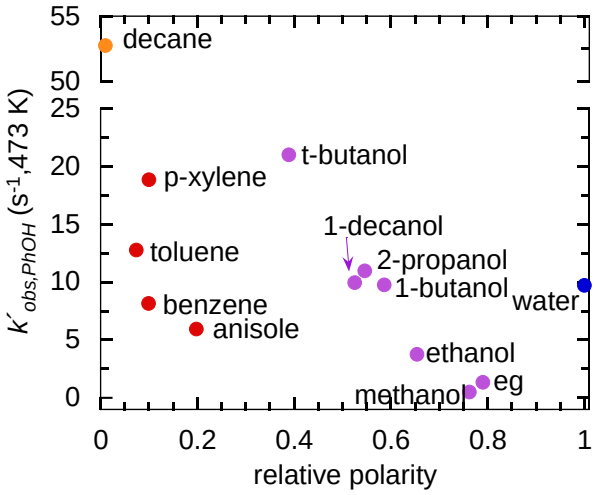

Figure 4.5. Variation of the apparent rate constant $k'_{obs,PhOH}$ with solvent relative polarity for aromatics (red), alcohols (purple), *n*-decane (orange) and water (blue). Rate parameters were obtained from curvefits of kinetic profiles for PhOH (0.64 mmol) hydrogenation with H_2 (50 bar) catalyzed by Ni/γ-Al_2O_3 (30 mg, 2 wt% Ni) at 473 K in the indicated solvent (120 mL).

To further examine the origin of the large solvent dependence of K'_{PhOH} values, PhOH hydrogenation catalyzed by Ni/γ-Al_2O_3 was studied as a function of temperature in *n*-decane and 2-propanol with 50 bar H_2. In the aprotic solvent at 448 K, the reaction goes to completion in ca. 25 min, but requires ca. 100 min in 2-propanol, Figure 4.6. Additional experiments were conducted at 463 K. The rate constants and adsorption constants obtained using eq 4.9 are shown in Table 4.2. The solvent dependence of the rate constant k'_{PhOH} decreases with increasing temperature. The adsorption constants are very similar in both solvents at 448 K, but appear to diverge as the temperature increases. Consequently, the ratio of $k'_{obs,PhOH}$ values is fairly constant over this temperature range.

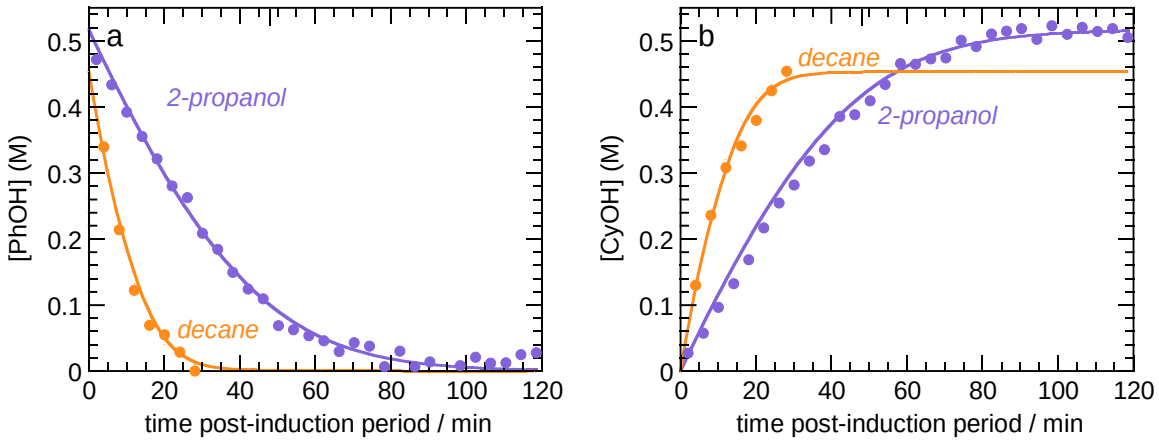

Figure 4.6. Kinetic analyses of ^{13}C NMR profiles for (a) PhOH, and (b) cyclohexanol, recorded simultaneously during hydrogenation of PhOH-1-^{13}C (0.02 mmol) catalyzed by air-exposed Ni/γ-Al_2O_3 (2 wt%) at 448 K with 50 bar H_2 in *n*-decane or 2-propanol (40 μL). The data collected during the short (<5 min) induction period were removed prior to curvefitting using eq 4.9.

Table 4.2. Temperature dependence of rate parameters[a] for PhOH hydrogenation catalyzed by Ni/γ-Al_2O_3[b]

T (K)	k'_{PhOH} ($M\ s^{-1}$)		K'_{PhOH} (M^{-1})		$k'_{obs,PhOH}$ (s^{-1})		Ratio of $k'_{obs,PhOH}$ values
	n-decane	2-PrOH	*n*-decane	2-PrOH	*n*-decane	2-PrOH	
448	3.5 (2.0)	1.2 (3)	3.1 (3.2)	3.0 (1.3)	11 (7)	3.6 (4)	3.0
463	4.1 (7)	2.7 (1.6)	11 (6)	3.2 (3.3)	42 (1)	8.4 (5.3)	5.0
473	6.0 (1.7)	4.3 (4.1)	8.8 (9.2)	2.6 (4.2)	53 (25)	11 (18)	4.8

[a] Values in parentheses represent 95% confidence intervals obtained by curvefitting eq 4.9 to the data. [b] Reaction conditions: PhOH (6.0 mg, 0.063 mmol), Ni/γ-Al_2O_3 (2 wt% Ni, 30.0 mg), 120 μL solvent, 50 bar H_2.

The rate constants k'_{PhOH} were used to construct the Eyring plots in Figure 4.7a. The apparent enthalpies and entropies of activation are shown in Table 4.3. In 2-propanol, the value of $\Delta H^{\ddagger}$, 86 kJ mol^{-1}, is much larger than the corresponding value in *n*-decane, 39 kJ mol^{-1}. In 2-propanol, the value of $\Delta S^{\ddagger}$, 120 J K^{-1} mol^{-1}, is also much larger than the corresponding value in *n*-decane, 22 kJ mol^{-1}. Adsorbed phenol may engage in H-bonding with adsorbed or near-surface 2-propanol, requiring considerably more disruption of these interactions and reorganization of molecules in the transition state compared to the reaction taking place in *n*-decane.

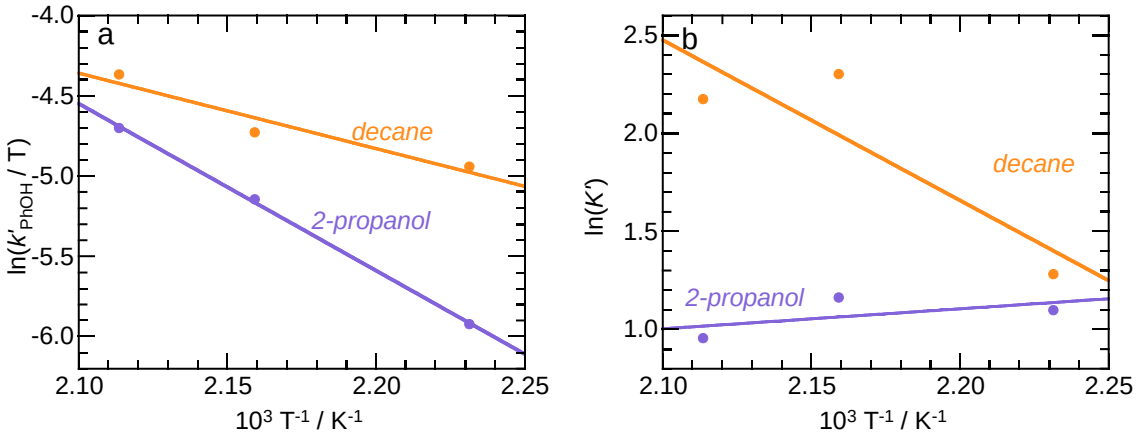

Figure 4.7. (a) Eyring plots of solvent-dependent rate constants $k´_{PhOH}$, and (b) van't Hoff plots of solvent-dependent adsorption constants $K´_{PhOH}$, for PhOH hydrogenation in *n*-decane and 2-propanol at various temperatures.

Table 4.3. Thermodynamic parameters for PhOH adsorption and activation barriers for PhOH hydrogenation catalyzed by Ni/γ-Al_2O_3

Solvent	$\Delta H^{\ddagger}_{PhOH}$ (kJ mol^{-1})	$\Delta S^{\ddagger}_{PhOH}$ (J mol^{-1} K^{-1})	ΔH_{ads} (kJ mol^{-1})	ΔS_{ads} (J mol^{-1} K^{-1})
2-PrOH	86	120	-8.5	-9.5
n-decane	39	22	68	163

Van't Hoff plots for the adsorption constants $K´_{PhOH}$ are shown in Figure 4.7b. The apparent adsorption enthalpy and entropy are both close to zero in 2-propanol, thus $K´_{PhOH}$ changes little with temperature. Both values are both large and positive in *n*-decane, but the enthalpic term dominates so that $K´_{PhOH}$ increases with temperature. The enthalpy and entropy of adsorption reflect the change in solvation of phenol vs. solvent upon adsorption,

as well as the difference in interactions between phenol vs. solvent at the adsorption site (*), eq 4.2:

$$PhOH + Solv* \rightleftarrows PhOH* + Solv \quad (4.2)$$

Decane solvates phenol poorly, and binds less strongly than phenol at the adsorption sites. However, hydrogen-bonded phenol clusters in the non-polar solvent must be disrupted to allow phenol to adsorb.[20–22] Consequently, adsorption involves increases in both enthalpy and entropy. In contrast, 2-propanol solvates phenol more effectively, via hydrogen-bonding, and competes with phenol for adsorption on the active sites. The loss of hydrogen-bonding upon phenol adsorption is balanced by a gain of hydrogen-bonding upon solvent desorption, resulting in much smaller changes in both enthalpy and entropy.

4.3.4 Phenol Adsorption onto Ni/γ-Al_2O_3 at Room Temperature

Since the values of K'_{PhOH} are not measured directly but arise from kinetic curvefitting, independent adsorption measurements were made at 295 K using a conventional equilibrium method in the absence of H_2. The results are shown in Table S4.4.[23] The equilibrium adsorption constants K'_{cat} are defined as shown in eq 4.11-4.12, and listed in Table 4.1. Note that these values refer to phenol adsorption on the support (161 m^2/g_{cat}) as well as the air-exposed metal (1 m^2/g_{cat}),[13] whereas K'_{PhOH} reflects only phenol adsorption on the reduced nickel active sites.

$$K_{Cat} = \frac{\theta_{PhOH}\, C_{Solv}}{\theta_{Solv}\, C_{PhOH}} = \frac{\theta_{PhOH}\, C_{Solv}}{(1-\theta_{PhOH})\, C_{PhOH,eq}} \quad (4.11)$$

$$K'_{Cat} = \frac{K_{Cat}}{C_{Solv}} = \frac{\theta_{PhOH}}{(1-\theta_{PhOH})\, C_{PhOH,eq}} \quad (4.12)$$

Despite the very different measurement temperatures (295 vs. 473 K) and adsorption sites (NiO + support vs. Ni alone), the values of K'_{cat} and K'_{PhOH} in a particular solvent are

similar in magnitude. The relationship between them is shown in Figure 4.8. For pyridine, no K'_{PhOH} value is available due to the absence of measurable PhOH hydrogenation at 473 K in this solvent. However, the value of K'_{cat}, 1.4 M^{-1}, was measured.

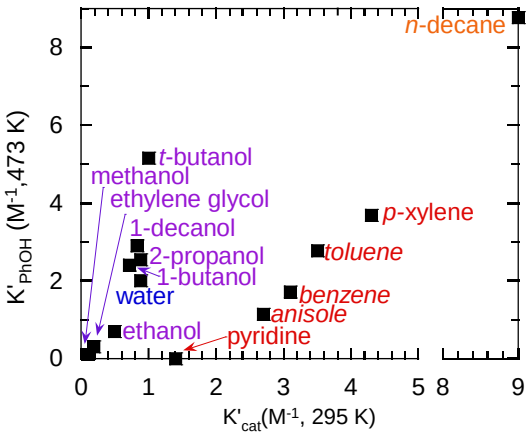

Figure 4.8. Relationship between the equilibrium constant K'_{PhOH} extracted from kinetic profiles for PhOH hydrogenation catalyzed by Ni/γ-Al_2O_3 at 473 K in various solvents (see Methods for reaction conditions) to PhOH adsorption constants K'_{cat} measured directly in the same solvents at 295 K.

Since K'_{cat} can be used to predict K'_{PhOH}, and since K'_{PhOH} determines the rate of phenol hydrogenation at 473 K (Table 4.1), K'_{cat} is well-correlated with $k'_{obs,PhOH}$, Figure S4.7. However, there are different linear correlations for protic and aprotic solvents, with (dimensionless) slopes of 3.2 and 1.2, respectively, Figure 4.9. For the protic solvents, the *x*-intercept is small, 0.1(1) M^{-1}, implying that PhOH hydrogenation at 473 K is very slow when PhOH adsorption on the catalyst (both Ni and the support) becomes negligible. A corollary is that almost all of the adsorbed PhOH (regardless of where it is adsorbed) is available for reaction in protic solvents. In contrast, the correlation for the aprotic solvents

has a significant *x*-intercept, 1.4 M^{-1}. Thus a significant amount of the phenol adsorbed at room temperature must be located on adsorption sites where it is unavailable for reaction at 473 K. These sites likely correspond to Lewis acid sites of the support, which adsorb phenol strongly and do not allow migration to the metal nanoparticles. Interestingly, the K'_{cat} value measured in pyridine lies precisely on the regression line for the aprotic solvents, even though no reaction was detected in pyridine at 473 K, Figure 4.9b. The solvent *t*-butanol deviates from the trendline for the protic solvents and is excluded from the fit. For the measured K'_{cat} , the K'_{PhOH} value is higher than predicted by the slope of the trendline.

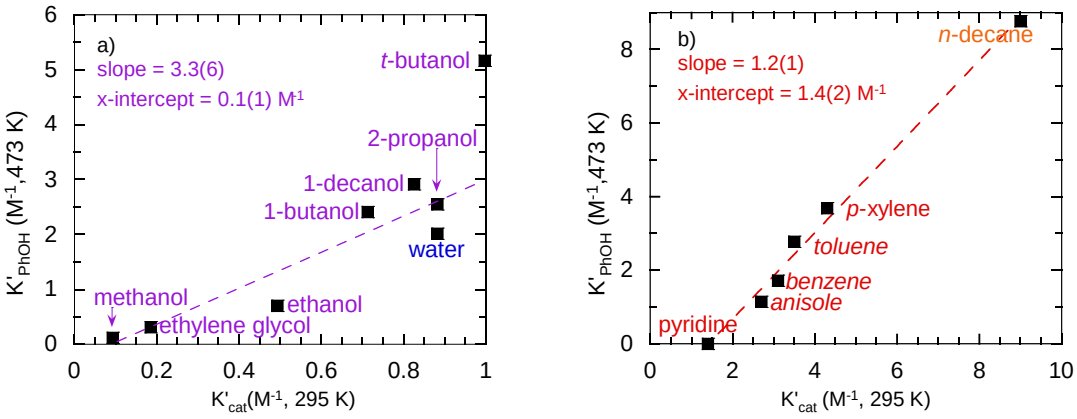

Figure 4.9. Relationship between the equilibrium constant K'_{PhOH} extracted from kinetic profiles for PhOH hydrogenation catalyzed by Ni/γ-Al_2O_3 at 473 K in various solvents (see reaction conditions in Methods) and the PhOH adsorption constants K'_{cat} measured directly in the same solvents at 295 K, for (a) protic solvents, and (b) aprotic solvents. Dashed lines represent the linear regression for each set of solvents (data for *t*-butanol is a significant outlier and is not included in the regression line for the protic solvents).

The extent of PhOH adsorption is determined by its solvation, as well as by the competing solvation of the catalyst surface. Protic solvents stabilize PhOH through

hydrogen-bonding to their OH groups, but the oxygen of the alcohol group also competes with PhOH for adsorption on the catalyst surface.[24] Since PhOH is more acidic than aliphatic alcohols, the former is the H-bond donor.[25] H-bond strength is inversely correlated with ΔpK_a, the difference between the pK_a values of the H-bond donor and pK_{BH+} values of the acceptor, or conjugate base.[25] H-bond strength reaches a maximum when ΔpK_a approaches zero. Methanol and ethylene glycol have the smallest ΔpK_a values (11.5 and 12, respectively), and should therefore form stronger hydrogen bonds with PhOH. H-bond strength between PhOH and each monoprotic solvent is correlated with the K'_{cat} adsorption equilibrium constant, Figure S4.8. Solvents with smaller ΔpK_a values will show stronger solvation of PhOH in solution, explaining the smaller K'_{cat} constants. Adsorption is a complex process with multiple interactions occurring on the surface of the catalyst and in solution. Nevertheless, the correlation between ΔpK_a and K'_{cat} suggests that solvents with stronger basicity form weaker H-bonds with PhOH, leading to poorer solvation and an increased PhOH coverage on the catalyst.

In contrast, the correlation between adsorption constants for the aprotic solvents has a significant positive *x*-intercept, corresponding to K'_{cat} = 1.4 M^{-1} at 295 K, Figure 4.9b. This behavior implies that the rate of PhOH hydrogenation is significant only when a threshold adsorption on the catalyst is exceeded. The threshold, K'_{cat} = 1.4 M^{-1} (0.15 mmol g_{cat}^{-1}), corresponds to an amount of adsorbed PhOH unavailable for reaction. It must be strongly adsorbed on the support and not labile enough to migrate onto the active Ni surface. Adsorption of aromatic solvents onto alumina, or other similar metal oxide supports, occurs predominantly through interactions with Lewis acid sites, with contributions from alumina hydroxyl O–H···π interactions.[26] The adsorption of aromatic hydrocarbons on metal

nanoparticles has been assumed to occur via the interaction of π-electrons of the aromatic ring with d-orbitals of the metal.

Pyridine, a strong base, has been shown to form strong bonds with the Ni active sites,[27] and can also effectively solvate phenol through hydrogen bonding. The solvent *n*-decane, however, adsorbs weakly to the Ni sites and solvates phenol poorly, leading to a high surface coverage of PhOH in *n*-decane and a low coverage in pyridine. For benzene, adsorption of the aromatic ring has been shown to occur parallel to Ni(100) and Ni (111) surfaces.[28] At low coverages toluene is adsorbed with the plane of the aromatic ring parallel to the surface.[29] Increasing toluene coverage leads to repulsion between the methyl groups and adjacent toluene molecules, resulting in adsorption of toluene that is not parallel to the surface. Additional studies have also shown that adsorption of aromatic hydrocarbons decreases with an increase in methyl derivatives on the aromatic ring.[30–32] In the aromatic hydrocarbon solvents, benzene, toluene and *p*-xylene, the amount of PhOH hydrogenation increases with the methylation of the benzene ring. Therefore, aromatic hydrocarbons with greater methylation compete less strongly for adsorption sites on the Ni surface, allowing for a greater PhOH coverage and rate of hydrogenation.

4.3.5 Kinetic Model for Benzyl Phenyl Ether Hydrogenolysis

Applying our findings on the kinetics of PhOH hydrogenation, the kinetics of BPE hydrogenolysis catalyzed by Ni/γ-Al_2O_3 was reexamined. Previously, the kinetics in 2-propanol were modeled using a pseudo-first-order kinetic equation.[13] However, this model clearly does not describe the profile in *n*-decane (Figure S4.9). The behavior suggests the need to account for the adsorption of BPE and potentially the various hydrogenolysis products.

The Langmuir-Hinshelwood model for BPE hydrogenolysis consists of six reactions. Eq 4.13 shows the dissociative chemisorption of H_2 on available surface sites (*). Eqs 4.14-4.16 describe the quasi-equilibrated adsorption of each organic species, displacing adsorbed solvent molecules (whose number is not known *a priori*). Eqs 4.16-4.18 show the kinetically significant reactions (not necessarily elementary) of the dissociation of BPE to give adsorbed benzyl and phenoxy,[32,33] combination of these fragments with adsorbed H, and subsequent hydrogenation of adsorbed PhOH.

$$H_2 + 2\,Solv* \rightleftarrows 2H* \qquad K_H \qquad (4.13)$$

$$BPE + Solv* \rightleftarrows BPE* + Solv \qquad K_{BPE} \qquad (4.14)$$

$$PhOH + Solv* \rightleftarrows PhOH* + Solv \qquad K_{PhOH} \qquad (4.15)$$

$$Tol + Solv* \rightleftarrows Tol* + Solv \qquad K_{Tol} \qquad (4.16)$$

$$BPE* \rightarrow PhO* + Benzyl* \qquad k_{BPE} \qquad (4.17)$$

$$PhO* + H* \rightarrow PhOH* \qquad k_{PhO} \qquad (4.18)$$

$$Benzyl* + H* \rightarrow Tol* \qquad k_{Benzyl} \qquad (4.19)$$

$$PhOH* + 6H* \rightarrow CyOH \qquad k_{PHOH} \qquad (4.20)$$

Since H_2 is typically present in excess (ca. 20 mol H_2/mol BPE), and since experiments conducted with higher H_2 pressures showed no significant differences in either rate or product distribution (Figure S4.5),[13] we assume that H_2 adsorption is not competitive with BPE adsorption, and that its coverage, θ_H, is constant.

The C-O bond cleavage in eq 4.17 is the rate-limiting step,[32,33] therefore the coverages of all organic species are quasi-equilibrated. The adsorption-desorption equilibria can be described algebraically (eq 4.21-4.24), where θ_i is the surface coverage and C_i is the concentration of species i in solution. The complete site balance (excluding H) is given by eq 4.25. It assumes that solvent occupies any site not occupied by a reacting species. Substitution of eq 4.21-4.24 into eq 4.25 yields an equation for the surface coverage of solvent, θ_{Solv} (eq 4.26).

$$K_{BPE} = \frac{\theta_{BPE} C_{Solv}}{\theta_{Solv} C_{BPE}} \tag{4.21}$$

$$K_{PhOH} = \frac{\theta_{PhOH} C_{Solv}}{\theta_{Solv} C_{PhOH}} \tag{4.22}$$

$$K_{Tol} = \frac{\theta_{Tol} C_{Solv}}{\theta_{Solv} C_{Tol}} \tag{4.23}$$

$$K_H = \frac{\theta_H^2 C_{Solv}^2}{\theta_{Solv}^2 C_{H_2}} \tag{4.24}$$

$$\theta_{BPE} + \theta_{PhOH} + \theta_{Tol} + \theta_{Solv} = 1 \tag{4.25}$$

$$\theta_{Solv} = \left(1 + \frac{K_{BPE} C_{BPE}}{C_{Solv}} + \frac{K_{Tol} C_{Tol}}{C_{Solv}} + \frac{K_{PhOH} C_{PhOH}}{C_{Solv}}\right)^{-1} \tag{4.26}$$

Eq 4.26 can be simplified by assuming the contribution from K_{Tol} are small since θ_{Tol} is expected to be small due to the weak competitive adsorption of toluene relative to PhOH. Adsorption of PhOH onto Ni/γ-Al_2O_3 showed ca. 4x more adsorption in the solvent toluene than 2-propanol, indicating weak competitive adsorption, Table S4.5. Additionally, the values of K'_{PhOH} from PhOH hydrogenation at 448 k in 2-propanol and *n*-decane (Table 4.2)

were fixed in eq S4.1. Values for K'_{BPE} in *n*-decane and 2-propanol did not change significantly with the absence of K'_{PhOH}, but led to significantly smaller fit errors, Table S4.6. Thus, eq 4.26 simplifies to eq 4.27 and θ_{BPE} is defined in eq 4.28.

$$\theta_{Solv} = \frac{C_{Solv}}{C_{Solv} + K_{BPE} C_{BPE}} \tag{4.27}$$

$$\theta_{BPE} = \frac{K_{BPE} C_{BPE}}{C_{Solv} + K_{BPE} C_{BPE}} \tag{4.28}$$

The rates of BPE hydrogenolysis and PhOH hydrogenation are given in eq 4.29-4.30, where n_{Ni} is the moles of nickel active sites.

$$-\frac{dC_{BPE}}{dt} = \frac{k'_{BPE} K'_{BPE} C_{BPE}}{(1 + K'_{BPE} C_{BPE})} \tag{4.29}$$

$$\frac{dC_{PhOH}}{dt} = \frac{k'_{BPE} K'_{BPE} C_{BPE} - k'_{PhOH} K'_{PhOH} C_{PhOH}}{(1 + K'_{BPE} C_{BPE})} \tag{4.30}$$

where $k'_{BPE} = k_{BPE}\, \theta_H\, n_{Ni} / V$, $K'_{BPE} = K_{BPE}/C_{Solv}$, and V is the liquid volume under the reaction conditions. Here k'_{BPE} is a "pseudo-zeroth-order" rate constant with dimensions [M s^{-1}] and K'_{BPE} is a conditional equilibrium constant with dimensions [M^{-1}].

4.3.6 Curvefits for the Benzyl Phenyl Ether Kinetic Profiles

Values for k'_{BPE} and K'_{BPE} were estimated by fitting eq 4.29 to BPE kinetic profiles recorded in 2-propanol and n-decane, Table 4.4. The value of k'_{BPE} is the same in both solvents (2-propanol: 5.6(2.0) M s^{-1}; *n*-decane: 5.4(3.5) M s^{-1}), while K'_{BPE} appears to be much larger in *n*-decane, 65(400) M^{-1}, than in 2-propanol, 11(10) M^{-1}. However, the confidence interval for K'_{BPE} in *n*-decane is very large, likely due to the small number of significant data points (5). Due to the agreement in k'_{BPE} values, the value was fixed at the average, 5.5 M s^{-1}, and K'_{BPE} was estimated by fitting eq 4.29 to the n-decane data (Figure

4.10). The resulting value for K'_{BPE} in *n*-decane is 22(11) M^{-1}, which is double the value in 2-propanol. Thus, the slightly faster rate of BPE hydrogenolysis in *n*-decane is likely caused by slightly more competitive adsorption of BPE, and higher θ_{BPE}, in the aprotic solvent. Adsorption of BPE onto by Ni/γ-Al_2O_3 is ca. 2x greater in *n*-decane than 2-propanol, Table S4.8, while adsorption of PhOH is ca. 7x greater in *n*-decane than 2-propanol. Solvent *n*-decane likely interacts with BPE and PhOH in a similar manner, predominantly through London dispersion and van der Waals forces.[35] In contrast, 2-propanol can hydrogen bond with PhOH leading to enhanced solvation and a decrease in adsorption relative to BPE.

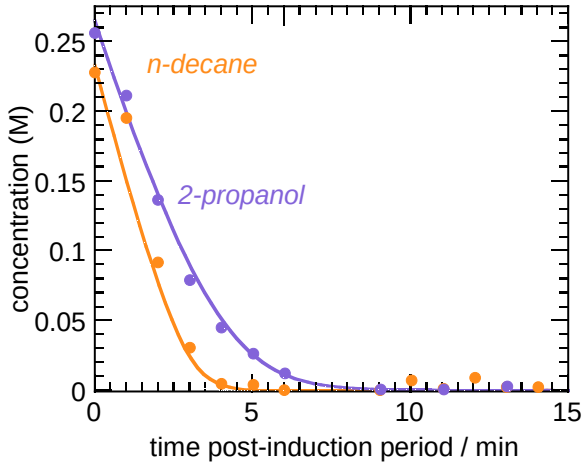

Figure 4.10. BPE kinetic profiles during hydrogenolysis of BPE (0.33 mmol) catalyzed by Ni/γ-Al_2O_3 (30 mg, 2 wt% Ni) at 448 K with 50 bar H_2, in either 2-propanol or *n*-decane as solvent (120 mL). The curvefit was obtained using eq 4.29, with only the first 10 data points, reflecting the timescale of BPE hydrogenolysis, used to calculate the sum of squared errors. Since the catalyst was air-exposed prior to use, all profiles had a short induction period (ca. 5 min, not shown), attributed to reduction of the surface oxide.

Table 4.4. Kinetic parameters for BPE hydrogenolysis [a]

Solvent	Two-parameter curvefit		Single-parameter curvefit[b]	
	k'_{BPE} [M s^{-1}]	K'_{BPE} [M^{-1}]	K'_{BPE} [M^{-1}]	$k'_{obs,BPE}$ [s^{-1}]
2-propanol	5.6 (2.0)	11 (10)	12 (2)	66(11)
n-decane	5.4 (3.5)	65 (400)	22 (11)	121(60)

[a] Determined by minimizing the sum of squared errors. Values in parentheses indicate the 95% confidence interval. [b] k'_{BPE} fixed at 5.5 M s^{-1}. Rate and equilibrium constants were calculated during the hydrogenolysis of BPE (0.33 mmol) catalyzed by Ni/γ-Al_2O_3 (30 mg, 2 wt% Ni) at 448 K with 50 bar H_2, in either 2-propanol or *n*-decane as solvent (120 mL).

4.4 Conclusions

Operando MAS NMR spectroscopy provides detailed kinetic and mechanistic information about the hydrogenolysis of BPE and hydrogenation of PhOH catalyzed by Ni/γ-Al_2O_3 in a wide range of solvents. One of the more significant findings to emerge from this study is the hydrogen bonding strength of the protic solvents playing a critical role in stabilization of PhOH in solution and competing for adsorption sites. The hydrogenolysis of BPE is shown to have a small dependence on the composition of the solvent used in the reaction, however the stability of the product PhOH is strongly solvent dependent. In protic solvents the stability of PhOH increases with hydrogen bonding strength, as defined by the ΔpK_a value, where ΔpK_a values closer to 0 represent stronger hydrogen bonds. Protic solvents, such as t-butanol, with large ΔpK_a values and thus weaker hydrogen bonding led to a greater extend of phenol hydrogenation. In aprotic solvents, the stability of phenol is found to correlate strongly with the solvents ability to compete for Ni active sites. Increases in

methylation of the aromatic ring showed a decrease in the adsorption strength of the solvent and thus a greater rate of phenol hydrogenation. With the strong correlations found between adsorption of PhOH onto the catalyst and rates of hydrogenation, rates of PhOH hydrogenation can be easily predicted with a simple adsorption experiment. Furthermore, applying these findings to the experimental design of new systems, rates and selectivites can be optimized with fewer reactions.

4.5 Experimental Methods

4.5.1 Chemicals.

The following were purchased from commercial suppliers and used as received: toluene-α-^{13}C and phenol-1-^{13}C (98 % purity, 99 atom % ^{13}C, Cambridge Isotopes), *n*-decane (anhydrous 99%, Sigma-Aldrich), *p*-xylene (99%, Sigma-Aldrich), toluene (anhydrous 99.9%, Sigma-Aldrich), benzene (anhydrous 99.8%, Alfa Aesar), anisole (anhydrous 99.7%, Sigma-Aldrich), pyridine (anhydrous 99.8%, Sigma-Aldrich), 1-decanol (98%, Fisher), *t*-butanol (anhydrous 99.5%, Sigma-Aldrich), 1-butanol (Certified ACS, Fisher), 2-propanol (HPLC Grade, Fisher), ethanol (100%), methanol (HPLC grade, Fisher), ethylene glycol (Reagent Grade, Fisher), water (HPLC grade, Fisher) $Ni(NO_3)_2 \cdot 6H_2O$ (98.5%, Sigma-Aldrich), γ-Al_2O_3 (≥97%, pore volume: 0.40 mL/g, B.E.T. surface area 185 m^2/g, Strem) . Solvents Selectively ^{13}C-labelled benzyl phenyl ether was synthesized from toluene-α-^{13}C and phenol-1-^{13}C according to literature procedures.[13] The 2 wt% Ni/γ-Al_2O_3 catalyst was prepared using a modified literature procedure.[13]

4.5.2 Solution state NMR adsorption measurements.

Phenol adsorption experiments were conducted by mixing 20 mg Ni/γ-Al_2O_3 with 1.5 mL phenol solution (40 mM in various solvents). The resulting slurries were stirred using a vortex mixer for 30 min at room temperature (295 K), then centrifuged. The supernatant was decanted, and its ^{1}H NMR spectrum was recorded on a Varian Unity Inova 500MHz NMR spectrometer. Every resonance for both phenol and the solvent were integrated and the ratio of the integrated NMR resonances for phenol and solvent was compared to that of the stock solution. The difference was used to determine amount of adsorbed phenol.

4.5.3 *Operando* MAS-NMR Spectroscopy.

Magic-angle-spinning (MAS) NMR experiments were performed on a Bruker Avance 500MHz NMR spectrometer equipped with an 11.7 T magnet, and using a 7.5 mm Revolution NMR magic-angle spinning (MAS) triple resonance HXY probe. Calibration of the spectrometer temperature setting was achieved by acquiring ^{207}Pb NMR spectra of $Pb(NO_3)_2$. Acquisition parameters have been previously described.[13]

In a typical high T/P experiment, a customized 7.5 mm ZrO_2 rotor was loaded with BPE or PhOH (6.0 mg), 2 wt% Ni/γ-Al_2O_3 (30 mg) and 2-propanol (120 μL), then pressurized with 50 bar H_2 at room temperature. The MAS rate was 3 kHz. Spectra were collected starting when the probe reached the desired temperature, ca. 5-10 min after heating of the rotor commenced. Each transient spectrum was acquired by averaging 2-8 scans, unless specified otherwise. ^{13}C chemical shifts were referenced to TMS via a secondary standard, adamantane (37.48 ppm). [35]

4.5.4 Kinetic analysis.

Kinetic profiles for conversion of BPE, production of toluene and phenol, and hydrogenation of phenol were analyzed by non-linear least-squares curvefitting using MATLAB (MatWorks Software). Concentrations of all species were normalized based on the initial concentration of BPE and PhOH, Table S4.1.

4.6 References

(1) Singh, N.; Campbell, C. T. A Simple Bond-Additivity Model Explains Large Decreases in Heats of Adsorption in Solvents Versus Gas Phase: A Case Study with Phenol on Pt(111) in Water. *ACS Catal.* **2019**, *9* (9), 8116–8127.

(2) Akinola, J.; Barth, I.; Goldsmith, B. R.; Singh, N. Adsorption Energies of Oxygenated Aromatics and Organics on Rhodium and Platinum in Aqueous Phase. *ACS Catal.* **2020**, *10* (9), 4929–4941.

(3) Sievers, C.; Noda, Y.; Qi, L.; Albuquerque, E. M.; Rioux, R. M.; Scott, S. L. Phenomena Affecting Catalytic Reactions at Solid–Liquid Interfaces. *ACS Catal.* **2016**, *6* (12), 8286–8307.

(4) Solvent Effects on the Rates of Homogeneous Chemical Reactions. In *Solvents and Solvent Effects in Organic Chemistry*; John Wiley & Sons, Ltd, 2002; pp 147–328.

(5) Albery, J. Solvent Isotope Effects. In *Proton-Transfer Reactions*; Caldin, E., Gold, V., Eds.; Springer US: Boston, MA, 1975; pp 263–315.

(6) Akpa, B. S.; D'Agostino, C.; Gladden, L. F.; Hindle, K.; Manyar, H.; McGregor, J.; Li, R.; Neurock, M.; Sinha, N.; Stitt, E. H.; Weber, D.; Zeitler, J. A.; Rooney, D. W. Solvent Effects in the Hydrogenation of 2-Butanone. *J. Catal.* **2012**, *289*, 30–41.

(7) Ramos, R.; Tišler, Z.; Kikhtyanin, O.; Kubička, D. Solvent Effects in Hydrodeoxygenation of Furfural-Acetone Aldol Condensation Products over Pt/TiO_2 Catalyst. *Appl. Catal. Gen.* **2017**, *530*, 174–183.

(8) Xia, H.; Tan, H.; Cui, H.; Song, F.; Zhang, Y.; Zhao, R.; Chen, Z.-N.; Yi, W.; Li, Z. Tunable Selectivity of Phenol Hydrogenation to Cyclohexane or Cyclohexanol by a Solvent-Driven Effect over a Bifunctional Pd/NaY Catalyst. *Catal. Sci. Technol.* **2021**, *11* (5), 1881–1887.

(9) Bertero, N. M.; Trasarti, A. F.; Apesteguía, C. R.; Marchi, A. J. Solvent Effect in the Liquid-Phase Hydrogenation of Acetophenone over Ni/SiO_2: A Comprehensive Study of the Phenomenon. *Appl. Catal. Gen.* **2011**, *394* (1), 228–238.

(10) Yoshida, H.; Onodera, Y.; Fujita, S.; Kawamori, H.; Arai, M. Solvent Effects in Heterogeneous Selective Hydrogenation of Acetophenone: Differences between Rh/C and Rh/Al_2O_3 Catalysts and the Superiority of Water as a Functional Solvent. *Green Chem.* **2015**, *17* (3), 1877–1883.

(11) Wan, H.; Vitter, A.; Chaudhari, R. V.; Subramaniam, B. Kinetic Investigations of Unusual Solvent Effects during Ru/C Catalyzed Hydrogenation of Model Oxygenates. *J. Catal.* **2014**, *309*, 174–184.

(12) Chamas, A.; Qi, L.; Mehta, H. S.; Sears, J. A.; Scott, S. L.; Walter, E. D.; Hoyt, D. W. High Temperature/Pressure MAS-NMR for the Study of Dynamic Processes in Mixed Phase Systems. *Magn. Reson. Imaging* **2019**, *56*, 37–44.

(13) Qi, L.; Chamas, A.; Jones, Z. R.; Walter, E. D.; Hoyt, D. W.; Washton, N. M.; Scott, S. L. Unraveling the Dynamic Network in the Reactions of an Alkyl Aryl Ether Catalyzed by $Ni/\gamma\text{-}Al_2O_3$ in 2-Propanol. *J. Am. Chem. Soc.* **2019**, *141* (43), 17370–17381.

(14) Walter, E. D.; Qi, L.; Chamas, A.; Mehta, H. S.; Sears, J. A.; Scott, S. L.; Hoyt, D. W. Operando MAS NMR Reaction Studies at High Temperatures and Pressures. *J. Phys. Chem. C* **2018**, *122* (15), 8209–8215.

(15) Wang, X.; Rinaldi, R. Solvent Effects on the Hydrogenolysis of Diphenyl Ether with Raney Nickel and Their Implications for the Conversion of Lignin. *ChemSusChem* **2012**, *5* (8), 1455–1466.

(16) Lide, D. R. *CRC Handbook of Chemistry and Physics*; CRC press, 2004; Vol. 85.

(17) Empirical Parameters of Solvent Polarity. In *Solvents and Solvent Effects in Organic Chemistry*; John Wiley & Sons, Ltd, 2002; pp 389–469.

(18) Ambrose, D.; Sprake, C. H. S. Thermodynamic Properties of Organic Oxygen Compounds XXV. Vapour Pressures and Normal Boiling Temperatures of Aliphatic Alcohols. *J. Chem. Thermodyn.* **1970**, *2* (5), 631–645.

(19) Willingham, C.; Taylor, W. J.; Pignocco, J. M.; Rossini, F. Vapor Pressures and Boiling Points of Some Paraffin, Alkylcyclopentane, Alkylcyclohexane, and Alkylbenzene Hydrocarbons. **1945**.

(20) Wakisaka, A.; Yamamoto, Y.; Akiyama, Y.; Takeo, H.; Mizukami, F.; Sakaguchi, K. Solvation-Controlled Clustering of a Phenol–Pyridine Acid–Base Pair. *J. Chem. Soc. Faraday Trans.* **1996**, *92* (18), 3339–3346.

(21) Wakisaka, A.; Akiyama, Y.; Yamamoto, Y.; Engst, T.; Takeo, H.; Mizukami, F.; Sakaguchi, K.; Jones, H. Molecular Self-Assembly Controlled by Acid–Base Non-Covalent Interactions: A Mass Spectrometric Study of Some Organic Acids and Bases. *J. Chem. Soc. Faraday Trans.* **1996**, *92* (19), 3539–3544.

(22) Bagno, A. Probing the Solvation Shell of Organic Molecules by Intermolecular 1H NOESY. *J. Phys. Org. Chem.* **2002**, *15* (12), 790–795.

(23) Moon, H.; Han, S.; L. Scott, S. Tuning Molecular Adsorption in SBA-15-Type Periodic Mesoporous Organosilicas by Systematic Variation of Their Surface Polarity. *Chem. Sci.* **2020**, *11* (14), 3702–3712.

(24) Guedes, R. C.; Coutinho, K.; Costa Cabral, B. J.; Canuto, S.; Correia, C. F.; Borges dos Santos, R. M.; Martinho Simões, J. A. Solvent Effects on the Energetics of the Phenol O−H Bond: Differential Solvation of Phenol and Phenoxy Radical in Benzene and Acetonitrile. *J. Phys. Chem. A* **2003**, *107* (43), 9197–9207.

(25) Gilli, P.; Pretto, L.; Bertolasi, V.; Gilli, G. Predicting Hydrogen-Bond Strengths from Acid−Base Molecular Properties. The PKa Slide Rule: Toward the Solution of a Long-Lasting Problem. *Acc. Chem. Res.* **2009**, *42* (1), 33–44.

(26) Rimola, A.; Civalleri, B.; Ugliengo, P. Physisorption of Aromatic Organic Contaminants at the Surface of Hydrophobic/Hydrophilic Silica Geosorbents: A B3LYP-D Modeling Study. *Phys. Chem. Chem. Phys.* **2010**, *12* (24), 6357–6366.

(27) Sheets, R.; Hansen, R. S. Promoted Adsorption of Pyridine on Nickel. *J. Phys. Chem.* **1972**, *76* (7), 972–976.

(28) Myers, A. K.; Schoofs, G. R.; Benziger, J. B. Comparison of Benzene Adsorption on Nickel(111) and Nickel(100). *J. Phys. Chem.* **1987**, *91* (9), 2230–2232.

(29) Coats, A. M.; Cooper, E.; Raval, R. Toluene Adsorption on Ni(111). *Surf. Sci.* **1994**, *307–309*, 89–94.

(30) Friend, C. M.; Muetterties, E. L. Coordination Chemistry of Metal-Surfaces. 3. Benzene and Toluene Interactions with Nickel Surfaces. *J. Am. Chem. Soc.* **1981**, *103* (4), 773–779.

(31) Myers, A. K.; Benziger, J. B. Effect of Methyl Substitution on the Interaction of Benzene with Nickel(100): An Experimental and Theoretical Study. *Langmuir* **1987**, *3* (3), 414–423.

(32) Becker, L.; Förster, H. Oxidative Decomposition of Benzene and Its Methyl Derivatives Catalyzed by Copper and Palladium Ion-Exchanged Y-Type Zeolites. *Appl. Catal. B Environ.* **1998**, *17* (1), 43–49.

(33) He, J.; Lu, L.; Zhao, C.; Mei, D.; Lercher, J. A. Mechanisms of Catalytic Cleavage of Benzyl Phenyl Ether in Aqueous and Apolar Phases. *J. Catal.* **2014**, *311*, 41–51.

(34) Zhu, C.; Cao, J.-P.; Zhao, X.-Y.; Xie, T.; Ren, J.; Wei, X.-Y. Mechanism of Ni-Catalyzed Selective CO Cleavage of Lignin Model Compound Benzyl Phenyl Ether under Mild Conditions. *J. Energy Inst.* **2019**, *92* (1), 74–81.

(35) Mathew, K.; Sundararaman, R.; Letchworth-Weaver, K.; Arias, T. A.; Hennig, R. G. Implicit Solvation Model for Density-Functional Study of Nanocrystal Surfaces and Reaction Pathways. *J. Chem. Phys.* **2014**, *140* (8), 084106.

(36) Morcombe, C. R.; Zilm, K. W. Chemical Shift Referencing in MAS Solid State NMR. *J. Magn. Reson.* **2003**, *162* (2), 479–486.

4.7 Appendix III

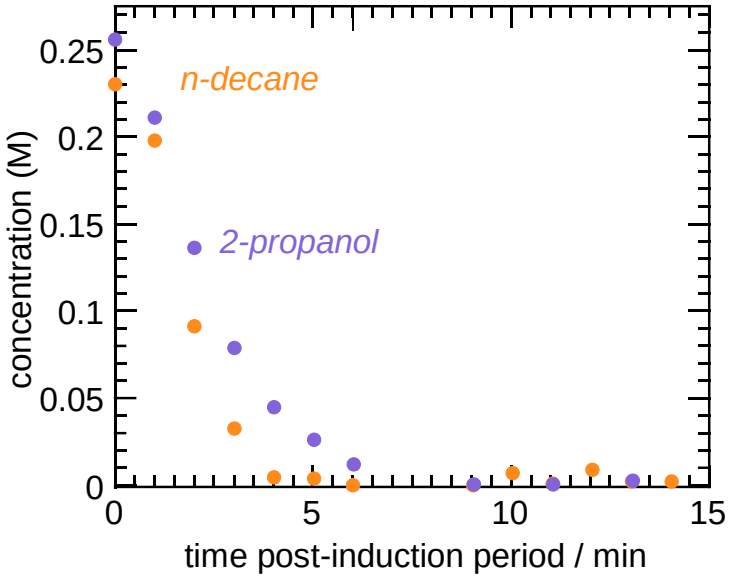

Figure S4.1. Comparison of BPE kinetic profiles in both 2-propanol and *n*-decane catalyzed by Ni/γ-Al_2O_3 (2 wt%) with 50 bar H_2 and 120 µL of solvent, after heating to 448 K. Since the catalyst was air-exposed prior to use, all profiles had a short induction period (ca. 5 min), attributed to reduction of the surface oxide.

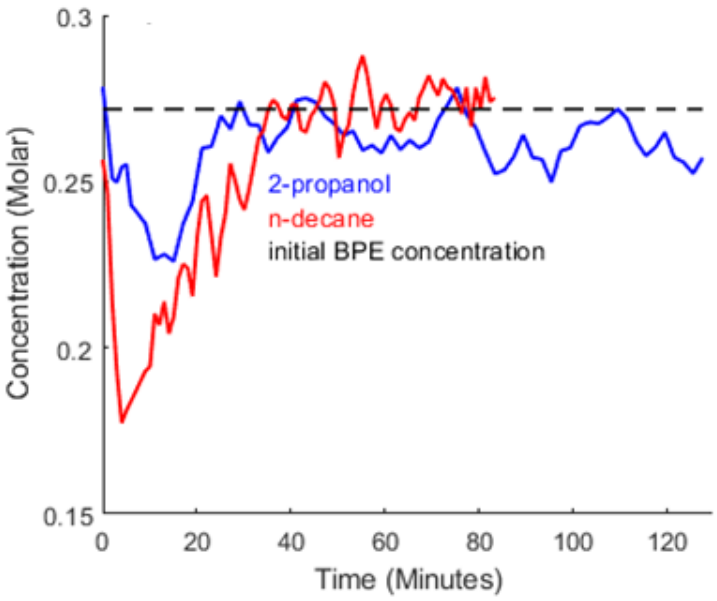

Figure S4.2. Mass balance in both 2-propanol and *n*-decane for the BPE hydrogenolysis reaction catalyzed by Ni/γ-Al_2O_3 (2 wt%) with 50 bar H_2 and 120 µL of solvent, after heating to 448 K.

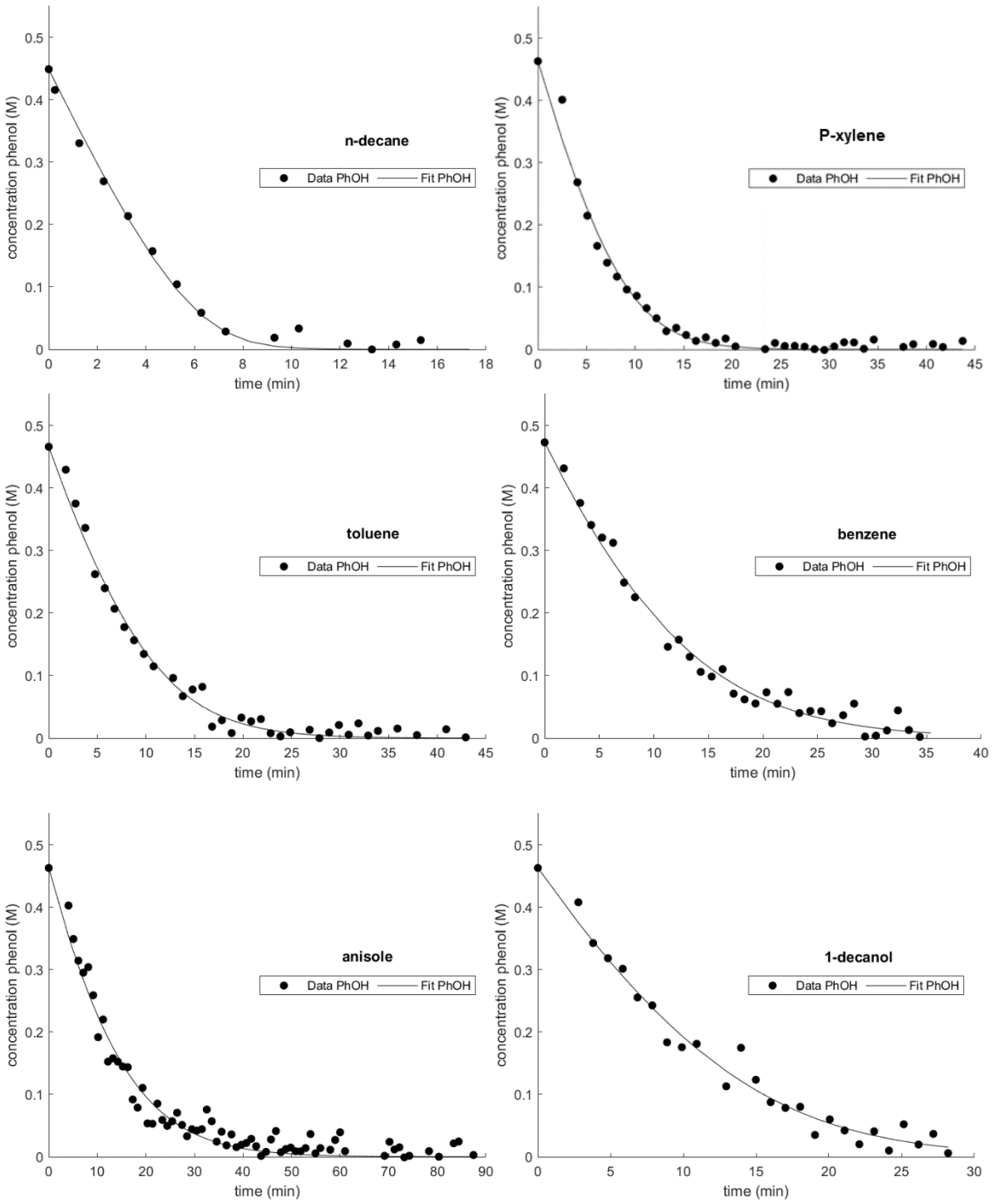
n-decane
Data PhOH
Fit PhOH
concentration phenol (M)
time (min)
P-xylene
Data PhOH
Fit PhOH
concentration phenol (M)
time (min)
toluene
Data PhOH
Fit PhOH
concentration phenol (M)
time (min)
benzene
Data PhOH
Fit PhOH
concentration phenol (M)
time (min)
anisole
Data PhOH
Fit PhOH
concentration phenol (M)
time (min)
1-decanol
Data PhOH
Fit PhOH
concentration phenol (M)
time (min)

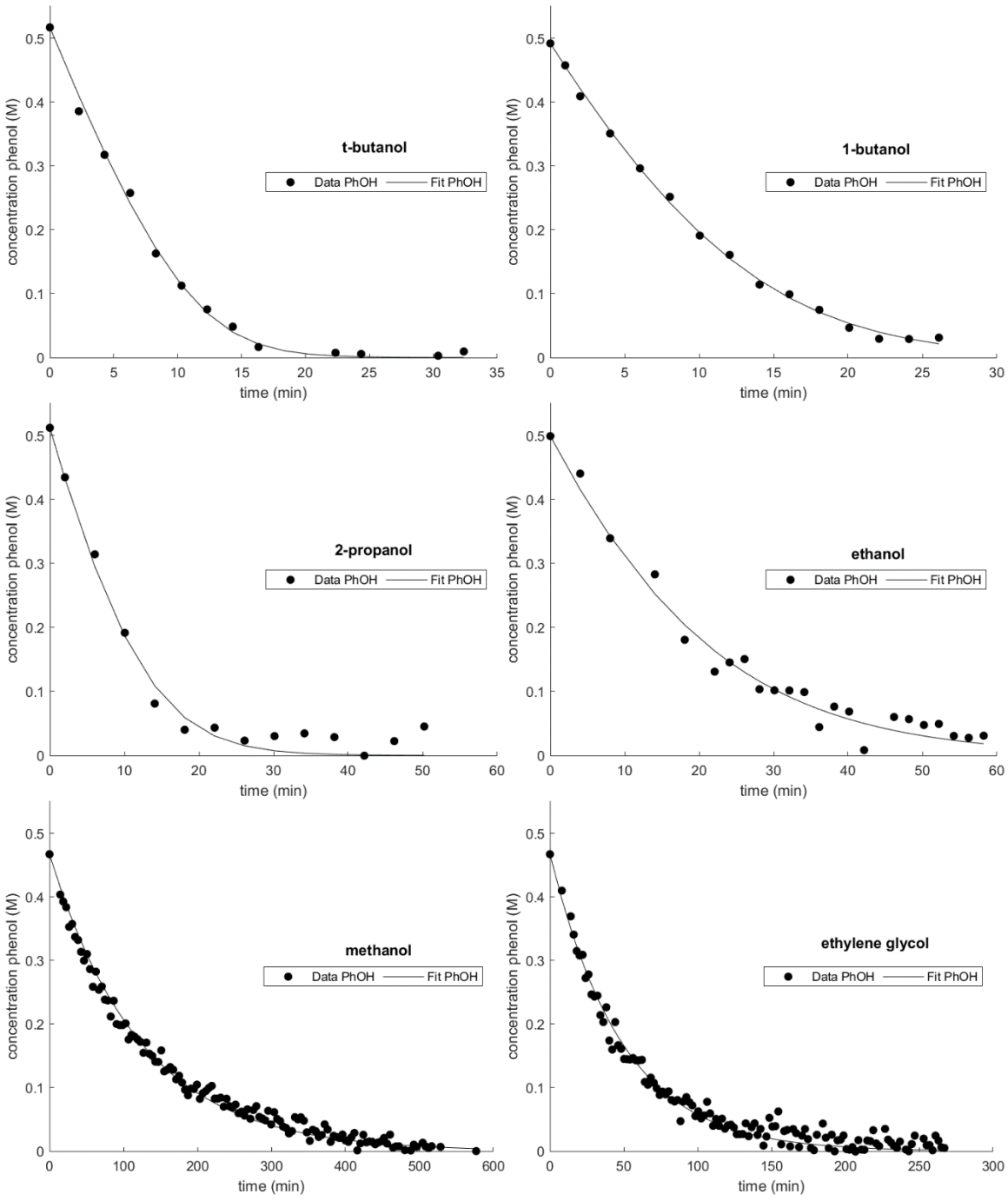
t-butanol
Data PhOH
Fit PhOH
concentration phenol (M)
time (min)
1-butanol
Data PhOH
Fit PhOH
concentration phenol (M)
time (min)
2-propanol
Data PhOH
Fit PhOH
concentration phenol (M)
time (min)
ethanol
Data PhOH
Fit PhOH
concentration phenol (M)
time (min)
methanol
Data PhOH
Fit PhOH
concentration phenol (M)
time (min)
ethylene glycol
Data PhOH
Fit PhOH
concentration phenol (M)
time (min)

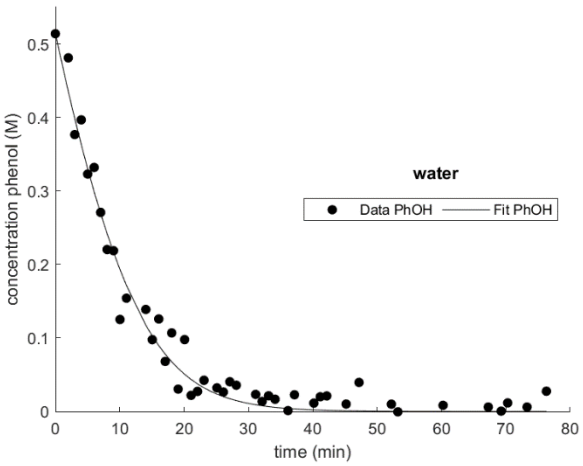

Figure S4.3. Kinetic analysis of individual ^{13}C NMR profiles recorded during PhOH hydrogenation in a rotor loaded with air-exposed Ni/γ-Al_2O_3 (2 wt%), 50 bar H_2, and 120 μL of solvent, after heating to 200 °C. Data collected during the induction period were removed prior to non-linear least-squares curvefitting. All solvents were analyzed with a Langmuir Hinshelwood based model (eq 4.29).

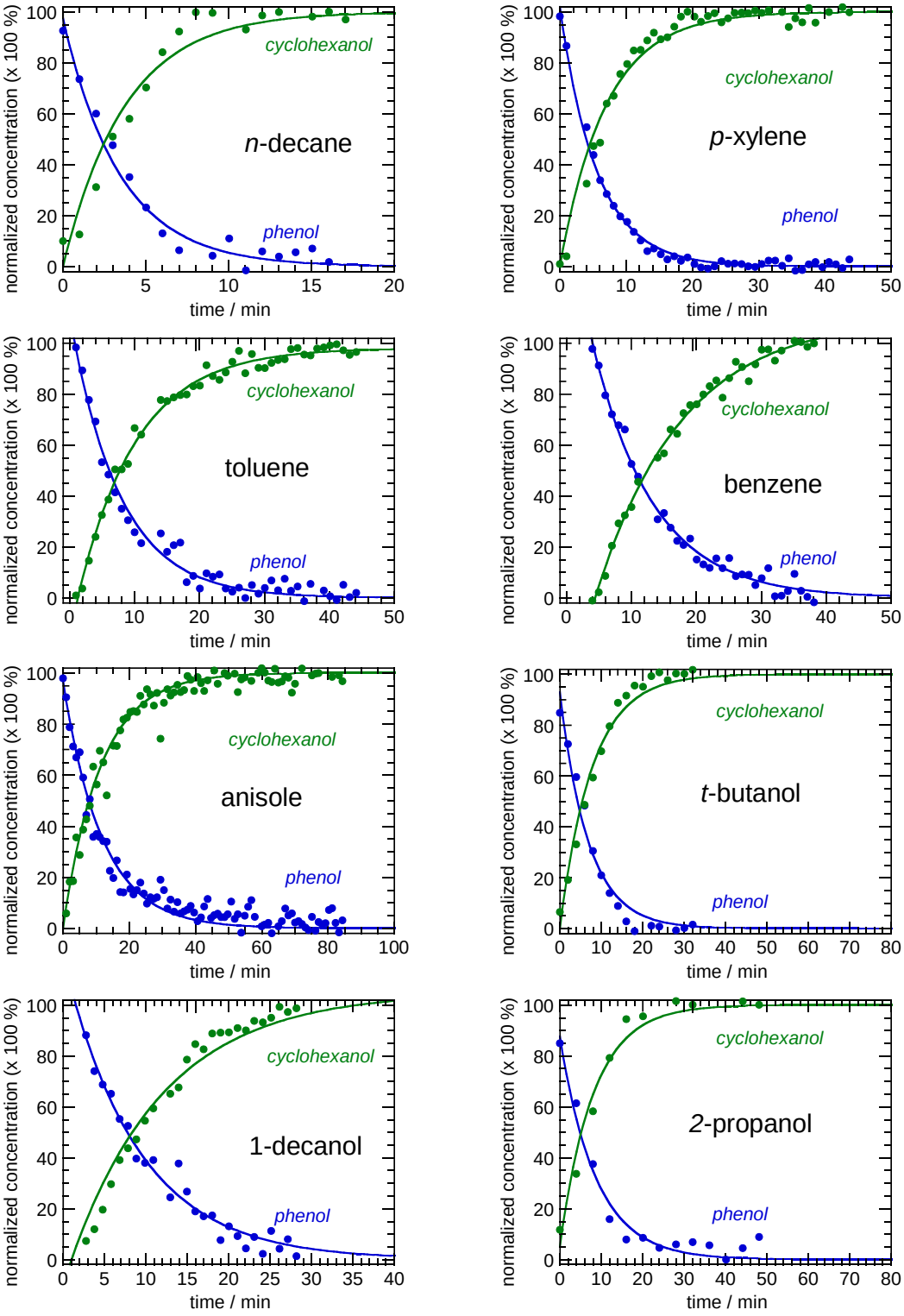
normalized concentration (x 100 %)
time / min
cyclohexanol
phenol
n-decane
p-xylene
toluene
benzene
anisole
t-butanol
1-decanol
2-propanol

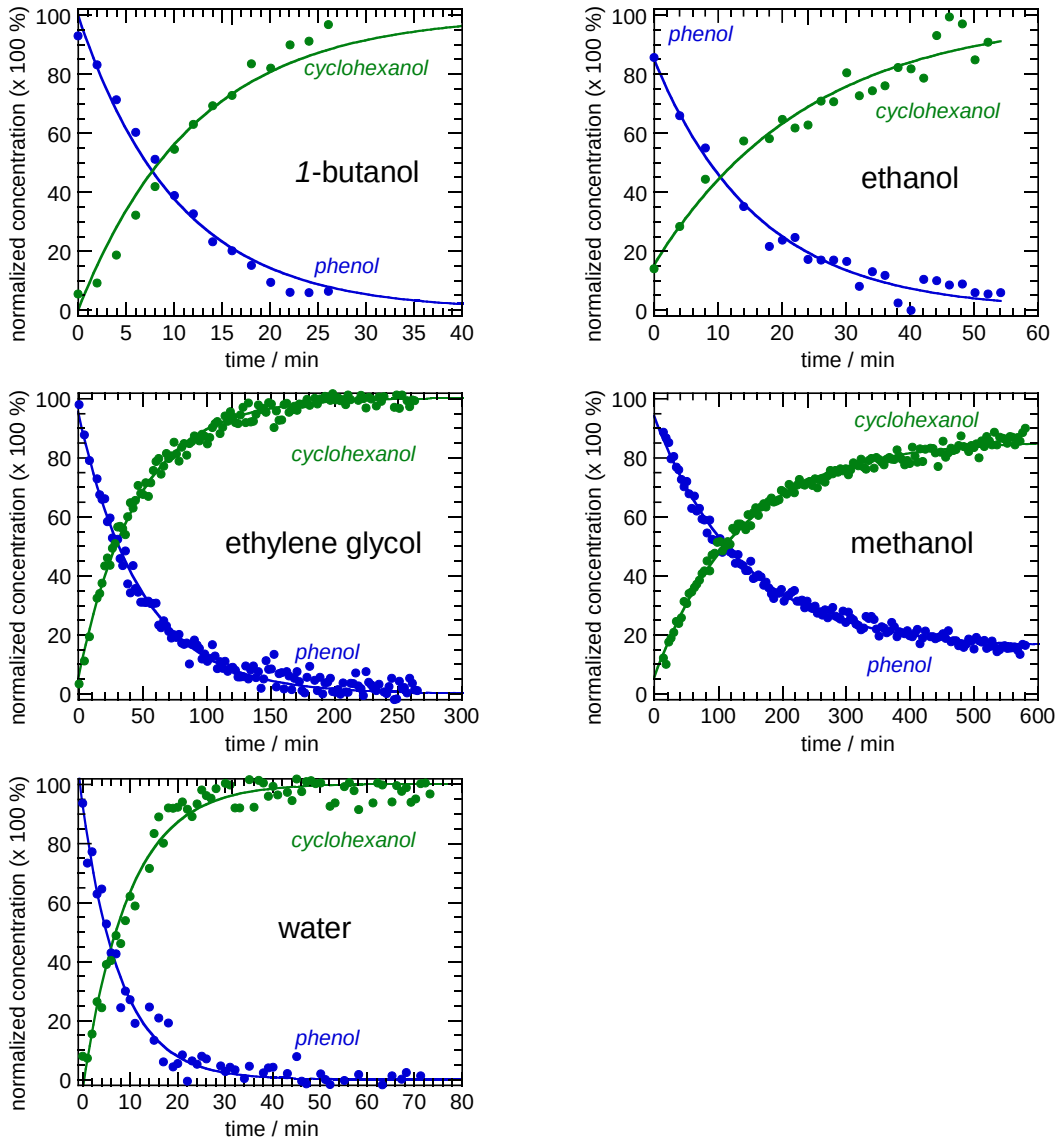

Figure S4.4. Kinetic analysis of individual ^{13}C NMR profiles recorded during PhOH hydrogenation in a rotor loaded with air-exposed Ni/γ-Al_2O_3 (2 wt%), 50 bar H_2, and 40 µL of solvent, after heating to 200 °C. Data collected during the induction period were removed prior to non-linear least-squares curvefitting. All solvents were analyzed with a single exponential rate equation.

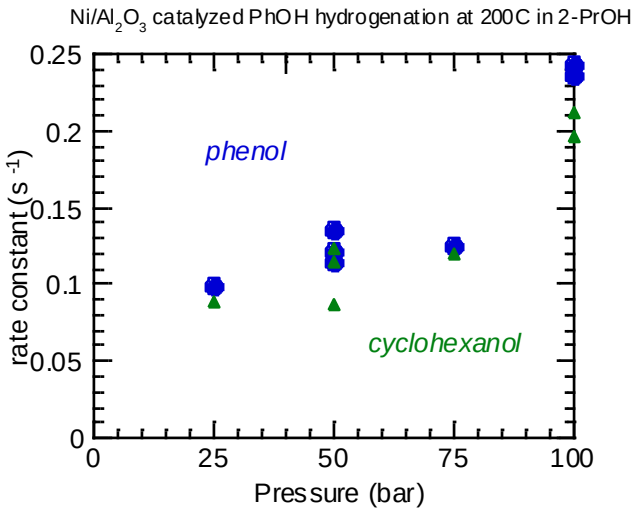

Figure S4.5. Rate constants for PhOH hydrogenation obtained by *operando* ^{13}C MAS NMR during hydrogenation of PhOH (0.63 mmol) catalyzed by Ni/γ-Al_2O_3 (30 mg, 2 wt% Ni) at 448 K with 25-100 bar of H_2 gas.

Table S4.1. Liquid solvent volumes and PhOH concentrations at 473 K

Solvent	Liquid fraction (%)		Volume [a]	C_s	$C_{PhOH,\ initial}$
	from NMR	from Antoine eq	(μL)	(M)	(M)
n-decane	-	97.5	140	4.3	0.45
p-xylene	-	96.5	136	6.9	0.46
benzene	89	91.2	133	9.2	0.47
toluene	-	94.6	135	7.9	0.47
anisole	-	97.9	136	7.9	0.46
pyridine	-	-	-	-	-
1-decanol	-	99.4	137	4.6	0.46
t-butanol	85	85.2	122	8.8	0.52
1-butanol	-	94.1	128	9.6	0.49
2-propanol	82	86.1	123	11.0	0.51
ethanol	86	88.4	126	14.4	0.50
methanol	88	89.4	135	19.6	0.47
ethylene glycol	-	99.6	131	16.3	0.48
water	-	98.8	123	53.6	0.51

[a] Calculated using the thermal expansion of the solvent at the reaction temperature.

Table S4.2. Rate and equilibrium constants for PhOH hydrogenation in methanol and ethylene glycol without fixing k´

Solvent	$k´$ ($M\ s^{-1}$)	K´ (M^{-1})	k_{obs} ($k´K´$) (s^{-1})
methanol	46(1,500)	0.011(0.35)	0.51(560.)
ethylene-glycol	66(950)	0.019(0.27)	1.3(260.)

Reaction conditions: PhOH (6.0 mg, 0.063 mmol), Ni/γ-Al_2O_3 (2 wt% Ni, 30.0 mg), 120 μL solvent, 50 bar H_2, 473 K.

Table S4.3. Rate and equilibrium constants for PhOH hydrogenation in methanol and ethylene glycol using pseudo-first order fit

Solvent	k_{obs} (s^{-1})
methanol	0.49(1)
ethylene-glycol	1.3(1)

Reaction conditions: PhOH (6.0 mg, 0.063 mmol), Ni/γ-Al_2O_3 (2 wt% Ni, 30.0 mg), 120 μL solvent, 50 bar H_2, 473 K.

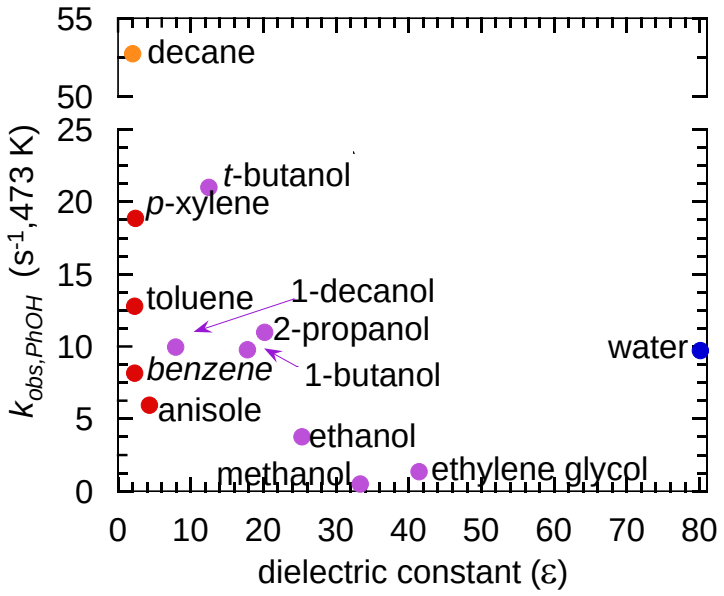

Figure S4.6. Variation of the apparent rate constant $k_{obs,PhOH}$ (product of k'_{PhOH} and K'_{PhOH}) for PhOH on the catalyst surface, with solvent dielectric constant. The various solvents studied are aromatics (red), alcohols (purple), *n*-decane (orange) and water (blue). Rate parameters were obtained from curvefits of kinetic profiles for PhOH hydrogenation at 473 K.

Table S4.4. Equilibrium adsorption of PhOH on Ni/γ-Al_2O_3 at 295 K

Solvent	pK_a	H-bond acceptor ability	H-bond donor ability	Adsorption (mmol g_{cat}^{-1})	% Phenol adsorbed
n-decane	-	0	0	0.65	22
p-xylene	-	0.12	0	0.39	13
benzene	-	0.11	0	0.30	10
toluene	-	0.10	0	0.32	11
anisole	-	0.32	0	0.27	9.0
pyridine	-	0.64	0	0.15	5.0
1-decanol	16.8	0.82	0.70	0.093	3.1
t-butanol	18.1	0.84	0.79	0.11	3.7
1-butanol	16.9	0.84	0.84	0.082	2.7
2-propanol	17.3	0.84	0.76	0.10	3.3
ethanol	16	0.75	0.86	0.058	1.9
methanol	15.5	0.66	0.98	0.011	0.37
ethylene glycol	15.1	0.52	0.91	0.022	0.73
water	15.7	0.47	1.17	0.099	3.3

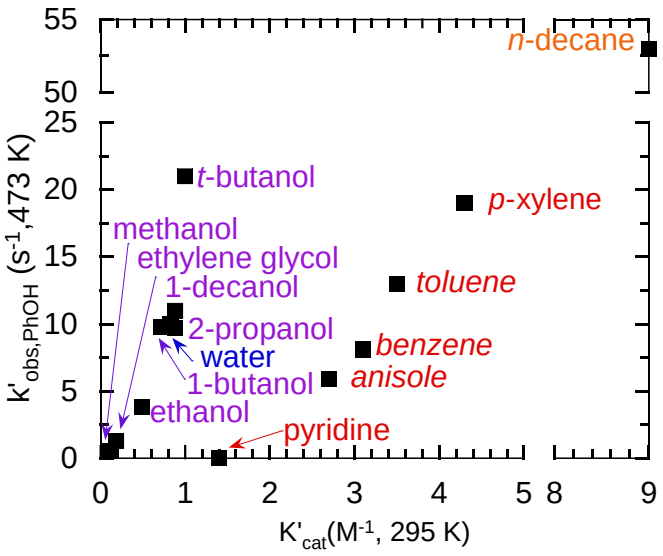

Figure S4.7. Relationship between the equilibrium constant $k'_{obs,PhOH}$ extracted from kinetic profiles for PhOH hydrogenation catalyzed by Ni/γ-Al_2O_3 at 473 K in various solvents (see Methods for reaction conditions) to PhOH adsorption constants K'_{cat} measured directly in the same solvents at 295 K.

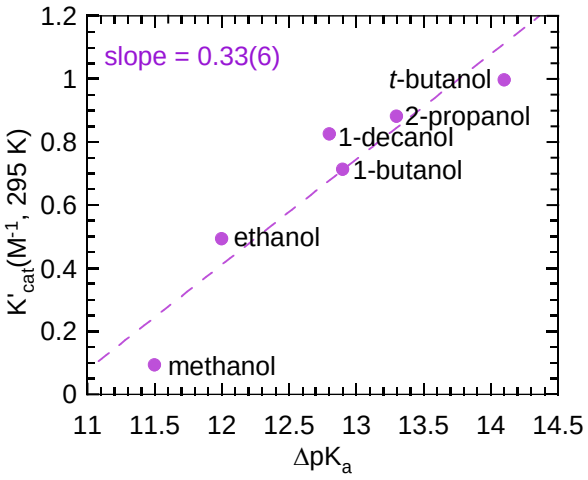

Figure S4.8. Correlation between solvent ΔpK_a and the corresponding PhOH adsorption constant K'_{cat} on Ni/γ-Al_2O_3, measured at 295 K. Ethylene glycol and water were not included in the trendline, due to the multiple H-bonds each solvent molecule can form.

Table S4.5. Amounts of PhOH adsorbed onto γ-Al_2O_3 and Ni/γ-Al_2O_3 from various solvents at 295 K

Adsorbent	Adsorbed amount (mmol g_{cat}^{-1})			K'_{cat} (M^{-1})		
	n-decane	toluene	2-propanol	n-decane	toluene	2-propanol
As-received γ-Al_2O_3	1.6	0.74	0.28	60	11	2.9
Pretreated γ-Al_2O_3[a]	0.85	0.55	0.05	14	6.7	0.44
$NiAl_2O_4$	0.81	0.55	0.06	13	7.2	0.55
Ni/γ-Al_2O_3	0.65	0.32	0.10	9.0	3.5	0.88

[a] Pretreated γ-Al_2O_3 was pretreated following the same procedure as the Ni/γ-Al_2O_3 catalyst. Calcination of the material in air at 1123 K for 5 hr, followed by reduction at 1123 K for 2 hr in flowing H_2.

Table S4.6. Kinetic parameters for BPE Hydrogenolysis with the addition of K'_{PhOH} in the denominator of the Langmuir model. Values in parentheses indicate the 95% confidence intervals.

Solvent	K'_{BPE} [M^{-1}]	K'_{BPE} [M^{-1}] (K'_{PhOH} fixed to 3.0 M^{-1})
2-propanol	12 (2)	13(2)
n-decane	22 (11)	23(13)

Reaction conditions: BPE (6.0 mg, 0.033 mmol), Ni/γ-Al_2O_3 (2 wt% Ni, 30.0 mg), 120 μL solvent, 50 bar H_2, 448K.

BPE rate equation with contributions of K'_{PhOH} in the denominator of the equation:

$$-\frac{dC_{BPE}}{dt} = \frac{n_{Ni}k_{BPE}\theta_{BPE}}{V} = \frac{n_{Ni}k_{BPE}K_{BPE}C_{BPE}}{V(C_{Solv}+K_{BPE}C_{BPE}+K_{PhOH}C_{PhOH})} = \frac{k'_{BPE}K'_{BPE}C_{BPE}}{1+K'_{BPE}C_{BPE}+K'_{PhOH}C_{PhOH}} \quad \text{(S4.1)}$$

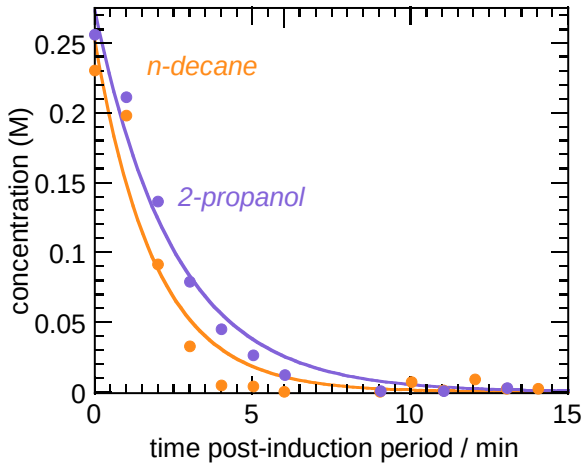

Figure S4.9. BPE kinetic profile fit a pseudo-first order model. Reaction conditions: BPE (6.0 mg, 0.033 mmol), Ni/γ-Al_2O_3 (2 wt% Ni, 30.0 mg), 120 μL solvent, 50 bar H_2, 448K.

Table S4.7. Adsorption measurements of BPE and PhOH to the catalyst and support at room temperature in both 2-propanol and *n*-decane.

Adsorbate	Adsorbent	2-propanol ($mmol/g_{cat}$)	n-decane ($mmol/g_{cat}$)
BPE	$Ni/\gamma\text{-}Al_2O_3$	0.027	0.076
BPE	$\gamma\text{-}Al_2O_3$	0.050	0.12
PhOH	$Ni/\gamma\text{-}Al_2O_3$	0.10	0.67
PhOH	$\gamma\text{-}Al_2O_3$	0.043	0.87
CyOH	$Ni/\gamma\text{-}Al_2O_3$	0.055	0.77
CyOH	$\gamma\text{-}Al_2O_3$	0.033	0.80